

# The Electrochemical Reduction of CO<sub>2</sub> on Bimetallic Electrocatalysts

---

A Thesis

Presented to  
the faculty of the School of Engineering and Applied Science  
University of Virginia

---

in partial fulfillment  
of the requirements for the degree

Master of Science

by

Zachary Hoffman

December

2016

APPROVAL SHEET

The thesis  
is submitted in partial fulfillment of the requirements  
for the degree of  
Master of Science

  
AUTHOR

The thesis has been read and approved by the examining committee:

Giovanni Zangari

---

Advisor

Robert Kelly

---

James Howe

---

---

---

Accepted for the School of Engineering and Applied Science:



Craig H. Benson, Dean, School of Engineering and Applied Science

December  
2016

# The Electrochemical Reduction of CO<sub>2</sub> on Bimetallic Electrocatalysts

Zachary Hoffman

M.S. Defense

August 5<sup>th</sup>, 2016

Advisor: Giovanni Zangari

Department of Materials Science and Engineering

University of Virginia

**Abstract:**

The electrochemical reduction of CO<sub>2</sub> provides an alternative and sustainable route to the production of valuable fuels and commodity chemicals. Electrocatalysts are of paramount importance to improve the efficiency and selectivity at which useful products are formed. Copper has been widely accepted as a material with very high catalytic activity towards this reaction, producing large amounts of hydrocarbons, formate, and syngas. However, only few studies have been performed where copper is alloyed with a second metal to produce bimetallic electrocatalyst materials for the reduction of CO<sub>2</sub>. In this thesis, we examine two such bimetallic systems for the electrocatalysis of CO<sub>2</sub> to value-added products: copper-indium and copper-bismuth.

Dendritic copper-indium alloys of various compositions were electrodeposited and investigated for their catalytic activity towards the reduction of CO<sub>2</sub>. These electrocatalysts produce formate at high efficiencies (up to 62%) while enabling tuning the ratio CO/H<sub>2</sub> to achieve the ideal syngas composition. The presence of intermetallics (namely Cu<sub>11</sub>In<sub>9</sub>) were confirmed, at/or near the catalyst surface, and the product distribution was found to be directly linked to the alloy composition. Furthermore, the observed product distribution, as a function of alloy composition and applied potential, can be rationalized in terms of the relative adsorption strengths of CO and COOH intermediates at Cu and In sites, and their variation with applied potential induced by the distinct electronic structure.

Copper-bismuth dendritic materials were also electrodeposited and explored for their ability to electrochemically reduce CO<sub>2</sub>. The films were dendritic and the microstructure consisted of a mechanical mixture of nanocrystalline grains of Cu, Bi, and metastable BiCu. These films selectively produce formate at efficiencies as high as ~90%, while producing a much

lower fraction of CO and H<sub>2</sub>. Product distribution trends, with respect to potential, show that lower reduction potentials typically yield the largest formate production. The selectivity to formate, on these catalyst surfaces, is explained in terms of the low adsorption strengths of CO<sub>2</sub> and COOH at Bi.

The alloying of sp-metals (In, Bi) to Cu, has been shown to modulate the selectivity and shift the reaction almost exclusively towards syngas and/or formate. The addition of an sp-metal dopant is shown to alter the relative trends of binding energies of COOH and CO observed for pure copper, giving way to the product distributions observed here. Overall, these studies highlight the opportunities of using bimetallic catalysts to enhance control over the product distribution and further suggest that bimetallic materials could be promising catalysts for the inexpensive, efficient and sustainable production of fuels and chemicals.

**Acknowledgements:**

I would first and foremost like to thank my advisor, Dr. Giovanni Zangari, for his continuous support and guidance throughout the past 2+ years. His breadth of knowledge and experience, in the fields of metallurgy and electrochemistry, have helped me in my research and educational endeavors, in pursuance of this degree. For that I am truly grateful to have been a part of his research group.

I would like to also thank Dr. Brent Gunnoe and Tristan Gray, my collaborators on my research. Without their patience, assistance, and enthusiasm, I would never have been able to accomplish the research I set out to perform. I am blessed to have had the opportunity to work with them and gain further insight into organic chemistry and analytical chemistry methodology.

The regular advice and assistance from Richard White, Dr. Michal Sabat, and Dr. Helge Heinrich at the NMCF (Nanoscale Materials Characterization Facility) was invaluable to my research efforts and growth as an aspiring materials scientist. The help and instruction from the faculty of the Center for Electrochemical Science and Engineering (CESE) as well as the overarching Materials Science and Engineering department are greatly appreciated.

The necessary financial support from the National Science Foundation (NSF, Grant #1152778), the UVA Office of Graduate Research, and the Jefferson Trust are gratefully acknowledged, herein. I would also like to thank my thesis defense committee of Dr. Robert Kelly and Dr. James Howe for their time, interest, and support throughout my graduate education.

Lastly (but certainly not least), I would like to thank my family and friends: my father, Douglas Hoffman; my sister, Abygail Owen; Jordan and Jeremy Bramow, my best friends

(essentially brothers); and Lok-Kun Tsui, Fu Zhao, and Marcel Mibus, my research group mentors. I am beyond thankful and blessed for all the wonderful people who have provided positivity, friendship, and kindness through all the highs and lows, good times and bad. Thank you for being a part of this pivotal turning point in my life.

# Table of Contents

Abstract.....	ii
Acknowledgements.....	iv
Table of Contents.....	vi
List of Figures and Tables.....	vii
Nomenclature.....	x
<i>Chapter 1: Introduction and Motivation.....</i>	<i>1</i>
<i>Chapter 2: Theory and Background - From Electrochemical Fundamentals to Electrodeposition and Electrocatalysis.....</i>	<i>5</i>
2.1 Electrode / Electrolyte Interface and Electrochemical Equilibria.....	5
2.2 Electrodeposition of Metals and Bimetallic Alloys.....	8
2.3 Electrocatalysis and the Electrochemical Reduction of CO <sub>2</sub> .....	18
2.4 Overview of Recent Literature and Motivation for Thesis Research.....	24
<i>Chapter 3: Experimental Methods and Instrumentation.....</i>	<i>30</i>
3.1 Electrochemical Setups, Instrumentation, and Software.....	30
3.2 Synthesis of Electrocatalyst Films.....	31
3.3 Custom Electrochemical Cell for the Electrochemical Reduction of CO <sub>2</sub> .....	34
3.4 Electrolysis – The Electrochemical Reduction of CO <sub>2</sub> .....	36
3.5 Product Identification and Quantification.....	37
3.6 Characterization Instrumentation and Techniques.....	46
<i>Chapter 4: The Electrochemical Reduction of CO<sub>2</sub>: The Copper-Indium System.....</i>	<i>54</i>
4.1 Structure and Morphology of Catalyst Materials.....	54
4.2 Electrolysis of CO <sub>2</sub> – Product Distribution and Conversion Rates.....	67
<i>Chapter 5: The Electrochemical Reduction of CO<sub>2</sub>: The Copper-Bismuth System.....</i>	<i>79</i>
5.1 Structure and Morphology of Catalyst Materials.....	79
5.2 Electrolysis of CO <sub>2</sub> – Product Distribution and Conversion Rates.....	88
<i>Chapter 6: Conclusions and Future Research Prospects.....</i>	<i>98</i>



## List of Figures:

**Figure 1.1:** Global anthropogenic CO<sub>2</sub> emissions from 1850 to present times.

**Figure 2.1:** A comparison of the Gout-Chapman and Helmholtz models for charge distribution at an electrode/electrolyte interface.

**Figure 2.2:** log j-V sample schematic showing the codeposition behavior of copper and indium.

**Figure 2.3:** Visual realization of the three fundamental modes of growth (Volmer-Weber, Stranski-Krastanov, Frank van der Merwe).

**Figure 2.4:** Schematic showing the electrodeposition and formation of nanofoam constructions.

**Figure 2.5:** Volcano plot showing the catalytic activity of metals and alloys for the hydrogen evolution reaction (HER).

**Figure 2.6:** Periodic table of elements highlighting the product distribution, by element, of the electrochemical reduction of CO<sub>2</sub>.

**Figure 2.7:** Electrocatalytic loop showing the conversion of CO<sub>2</sub> to CH<sub>4</sub> via proton coupled electron transfer (PCET).

**Figure 2.8:** A Pourbaix diagram showing the stable species in a CO<sub>2</sub>/H<sub>2</sub>O electrochemical system (pH vs. potential).

**Figure 2.9:** Plot showing number of publications on the “Electrochemical Reduction of CO<sub>2</sub>” since 2010.

**Figure 3.1:** Simple experimental set-up (beaker) for electrodeposition experiments.

**Figure 3.2:** Schematic of our custom electrochemical cell built in-house and used for CO<sub>2</sub> reduction experiments.

**Figure 3.3:** Photograph of the GC (gas chromatography) instrument used to analyze gaseous products.

**Figure 3.4:** Sample chromatograms of the various CO<sub>2</sub> reduction products and contaminants.

**Figure 3.5:** Photograph of the Varian 600 MHz NMR (nuclear magnetic resonance) instrument used in the Dept. of Chemistry at the University of Virginia.

**Figure 3.6:** Sample NMR spectrum showing several various potential products from CO<sub>2</sub> reduction.

**Figure 3.7:** Sample EDS spectra of Cu-In electrocatalysts used in ERC experiments.

**Figure 3.8:** FFT pattern comparison – one experimentally determined and another recreated using PDF-4 (ICDD) software – of an 83 at% In Cu-In alloy.

**Figure 3.9:** Ideal Randles circuit showing how EIS (electrochemical impedance spectroscopy) was performed and how the data was fit, to obtain double layer capacitances and surface areas.

**Figure 4.1:** SEM images of a copper dendrite and the surface of electroplated Indium.

**Figure 4.2:** Compositional dependence of Cu-In alloys on applied deposition potential using a specific Cu-In plated solution.

**Figure 4.3:** SEM images of dendritic Cu-In films used for the electrochemical reduction of CO<sub>2</sub>.

**Figure 4.4:** Cross-sectional SEM images of the dendritic Cu-In films used in CO<sub>2</sub> reduction.

**Figure 4.5:** SEM images of Cu-In alloys showing surface morphology before and after use in CO<sub>2</sub> reduction experiments.

**Figure 4.6:** XRD (X-ray diffraction) patterns for electrodeposited Cu-In films used for CO<sub>2</sub> reductions.

**Figure 4.7:** Two plots showing shifting of solid solution (111) peak as well as the calculated lattice parameter as a result of this shifting.

**Figure 4.8:** HR-TEM image of an 80 at% In, Cu-In electrocatalyst. Several views and FFT patterns are included.

**Figure 4.9:** HR-TEM image of an 60 at% In, Cu-In electrocatalyst. A FFT pattern is included.

**Figure 4.10:** HR-TEM image of an 25 at% In, Cu-In electrocatalyst. A FFT pattern is included.

**Figure 4.11:** EELS / EDS mapping of a 83 at% In, Cu-In films.

**Figure 4.12:** Grain size trends of various Cu-In alloys. Scherrer analysis was used.

**Figure 4.13:** Product distribution (Faradaic Efficiency) as a function of composition.

**Figure 4.14:** Product distribution (Faradaic Efficiency) as a function of potential.

**Figure 4.15:** Total and partial current densities as a function of composition and potential.

**Figure 4.16:** LSVs (linear sweep voltammetry) of various electrocatalysts, Cu-In and pure In.

**Figure 5.1:** SEM image comparing dendritic growth of copper and bismuth, via electrodeposition.

**Figure 5.2:** Plot showing composition of electrodeposited Cu-Bi films as a function of ion concentration of Bi<sup>3+</sup> and Cu<sup>2+</sup>.

**Figure 5.3:** SEM images showing dendritic morphology of Cu-Bi electrocatalysts from both a top-down and cross-sectional perspective.

**Figure 5.4:** SEM images before and after CO<sub>2</sub> reduction experiments for Cu-Bi films of various compositions.

**Figure 5.5:** Grazing Incidence XRD patterns covering electrocatalysts of all compositions from pure Cu to pure Bi.

**Figure 5.6:** HR-TEM of a 23 at% Bi, Cu-Bi dendrite with labeled grains and crystallographic planes.

**Figure 5.7:** Product distribution (Faradaic efficiency) of pure dendritic catalysts – Cu and Bi.

**Figure 5.8:** Product distribution (Faradaic efficiency) for the various Cu-Bi catalysts as a function of potential.

**Figure 5.9:** Product distribution (Faradaic efficiency) for Cu-Bi catalysts as a function of composition (at% Bi).

**Figure 5.10:** Geometric total and partial current densities for CO<sub>2</sub> reduction on Cu-Bi. Partial current densities include H<sub>2</sub>, formate, and CO.

## List of Tables:

**Table 3.1:** Retention times of various gaseous products or contaminants on a gas chromatogram.

**Table 3.2:** Tabulated Henry's law constants of relevant products in water.

**Table 3.3:** Relevant liquid product information – chemical structure, placement on NMR spectrum (chemical shift), and peak shape.

**Table 4.1:** Table exemplifying compositional durability of a couple Cu-In catalysts used in the electrochemical reduction of CO<sub>2</sub>.

**Table 4.2:** Calculated double-layer capacitances and roughness factors using EIS, for various electrocatalyst and reference materials.

**Table 5.1:** Table showing compositional durability of four Cu-Bi catalysts used in the electrochemical reduction of CO<sub>2</sub>.

## Nomenclature:

*	adsorbed species
$\alpha$	alpha parameter for EIS fitting
$A_{\text{catalyst}}$	Area of catalyst (high surface area) [cm <sup>2</sup> ]
$A_{\text{reference}}$	Area of reference material (smooth) [cm <sup>2</sup> ]
$\beta$	symmetry factor in the Tafel equation
$c_{aq}$	concentration of gas dissolved in solution [M]
$C_{dl}$	double layer capacitance [ $\mu\text{F}/\text{cm}^2$ ]
$C_{\text{catalyst}}^{DL}$	double-layer capacitance of catalyst (high surface area) [ $\mu\text{F}/\text{cm}^2$ ]
$c_{gas}$	concentration of gas in the headspace above the solution [M]
$C_{\text{reference}}^{DL}$	double-layer capacitance of reference material (low surface area) [ $\mu\text{F}/\text{cm}^2$ ]
CPE	constant phase element for imperfect capacitors
$d$	d-spacing between adjacent lattice planes [ $\text{\AA}$ ]
EASA	electrochemically active surface area [cm <sup>2</sup> ]
$E^\circ$	standard state half-cell potential [V]
$E_{app}$	applied potential [V]
$E_r$	Nernst potential [V]
$\eta$	overpotential [V]
$\eta_x$	overpotential, x = c, cathodic; x = a, anodic. [V]
F	Faraday's Constant (96485 coulombs/equivalent)
$\Delta G^\circ$	standard Gibbs free energy change [kJ/mol]
$\Delta G_H$	Gibbs binding energy of M-H, where M is an arbitrary metal [kJ/mol]
$G_{ox}$	Gibbs energy of the oxidation reaction in a redox couple [kJ/mol]
$G_{red}$	Gibbs energy of the reduction reaction in a redox couple [kJ/mol]
$i$	current density [mA/cm <sup>2</sup> ]
$i_0$	exchange current density [mA/cm <sup>2</sup> ]

$i_{red}$	reduction reaction partial currentensity [mA/cm <sup>2</sup> ]
$i_{ox}$	oxidation reaction partial current density [mA/cm <sup>2</sup> ]
$i_x$	current density, x = c, cathodic; x = a, anodic. [mA/cm <sup>2</sup> ]
$k_H$	Henry's law constant (M/atm)
$k_H^{cc}$	dimensionless Henry's law constant
m	mass [g]
$M^0$	deposited metal (neutral charge)
$M^{+}$	example metallic salt with valency, z
MSE	mercurous sulfate electrode
$M_w$	molecular weight [g/mol]
P	pressure [atm]
Q	total charge [C]
R	universal gas constant [8.314 J /mol-K]
$R_c$	compensated resistance [ohms]
$R_f$	surface roughness [cm <sup>2</sup> /cm <sup>2</sup> ]
$R_u$	uncompensated resistance [ohms]
$\delta$	chemical shift in NMR [ppm]
T	temperature (K or degrees C)
$V_{reference}$	resonance frequency of reference in NMR [MHz]
$V_{sample}$	resonance frequency of a sample in NMR [MHz]
z	number of electrons required to complete a given electrochemical reaction
$Z_w$	Warburg impedance

# Chapter 1: Introduction and Motivation

As the world's energy consumption continues to be centered on fossil fuels, especially in developing nations in Africa and Asia, relatively little has been done to offset the resulting growth of CO<sub>2</sub> emissions (**Figure 1.1**) into the atmosphere [1]. As a result, ongoing CO<sub>2</sub> discharge has with great probability caused unprecedented climate change and warming of the Earth [2, 3]. Sea-surges, due to polar ice melting, as well as extreme weather events could uproot tens to hundreds of millions of people, especially those in large coastal cities, causing unparalleled socio-economic devastation [4].

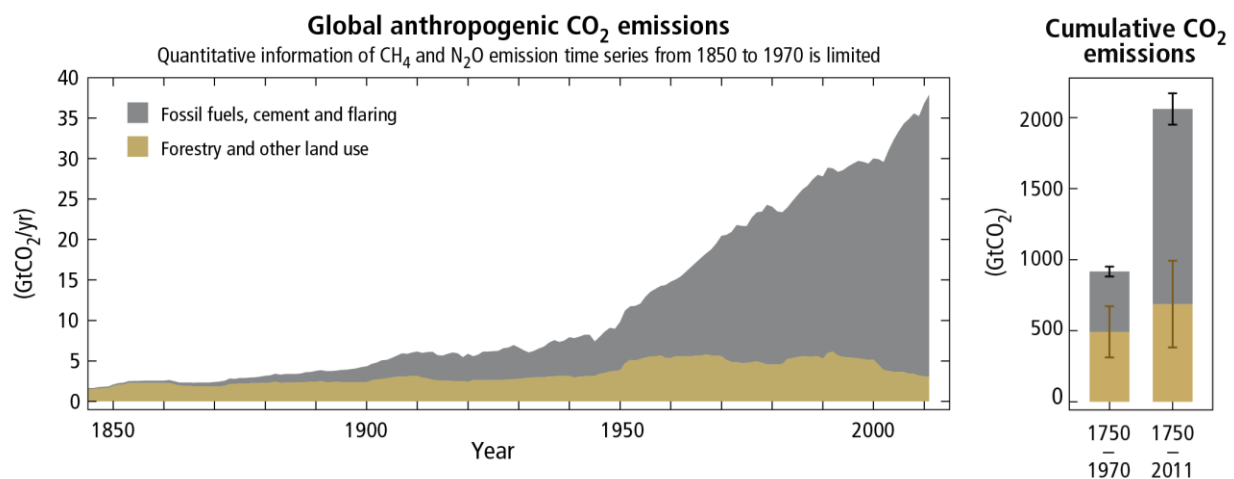


**Figure 1.1:** (left) Trends of atmospheric CO<sub>2</sub> emissions stemming from human activity, from 1850 to 2011. (right) Cumulative emissions of CO<sub>2</sub> in two different timeframes highlights the overwhelming amount of discharged CO<sub>2</sub> sent into the atmosphere, in recent years [1].

For the first time since CO<sub>2</sub> concentration has been measured, the top of the Mauna Loa will average above 400 ppm CO<sub>2</sub> all year, an iconic landmark in the monitoring of growing CO<sub>2</sub>

emissions. Even if society adopts an aggressive mitigation strategy, forecasts suggest that CO<sub>2</sub> concentrations, atop Mauna Loa, will not fall below this level during our lives [5]. Despite these recent alarming observations, the switch to renewables and clean energy may only be sparked by the ramifications of “peak oil.”

Theories by Hubbert, and other experts in energy policy and energy economics, anticipate a time where global oil output peaks (i.e. “peak oil”) will be followed by steady decreases and long-term economic consequences on developing and developed nations, alike. In the past, recessions have been sparked by, or occurred simultaneously with, increases in oil prices and/or decreases in oil production such as the Arab Oil embargo of the 1970s, the Iranian Revolution in 1980, and the recent economic depression (2007 to recent) [6]. It is extraordinarily difficult to pinpoint exactly when a global “peak oil” transition will occur, but it is believed to be happening during this century. Optimistic reports conclude this will occur after 2030; pessimistic reports anticipate this will happen before 2020; a few however believe that “peak oil” has already taken place [1]. Thus, the immediate need for adoption of cleaner renewable energy is evident for both economic reasons and aforementioned environmental implications -- CO<sub>2</sub> emissions are expected to increase until at least 2045, despite the good intentions of the recent Paris Agreement and several projected scenarios in which humanity actively seeks this transition [7].

Many technological solutions have been proposed in order to decrease the concentration of CO<sub>2</sub> in the atmosphere, including the mineralization of CO<sub>2</sub> (i.e. Iceland) and carbon capture and sequestration (CCS) [8-9, 10]. Advancements in CO<sub>2</sub> conversion technologies, alongside the rise of CCS facilities, has catapulted CO<sub>2</sub> recycling efforts into the spotlight of the global green energy community [11]. However, the most attractive process would be the transformation of CO<sub>2</sub> into useful chemicals, including fuels, by chemical or electrochemical methods – in

particular, the electrochemical reduction of CO<sub>2</sub> (ERC). The ERC has been shown to produce a variety of valuable products including hydrocarbons, syngas (CO + H<sub>2</sub>), formate, and small quantities of hydrocarbons and alcohols [12]. Recent economic feasibility analyses showed that the ERC under certain scenarios could be a profitable process, but could be made even more profitable with improvements in catalyst lifetime, reaction efficiency and selectivity, as well as reactor design and implementation [13].

The cost of fuel production (i.e. formate, methane, syngas) is significantly higher, compared to traditional fossil fuel processing, via the ERC due to the necessity for electricity, complex setup and materials, and relatively slow production rates. However, the ERC is a carbon neutral cycle when the products are utilized as fuel sources and the effluent CO<sub>2</sub> is recycled. The process allows us to use carbonaceous fuels without the further detriment of the environment. All in all, the ERC may not only provide an environmentally clean alternative source of fuel and chemical production (assuming the use of renewables such as electricity from wind or solar supplies the electrical current) but could also benefit the long-term energy infrastructure when oil output and availability begins to decline.

In this thesis, we focus on the electrocatalytic properties of two bimetallic systems, for the optimization of the CO<sub>2</sub> reduction reaction. Our work, herein, aims to explore bimetallic effects on catalytic properties in order to selectively produce value-added products at higher efficiencies than previous work. In particular, Ch. 2 discusses the relevant theory and background on fundamentals of electrochemistry, electrodeposition of metals and alloys, and the electrocatalysis of CO<sub>2</sub>. Ch. 3 displays the various instrumentation, methods, and experimental procedures required to perform or reproduce the work presented. Ch.4 and Ch. 5 discuss the synthesis and performance of two specific bimetallic systems for use in the ERC; the former



being copper-indium (Cu-In) and the latter copper-bismuth (Cu-Bi). These two systems, and their pure metallic counterparts, are explored with respect to electrochemical characteristics, metallurgical and surface characterization, and electrocatalytic properties in the ERC. Ch. 6 provides conclusions of the research performed and also provides recommendations for future research to further understanding of the CO<sub>2</sub> reduction reaction.

## References:

- [1] Pachauri, R. K., Allen, M. R., Barros, V. R., Broome, J., Cramer, W., Christ, R., ... & Dubash, N. K. (2014). *Climate change 2014: synthesis Report. Contribution of working groups I, II and III to the fifth assessment report of the intergovernmental panel on climate change* (p. 151). IPCC.
- [2] Hansen, J., Sato, M., Ruedy, R., Lo, K., Lea, D. W., & Medina-Elizade, M. (2006). Global temperature change. *Proceedings of the National Academy of Sciences*, 103(39), 14288-14293.
- [3] IPCC, 2007: *Climate Change 2007: The Physical Science Basis*, Cambridge University Press, Cambridge, UK and New York, NY USA.
- [4] Hanson, S., Nicholls, R., Ranger, N., Hallegatte, S., Corfee-Morlot, J., Herweijer, C., & Chateau, J. (2011). A global ranking of port cities with high exposure to climate extremes. *Climatic change*, 104(1), 89-111.
- [5] Betts, R. A., Jones, C. D., Knight, J. R., Keeling, R. F., & Kennedy, J. J. (2016). El Nino and a record CO<sub>2</sub> rise. *Nature Climate Change*.
- [6] Murphy, D. J., & Hall, C. A. (2011). Energy return on investment, peak oil, and the end of economic growth. *Annals of the New York Academy of Sciences*, 1219(1), 52-72.
- [7] Kharecha, P. A., & Hansen, J. E. (2008). Implications of “peak oil” for atmospheric CO<sub>2</sub> and climate. *Global Biogeochemical Cycles*, 22(3).
- [8] Herzog, H. J. (2001). Peer reviewed: what future for carbon capture and sequestration?. *Environmental science & technology*, 35(7), 148A-153A.
- [9] Global, C. C. S. "Institute." *The Global Status of CCS* (2014).
- [10] Oelkers, E. H., Gislason, S. R., & Matter, J. (2008). Mineral carbonation of CO<sub>2</sub>. *Elements*, 4(5), 333-337.
- [11] Centi, G., & Perathoner, S. (2009). Opportunities and prospects in the chemical recycling of carbon dioxide to fuels. *Catalysis Today*, 148(3), 191-205.
- [12] Ma, J., Sun, N., Zhang, X., Zhao, N., Xiao, F., Wei, W., & Sun, Y. (2009). A short review of catalysis for CO<sub>2</sub> conversion. *Catalysis Today*, 148(3), 221-231.
- [13] Agarwal, A. S., Zhai, Y., Hill, D., & Sridhar, N. (2011). The electrochemical reduction of carbon dioxide to formate/formic acid: engineering and economic feasibility. *ChemSusChem*, 4(9), 1301-1310.

# **Chapter 2: Theory and Background - From Electrochemical Fundamentals to Electrodeposition and Electrocatalysis**

This chapter outlines the theory and background, relevant to the research and work performed in this thesis. The chapter starts with a discussion of electrochemistry fundamentals and moves to selected concepts on the electrodeposition of alloys; finally, electrocatalysis phenomena are discussed as the main topic of this work. Some sections in this chapter are reproduced from manuscripts currently under preparation.

## **2.1) The Electrode / Electrolyte Interface and Electrochemical Equilibria**

Electrochemical processes, including electrodeposition and electrocatalysis, occur at the interface between an electrode and an electrolyte. In order for any electrochemical process to occur and be controlled the system should include a working electrode WE (in our case performing a reduction process, i.e. a cathode), a counter electrode CE (or anode) to complete the circuit, a reference electrode (RE) to precisely measure applied potentials, and an electrochemical cell to house these along with an electrolyte. Under equilibrium conditions, a charge separation at the electrode/electrolyte interface is present. Generally, electrons accumulate at the electrode surface (the WE) while a distribution of overall oppositely charged ions gather on the electrolyte side. Once the equilibrium between the ions present in the

electrolytes and the electrode is reached, the potential difference across this interface, referenced to a given RE (typically the standard hydrogen electrode, SHE [1]), is known as the half-cell potential for that particular ion/electrode system.

The Helmholtz model was the first physical model describing this interface, also called the *electrical double layer*. The model assumes behavior analogous to a capacitor, where two separated layers of opposite charge (+ and -) are separated by a finite distance,  $d$ , with nanometer scale. It is then assumed that the voltage drop across this surface is linearly related to  $d$ . This early model has worked relatively well experimentally, but has been unable to explain observed trends and has vastly been improved since its development in 1874 [2].

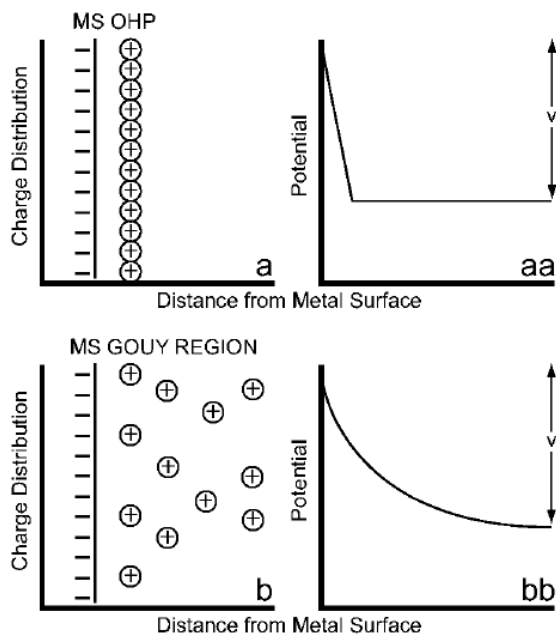


**Figure 2.1:** Schematics comparing the Helmholtz model (top) and Gouy-Chapman model (bottom) with respect to charge distribution and potential profile at the electrode / electrolyte interface. [4]

The Gouy-Chapman model predicts that the charge in the electrolyte is not at a set distance from the electrode surface, but that ions are distributed in the surrounding electrolyte. This distribution is dictated by the Maxwell-Boltzmann statistics, that take into account thermal agitation and electrostatic forces in the potential distribution [3]. These two models are illustrated in **Figure 2.1**. A later model of the double layer, that takes into account a combination of the two models, is capable to predict most of the observed features.

As mentioned above, the half-cell potential is defined as the potential drop across the electrode/ electrolyte interface, in reference to the RE. The half-cell potential for a generic redox couple at standard state,  $E^0$ , is the basis for determining the thermodynamics of electrochemical systems. The standard Gibbs free energy change ( $\Delta G^0$ ) of an electrochemical reaction (**Eqn. 2.1**) is defined as the difference between two redox couples, as shown below:

$$\Delta G^{\circ} = G_{red} - G_{ox} \quad (\text{Eqn. 2.1})$$

$$\Delta G^{\circ} = -zFE^{\circ} \quad (\text{Eqn. 2.2})$$

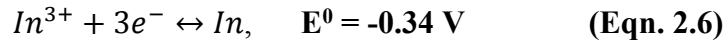
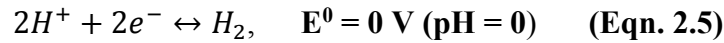
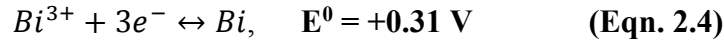
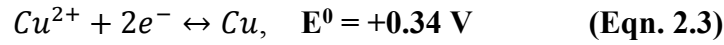
where  $F$  is the Faraday's constant (96485 C/mol) and  $z$  is the number of electrons transferred per ion (oftentimes the valency of the ion). If  $\Delta G^{\circ} < 0$ , the given reaction is spontaneous; if  $\Delta G^{\circ} = 0$ , the reaction is in equilibrium; if  $\Delta G^{\circ} > 0$ , the reaction is non-spontaneous and requires the supply of electrical energy to the system in order to occur.  $E^0$  is the potential at which a given reaction (i.e., metal dissolution/deposition) occurs in equilibrium and reversibly, at standard state conditions of  $T = 25$  degrees C,  $P = 1$  atm, with an activity of  $\sim 1$ .

## 2.2) The Electrodeposition of Metals and Bimetallic Alloys

### a.) Introduction to the Electrodeposition of Metals

Electrodeposition is the process of plating metallic films onto an electrode substrate, from an aqueous solution. The electroplating solution, contains metallic salts, sometimes together with complexing agents to maintain the metal ions in solution, and other additives that contribute to the formation of dense, continuous metallic films.

Equations (2.3) through (2.6) list a set of redox couples, and their standard potentials, from most to least noble, relevant to this work [5].



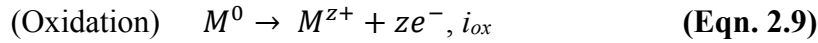
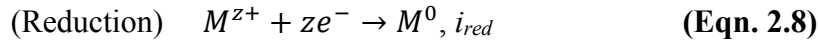
The hydrogen evolution reaction (HER), portrayed in **Eqn. 2.5**, is added to the other metal reduction reactions as it is an important side reaction, sometimes competing with metal electrodeposition.

In most cases standard conditions do not apply, and  $E^0$  differs from the equilibrium potential  $E_r$ , called also the *Nernst Potential*. The Nernst equation determines the equilibrium between metal ion and deposited metal. Given an arbitrary metal, M:

$$E_r = E^0 + \frac{RT}{zF} \ln \frac{[M^{z+}]}{[M^0]} \quad (\text{Eqn. 2.7})$$

where  $R$  is the universal gas constant,  $T$  is the deposition temperature,  $M^{z+}$  is the metallic salt or ion with valency  $z$ , and  $M^0$  is the deposited metal on the substrate (where  $[M^0]$  is unity for a pure metal). The Nernst potential,  $E_r$  depends therefore among others on the concentration of metal ions in solution.

Electrochemical equilibrium is purely dynamic in the sense that the opposite reduction and oxidation reactions, relevant to the system, are occurring at exactly the same rate or current density [1]. The sum of the two current densities is zero, so no net current flows through the system – hence the term “dynamic equilibrium”. The partial current density of either partial process, the reduction or oxidation reaction, is known as the exchange current density,  $i_0$ .



$$i_{red} + i_{ox} = 0 \quad \textbf{(Eqn. 2.11)}$$

$$|i_{redox}| = |i_{ox}| = i_0 \quad \textbf{(Eqn. 2.12)}$$

The exchange current density affects the kinetics of a given reaction. Specifically, a higher exchange current represents a higher propensity for charge to flow across the electrode / electrolyte interface [6].

The overpotential, typically denoted as  $\eta$ , is the difference between the applied potential,  $E_{app}$  and the Nernst potential of the redox couple,  $E_r$ , as defined by:

$$\eta = E_{app} - E_r \quad \textbf{(Eqn. 2.13)}$$

The overpotential represents the driving force necessary to overcome the energy barrier for running the electrochemical process of interest. This quantity can be broken down into various

components due to the various phenomena occurring during films growth; they include activation of the charge transfer, nucleation as the initial process for film formation, and concentration gradients, related to diffusion of ionic species. If  $\eta > 0$ , the oxidation reaction is favored, as shown above in **Eqn. 2.13**. If  $\eta < 0$ , the reduction reaction is favored, and in the case of electrodeposition the metal will be deposited from an electrolytic solution. Note that the potential is a thermodynamic term in electrochemistry; in contrast, the overpotential is directly linked to the kinetics of an electrochemical process or reaction.

When an overpotential is applied, the electrochemical system is no longer at equilibrium, and a net current flows. The applied current density in these conditions is a combination of anodic and cathodic currents, of which both are a function of the exchange current density ( $i_0$ ), overpotential ( $\eta$ ), temperature ( $T$ ), numbers of electrons exchanged ( $z$ ), and the symmetry factor ( $\beta$ ) (**Eqn. 2.14**).

$$i_{app} = i_a - i_c = i_0 e^{\frac{\beta z F \eta}{RT}} - i_0 e^{-\frac{(1-\beta) z F \eta}{RT}} \quad (\text{Eqn. 2.14})$$

This equation is known as the Butler-Volmer expression and relates electrochemical kinetics (in units of current density) to applied potential. The symmetry factor is a dimensionless parameter that quantifies the symmetry of the energy barrier for charge transfer in the anodic or cathodic directions, for a single-step reaction. The expression for  $i_c$  from the Butler-Volmer equation can be manipulated to yield the Tafel expression, as shown in **Eqn. 2.15**:

$$\eta_c = \frac{-2.3RT}{(1-\beta)zF} \log\left(\frac{i_c}{i_0}\right) \quad (\text{Eqn. 2.15})$$

The Tafel slope is equal to  $-2.3RT/(1-\beta)zF$  and is often used to compare an experimentally measured kinetics with a theoretical mechanism for the same reaction. Note that the Tafel

relationship can be used only at potentials sufficiently far from the equilibrium potential (typically 120 mV), and for a single electron exchange. In some cases however, reactions involving multiple electron exchanges exhibit a kinetics similar to that of the Tafel equation, only with the  $z$  being equal to the number of electrons being exchanged [1].

Another important relationship, known as Faraday's law of Electrolysis, allows to calculate the amount of a formed product (products from electrocatalysis or an electrodeposited material) using the charge passed through the electrochemical cell ( $Q$ ), number of electrons involved in the reaction ( $z$ ), Faraday's constant, and the molecular weight ( $M_w$ ) of the relevant product. The law is given by **Eqn 2.16**:

$$m = \frac{QM_w}{Fz} \quad (\text{Eqn. 2.16})$$

The mass can be interchanged with  $\rho V$ , or the density multiplied by the volume. The expression can be shifted around to calculate the necessary charge,  $Q_n$ , given a target mass,  $m_n$ , of a product. The Faradaic efficiency (FE) of a product (1), is calculated from the following expressions:

$$Q_1 = \frac{m_1 Fz}{M_{w,1}} \quad (\text{Eqn. 2.17})$$

$$\frac{Q_1}{Q_{total}} * 100\% = FE \text{ of Product 1 (\%)} \quad (\text{Eqn. 2.18})$$

The sum of all product charges ( $Q_n$ ) should equal the total charge ( $Q_{total}$ ) and includes both useful species and unwanted side products, such as HER during electrodeposition. The Faradaic efficiency allows to calculate the selectivity of products effluent from an electrochemical reaction, such as the electrochemical reduction of  $\text{CO}_2$ .



## b.) Electrodeposition of Bimetallic Materials

The electrodeposition of alloys consists in the electrochemical growth of films that contain more than one metallic element. As with the electrodeposition of single metals, multiple metallic salts in solution are reduced to metal atoms on the substrate (WE surface) and are co-deposited. The relative nobility and the electrochemical kinetics of the metals being deposited is of utmost importance in understanding overall deposition behavior as well as the final film composition and crystallography. Let us assume that the metal ions deposit independently (that is, each one with its own kinetics). In this case the more noble metal A, having the higher standard potential, will typically be deposited with priority over the less noble metal B, and the alloy will be richer in A. However, the metal ion concentration may limit the maximum reduction rate due to diffusional limitations; in this case the composition will depend both on the relative kinetics and the relative concentration of A and B in solution. In some cases, the two metal ions in solution interact strongly through the formation of intermediates and adsorption processes, leading to anomalous or induced codeposition processes as described by Brenner [7]. Applying a given potential to a cathode immersed in a bimetallic electroplating solution results in the two metals being subject to two different overpotentials based on the distinct Nernst potentials of each metallic salt in solution.

$$\eta_1 = E_{app} - E_{r,1} \quad \text{(Eqn. 2.19)}$$

$$\eta_2 = E_{app} - E_{r,2} \quad \text{(Eqn. 2.20)}$$

As mentioned, the more noble metal has the higher standard potential and in turn a higher overpotential for deposition. The difference in overpotential between the two depositing metals

can determine the composition of the bimetallic material and the resulting phase constitution and microstructure.

Co-electrodeposition leads to the formation of alloys with identifiable phases and crystallographic structure; in many cases equilibrium phases may be obtained; however, in some cases metastable phases may be grown. Additionally, the alloys being formed may not be simple solid solutions but they may form mechanical mixtures of the two elements. A high mutual solubility of the two elements usually results in the formation of solid solution phases; on the other hand intermetallic phases, and sometimes even metastable phases usually found at very high temperatures and pressures can be obtained [8, 9].

The two relevant systems, discussed herein, show different deposition behavior. **Figure 2.2** shows a schematic current density vs. applied voltage (i-V) plot specific for the Cu-In system, where pure Cu deposition occurs at potentials between  $E_{Cu^{2+}}$  and  $E_{In^{3+}}$ , followed by Cu-In codeposition below  $E_{In^{3+}}$ . The Cu-In system exhibits a wide gap between the  $Cu^{2+}$  and  $In^{3+}$  (Eqns. 2.3 and 2.6) standard potentials, and limited changes can be achieved by varying the metal ion concentrations; therefore, once the redox potential of In is reached, Cu is being deposited already with 0.68 V of overpotential, at a high deposition rate and in most cases under diffusional limitations. In order to tune the alloy composition, the electrolyte must be very indium rich in order to deposit films across the whole composition range by varying the applied potential.

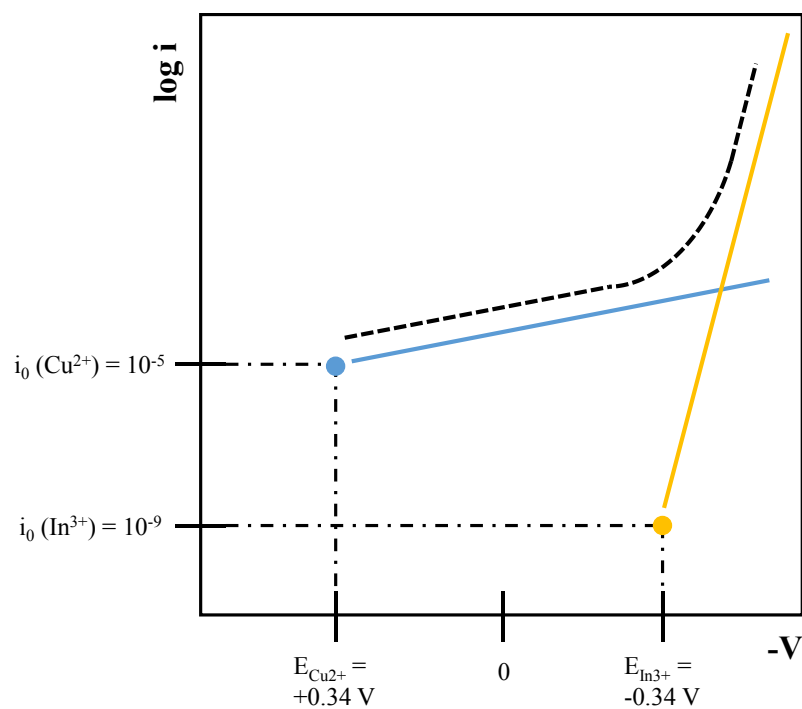


**Figure 2.2:** An example  $\log(i)$ - $V$  curve summarizing codeposition of Cu-In films. The occurrence of hydrogen evolution is neglected in this plot.

The Cu-Bi system in contrast exhibits a very small gap between the  $\text{Cu}^{2+}$  and  $\text{Bi}^{3+}$  (Eqns. 2.3 & 2.4) standard potentials, leading to the composition of the plated film being almost identical to the concentration of these metal ions in the electrolyte. In practice, a propensity to form films with a slightly higher Cu fraction than its relative concentration in solution was observed. This arises due to differences in Tafel slopes between depositing Cu and Bi: Cu deposition on Cu, from an acidic sulfate solution, has a slope of 120 mV/dec; Bi on Pt, from an acidic perchlorate solution, has a slope of  $\sim 80$  mV/dec [10-11]. Identical Tafel slopes for both species with similar redox potentials would yield films of identical composition of the solution,

while largely varying Tafel slopes can drastically affect deposited film composition, regardless of redox potential proximity.

### **c.) Tuning Surface Morphology**

The metallic film formed on the substrate surface may exhibit varying surface morphologies, dependent on the plating solution chemistry, the deposition potential, the substrate, and the deposition conditions (including temperature, cell geometry, and size/shape of the CE). The growth of an electroplated film depends on the conditions of nucleation, dependent in turn on the applied overpotential, the presence of additives to hinder growth of large grains, and the surface mobility of adsorbed atoms (adatom) on the growing surface. By rationally selecting the growth conditions, the film may form a variety of morphologies, including compact and smooth films, rough films, or dendritic constructions.

Two stages of electrodeposition may, in particular, determine surface morphology: kinetic control and diffusion control of growth. Cu and In, as mentioned earlier, show a large gap between their standard Nernst potentials, with Cu being the more noble metal. As shown above in **Figure 2.2**, Cu-In can only be codeposited at potentials more negative than the Nernst potential of In. At the onset of In deposition, a large overpotential is already achieved for Cu deposition, resulting in diffusion controlled growth and morphological growth instability [12]. At this point, In is being deposited via kinetic control and follows Tafel behavior. Typically, diffusion controlled growth results in roughening and formation of dendritic films such as in our case with Cu-In and Cu-Bi (see Chapters 4 and 5).

Smoother films require higher adatom surface mobility, and can typically be produced when substrate irregularities and the Schwöbel barrier (the energy barrier for an adatom to jump down from an island) are minimized [12]. Thus, at low overpotentials, growth can be more two-dimensional and produce films that are more compact, depositing atoms layer by layer. This is the Frank van-der Merwe mechanism of growth (**Figure 2.3**). On the other hand, kinetic controlled growth typically results in smoother films as opposed to growth instability and rough surfaces when deposition occurs in the diffusion limited regime. The addition of surfactants may contribute to attain 2-D compact growth, by adsorbing to surface sites, thus slowing down deposition and increasing nucleation density [13, 14].

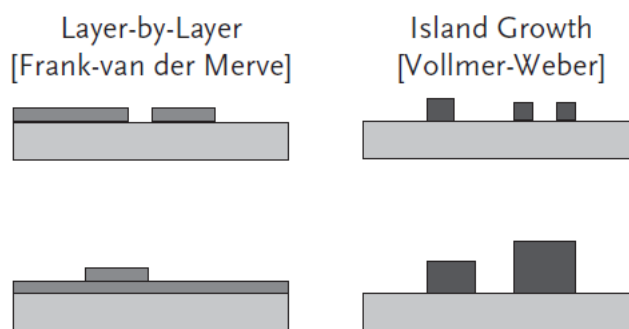


**Figure 2.3:** Two fundamental growth modes that apply to electrodeposition. Frank-van der Merwe shows more 2-D compact growth while Volmer-Weber reveals 3-D outward growth, resulting in rougher films. [15]

Rougher and dendritic films can be produced by a variety of conditions or combinations of conditions. Three-dimensional growth, as seen with rough or dendritic morphologies, can occur via Volmer-Weber growth (**Figure 2.3**), at small overpotentials. However, dendritic films

can easily be produced at large overpotentials, where the probability for nucleation increases – especially on already deposited nuclei, leading to outward 3-D growth [12]. Dendritic growth is linked to the crystal structure and symmetry of the material being deposited. If a material naturally exhibits anisotropy, (i.e. hexagonal Zn, **Figure 2.4**), it is possible for it to grow dendritically. Dendritic growth typically occurs along the lowest energy plane for growth, which is (0001) in the case of Zn [16]. Also, the competing hydrogen evolution process, with the simultaneous hydrogen reduction on the substrate, may assist in achieving rough or dendritic films [17].

High surface area materials (i.e. dendrites, nanoporous films, nanofoams) may be mechanically fragile, but are ideal for electrocatalysis applications due to a large surface area and larger number of catalytic sites capable of performing the relevant electrochemical reaction.

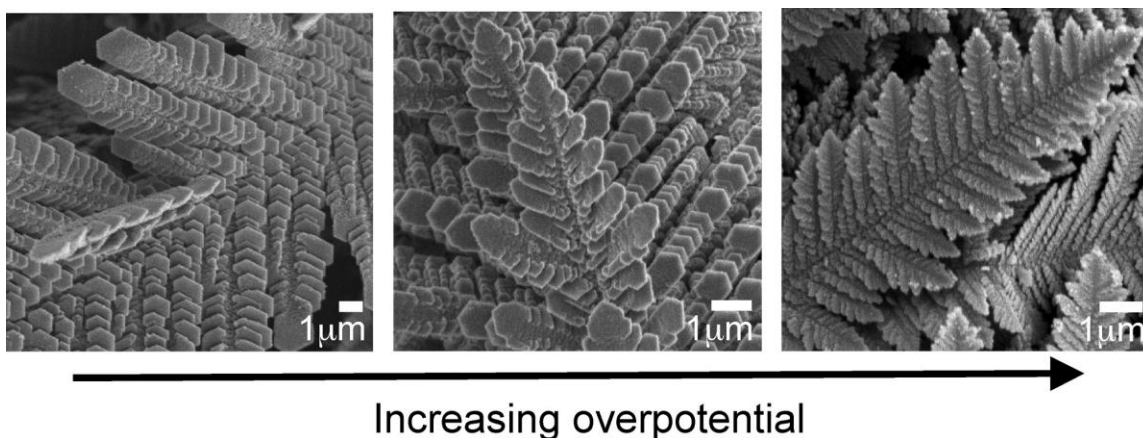


**Figure 2.4:** The changes in surface morphology of electrodeposited hexagonal-Zn films. As overpotential increases, side branch growth and faceting are shown to increase. [16]

## 2.3) Electrocatalysis and the Electrochemical Reduction of CO<sub>2</sub>

### a.) Electrocatalysis on Bimetallic Surfaces

Electrocatalysis is utilized to facilitate a target electrochemical reaction; when more reactions are possible a catalyst may also shift the selectivity of an electrochemical reaction. In general, the catalyst is not consumed in the process. Similar to traditional catalysis, different types of electrocatalysts exist: surface (heterogeneous) and photoelectrocatalysts [18-20]. We will focus our attention on the first, more specifically electrocatalysis at metallic and bimetallic surfaces.

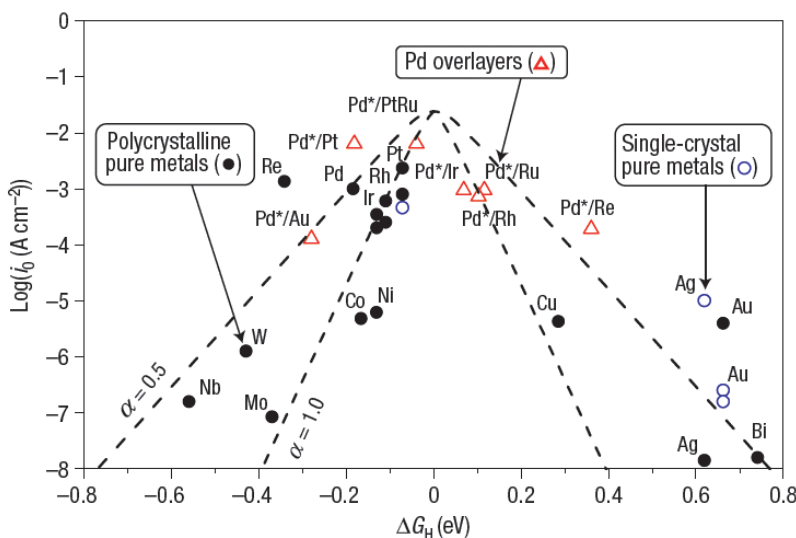


**Figure 2.5:** A volcano plot showing the exchange current densities for HER on various metallic and bimetallic surfaces. DFT derived data suggests an optimal electrocatalyst for HER will have a  $\Delta G_H = 0$ . [21]

Different metals and alloy systems show differences in their inherent catalytic properties due to their specific electronic structure. This results for example in differences in binding energy of

reactants and intermediates, which eventually result in varying kinetics, products being formed, and selectivity [21]. A prototypical example of these effects is the activity towards HER on various metals and alloys as portrayed by a volcano plot in **Figure 2.5**. The exchange current density for HER (y axis) varies significantly with the catalyst material, due to the variation of binding energy of H at the selected surface (x axis). A higher exchange current density for HER reveals a greater propensity for this reaction to occur when an overpotential is applied. This type of analysis connects electrochemical kinetics of a given reaction (i.e. HER) to the adsorption properties of relevant chemical intermediates (i.e.  $H^+$ , H). Note that many of these HER electrocatalysts are alloys, suggesting that a bifunctional catalytic mechanism for HER may be operative.

The concept of a bifunctional reaction mechanism calls on the cooperation of the two metals, each with its own adsorption or, more generally, catalytic properties that work synergistically to perform or shift an electrochemical reaction. The oxidation of methanol is one example in which Pt-Ru alloys are widely utilized. Pt is efficient to split methanol and adsorb CO strongly to the surface, while Ru in parallel splits water and adsorbs OH, then adjacent Pt and Ru surface atoms work together to produce  $CO_2$  [1, 22]. Bifunctional mechanisms work in multi-step reactions, where adsorption of different chemical species (i.e. C or O) at the catalyst may be required to see the reaction to completion. Neither individual metal could perform the reaction, but together they provide the means to successfully and efficiently do so. This bifunctional (or multifunctional) mechanism could be applied to many other important reactions such as those occurring in fuel cells and the electrocatalysis of  $CO_2$ .



## b.) The Electrochemical Reduction of CO<sub>2</sub>

The electrochemical reduction of CO<sub>2</sub> (ERC) has been studied thoroughly using various classes of catalysts [23]; metallic electrodes, in particular, require minimal manufacturing efforts and provide favorable electron transfer kinetics. Early on, Hori developed a classification (Figure 2.6) of the products formed by different catalyst materials; roughly, Au and Ag reduce CO<sub>2</sub> only to CO, sp post-transition metals such as In, Pb, Sn, produce mostly formate, and late transition metals such as Pt, Ni, Fe form mainly H<sub>2</sub>. Copper is unique among the metals as it has been shown to convert CO<sub>2</sub> to a wide range of products, including CO, formate, hydrocarbons and alcohols.

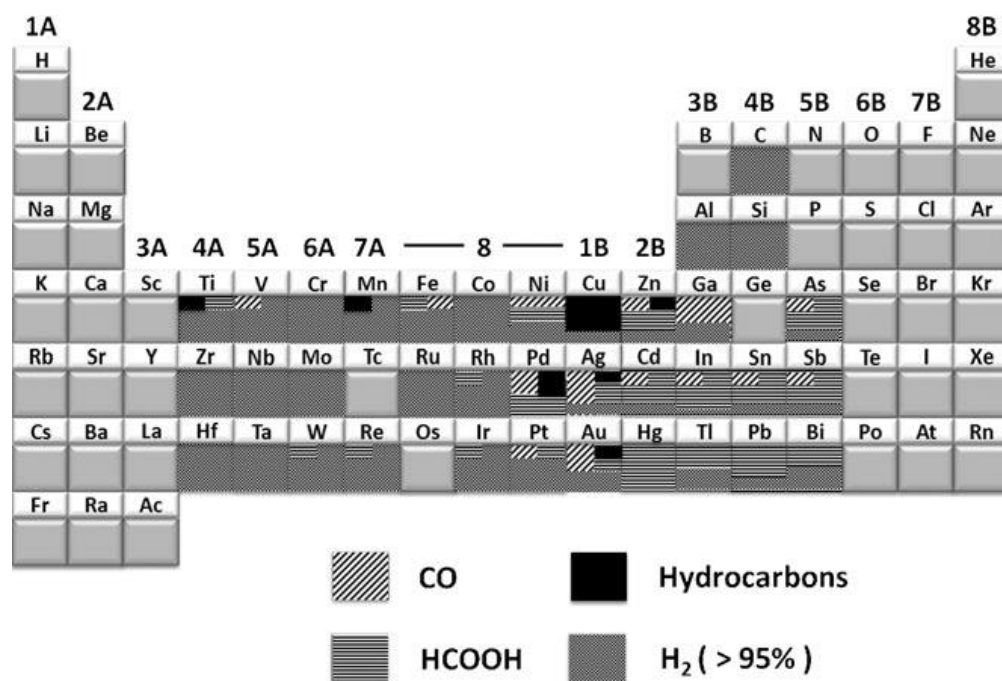


**Figure 2.6:** An insight into the electrocatalytic properties of elements towards the reduction of CO<sub>2</sub>. [24]

Unfortunately, these transformations occur at copper electrodes only at high overvoltage, where the hydrogen evolution reaction (HER) is in competition with CO<sub>2</sub> reduction, leading to a decline of the overall efficiency and selectivity [25, 26]. The ERC has been found to form CO or formate selectively with efficiency approaching 100%, although the formation of these species requires precious metallic catalysts [27, 28] or other impractical conditions and materials such as high pressures or temperatures and an ionic liquid environment [29, 30].

The product distribution of the ERC as a function of applied potential has been initially rationalized by Norskov's group utilizing the Computational Hydrogen Electrode (CHE) approach, whereby a given reaction step may occur when the applied potential decreases the thermodynamic barrier for that step to zero. The model is purely thermodynamic, and assumes that the energy barrier for such step is negligible. According to this theory the products obtained with increasing applied overvoltage are H<sub>2</sub>, HCOO<sup>-</sup>, CO and CH<sub>4</sub> [31]. However, this model fails to take into account the influence of a bulk water environment. Norskov's assumes a monolayer of water surrounds the catalyst surface – a strong generalization of a bulk aqueous environment. He concedes that improvements to the model can be made with respect to water [32]. Furthermore, the model never mentions the influence of the electrochemical cell (geometry, orientation, overall setup), which has a significant effect on the ERC process, as a whole. A catalytic loop demonstrating the reaction mechanism(s) to form the latter three products are shown in **Figure 2.7**. They occur via a series of successive PCET (proton coupled electron transfer) reactions with relatively positive redox potentials [31]. Proposed and modeled by Norskov, this mechanism proceeds through successive hydrogenation of CO to CHO, CH<sub>2</sub>O, and so forth, but doesn't describe formation of ethylene.

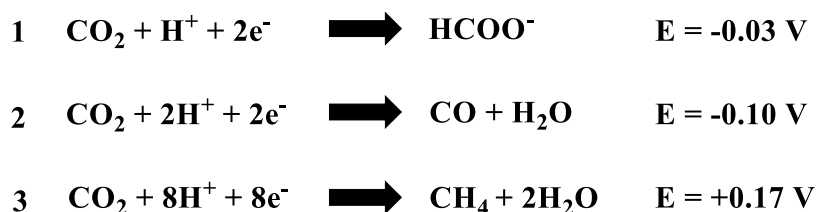
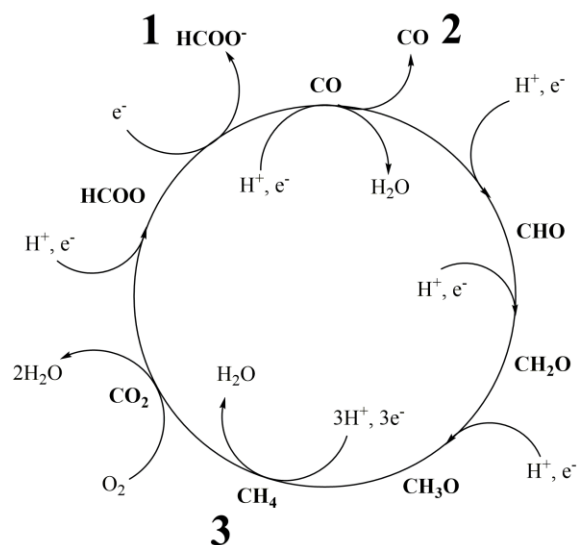


**Figure 2.7:** An electrocatalytic loop visualizing the ERC by consecutive PCET steps to form (1)  $\text{HCOO}^-$ , (2)  $\text{CO}$ , and (3)  $\text{CH}_4$ .  $\text{CH}_4$  is then oxidized back to  $\text{CO}_2$  generating electricity, and the cycle repeats. Adapted from Kortlever et al. [33]

The ERC affords a couple reaction pathways that determine the end products and distribution. The formate pathway, as its name suggests, ends at formate, which cannot be further reduced or hydrogenated. Different from the pathway proposed by Norskov above, Hori [34] proposed a carbene ( $^*\text{CH}_2$ ) intermediate which could also lead to methane but also ethylene via dimerization or reaction with another adsorbed  $^*\text{CO}$  intermediate [33]. However, the formation of ethylene has been shown to occur without the co-evolution of methane, which cannot be explained by either mechanism. Thus, it is still unknown how these various products are formed,

but it is universally accepted that high value hydrocarbons are formed through a CO intermediate.

The pH is also an important measurement to understand the ERC in a specific system.

**Figure 2.8**, shows the CO<sub>2</sub> Pourbaix diagram which correlates stable phases of CO<sub>2</sub> (pH) versus applied potential (V vs SHE).

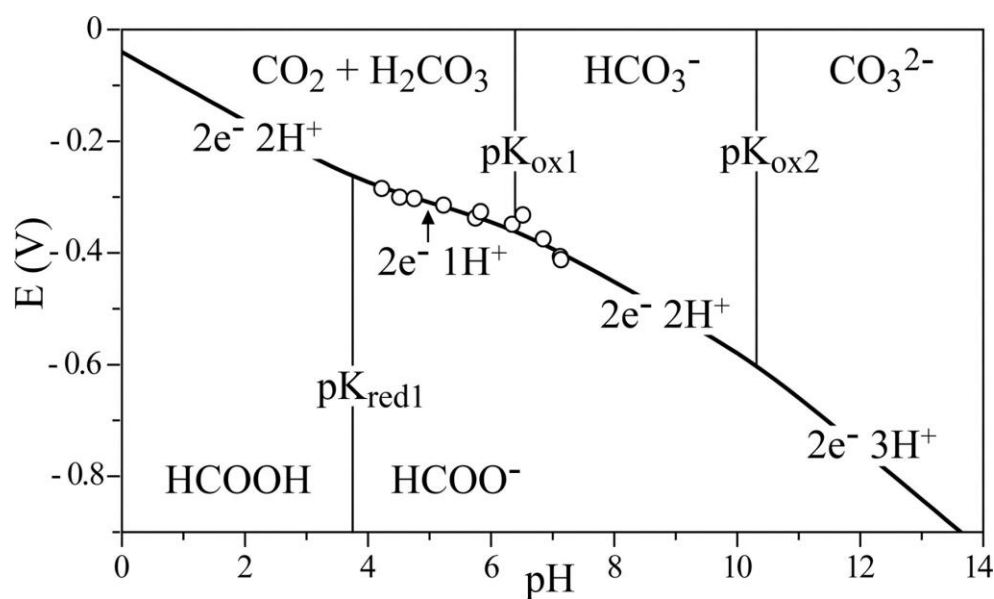


**Figure 2.8:** The CO<sub>2</sub> Pourbaix diagram shows the difference between forming formic acid (HCOOH) and formate (HCOO<sup>-</sup>), when significant cathodic potentials are applied [35].

Many authors mistakenly report HCOOH as a product, but the typical conditions clearly point to the HCOO<sup>-</sup> predominance region. Furthermore, it should be noted that the local pH may be playing a role in the catalysis of CO<sub>2</sub>. Significant HER on the catalyst surface, as well as production of CO<sub>2</sub> derived products, result in a drastic local pH increase. The local pH increases, due to the production of OH<sup>-</sup> anions, and thus heavily relies on the current density during the ERC. It has been shown, however, that the production of alcohols and ethylene on copper

surfaces is more favorable in high pH environments [36]. Little work has been done investigating the effects of pH, solution chemistry, and solution concentration on other metallic surfaces.

Tailoring the surface morphology of metal catalysts has also been shown to vary the distribution of products formed via the ERC. Continuing our focus on Cu, the production efficiency of useful products typically increases upon nanostructuring, due to the general availability of a variety of facets with different surface energy, enabling adsorption of various intermediates. Cu nanoparticles for instance showed an efficiency as high as 75% for CO methanation, but only at high overvoltages [37]. In contrast, high surface area oxide-derived Cu surfaces show a propensity to form CO at low overvoltages, achieving over 90% efficiency [38]. Copper nanofoam architectures have shown promise in increasing the selectivity to formate [39]. Overall, the modulation of the surface topography is capable of exposing more catalytically active reaction sites, in turn benefitting the selectivity and the efficiency of the ERC.

#### **2.4) Recent Research and Motivation for Work on the Electrochemical Reduction of CO<sub>2</sub>**

The amount of literature relating to the electrochemical reduction of CO<sub>2</sub> has soared in recent years with over 1500 publications since the beginning of 2010. **Figure 2.9** shows the publication count on this topic, evidencing a steady increase, due to the increased efforts in renewable energy and sustainability innovation.

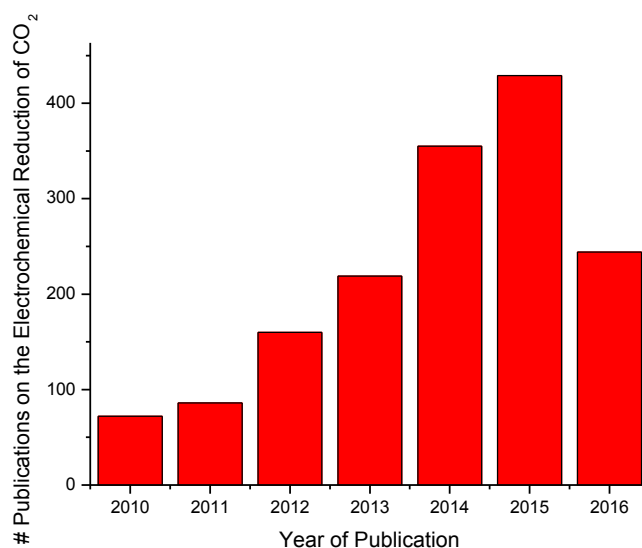


**Figure 2.9:** The number of publications by year (since 2010) on “The Electrochemical Reduction of CO<sub>2</sub>.” Metrics taken from Web of Science™ and include results through the end of July, 2016.

Despite the copious amount of research, in recent years, limited studies relating CO<sub>2</sub> reduction to reaction mechanisms, bimetallic catalysis, and/or dendritic morphologies can be discerned.

Besides the reaction mechanisms proposed by Hori [34] and Norskov [31], and reviewed recently with work by Kortlever [33] and Asthagiri [40], little has been done to provide links between the adsorption of intermediates to both the end product distribution and the atomic layout on catalyst surfaces. Single crystal Cu surfaces reveal varying product distributions and provide the inspiration for extending those studies to more complex bimetallic surfaces [41-43].

Cu is unique because it exhibits the lowest overvoltage for the CO\* to CHO\* step (an asterisk indicates that the species is adsorbed at the catalyst). Furthermore, it is predicted that

CO\* cannot be kept adsorbed at high overpotential: a second metal with stronger oxygen affinity is needed to enable both adsorption of CO and H at suitable potentials [44]. Therefore, it may be useful to couple to Cu more oxyphilic materials from the sp metals block: Sn, In, Bi, Sb. This could result in more sluggish hydrogen evolution while enhancing the adsorption strength of species like CO and CHO to facilitate successive hydrogen addition. Through DFT calculations, it was shown that alloying a d-metal (i.e. Cu) with an sp-metal (i.e. In) may assist in lowering the energy barrier for formation of certain products, more specifically CO and formate [45]. However, little has been done to prove this experimentally.

Finally, studies of electrocatalysts with dendritic surface morphologies have been scarce. Increased formate efficiency was revealed on nanofoams made of copper dendrites [39]. Palmore explored relative quantities of atomic planes, comparing nanofoams to bulk Cu with XRD. More recently, hexagonal-Zn dendrites showed a propensity to form CO at high efficiencies and current densities over traditional Zn electrodes [46]. XRD comparison of these Zn electrodes showed no noticeable differences, but in-situ surface characterization using XAS (X-ray Adsorption Spectroscopy) techniques provided new insight into connecting catalyst valency to product distribution. Furthermore, Sn dendrites have been explored for CO<sub>2</sub> reduction activity [47]. Other than these select examples, CO<sub>2</sub> electrocatalysis investigations on dendritic catalysts have been sparse, despite obvious advantages of very high surface area over traditional materials.

Overall, economical and efficient electrocatalysts that slow down HER, tune the selectivity towards value-added products, and remain stable over time, are desired in order to enable widespread deployment of a practical process for the electrocatalysis of CO<sub>2</sub>. In order to fill the aforementioned gaps in knowledge, we provide insight into mechanistic events on

bimetallic catalysts with unique dendritic morphologies. The bimetallic systems of Cu-In and Cu-Bi are explored in this work.

## References:

- [1] Hamann, C. H., Hamnett, A., & Vielstich, W. (2007). *Electrochemistry*, second, completely revised and updated.
- [2] Srinivasan, S. (2006). *Fuel cells: from fundamentals to applications*. Springer Science & Business media.
- [3] Kolb, D. M. (2002). An atomistic view of electrochemistry. *Surface Science*, 500(1), 722-740.
- [4] Bockris, J. O. M., & Reddy, A. K. (2001). *Modern Electrochemistry 2B: Electrodics in Chemistry, Engineering, Biology and Environmental Science* (Vol. 2). Springer Science & Business Media.
- [5] Jones, D. A. (1995). *Principles and prevention of corrosion (2<sup>nd</sup> edition)*. Macmillan.
- [6] Bagotsky, V. S. (Ed.). (2005). *Fundamentals of electrochemistry* (Vol. 44). John Wiley & Sons.
- [7] Brenner, A. (2013). *Electrodeposition of alloys: principles and practice*. Elsevier.
- [8] Cavallotti, P. L., Nobili, L., & Vincenzo, A. (2005). Phase structure of electrodeposited alloys. *Electrochimica acta*, 50(23), 4557-4565.
- [9] Yang, G. H., Geng, K. W., Zeng, F., & Pan, F. (2005). Formation of metastable phases and their effect on the magnetic properties of Co-Cu multilayers. *Thin solid films*, 484(1), 283-288.
- [10] Donepudi, V. S., Venkatachalapathy, R., Ozemoyah, P. O., Johnson, C. S., & Prakash, J. (2001). Electrodeposition of copper from sulfate electrolytes: Effects of Thiourea on resistivity and electrodeposition mechanism of copper. *Electrochemical and Solid-State Letters*, 4(2), C13-C16.
- [11] Valsiūnas, I., Gudavičiūtė, L., & Steponavičius, A. (2005). Bi electrodeposition on Pt in acidic medium 1. A cyclic voltammetry study. *Chemija*, 16, 21-28.
- [12] Zangari, G. (2015). Electrodeposition of Alloys and Compounds in the Era of Microelectronics and Energy Conversion Technology. *Coatings*, 5(2), 195-218.
- [13] Sieradzki, K., & Dimitrov, N. (1999). Electrochemical defect-mediated thin-film growth. *Science*, 284(5411), 138-141.
- [14] Berg, J. C. (2010). *An introduction to interfaces & colloids: the bridge to nanoscience*. World Scientific.
- [15] Reinke, P. (2012). *Inorganic nanostructures: properties and characterization*. John Wiley & Sons.
- [16] López, C. M., & Choi, K. S. (2006). Electrochemical synthesis of dendritic zinc films composed of systematically varying motif crystals. *Langmuir*, 22(25), 10625-10629.
- [17] Léger, C., Servant, L., Bruneel, J. L., & Argoul, F. (1999). Growth patterns in electrodeposition. *Physica A: Statistical Mechanics and its Applications*, 263(1), 305-314.
- [18] Ertl, G. (2010). *Reactions at solid surfaces* (Vol. 14). John Wiley & Sons.



- [19] Karunadasa, Hemamala I., et al. "A molecular MoS<sub>2</sub> edge site mimic for catalytic hydrogen generation." *Science* 335.6069 (2012): 698-702.
- [20] Yang, J., Wang, D., Han, H., & Li, C. (2013). Roles of cocatalysts in photocatalysis and photoelectrocatalysis. *Accounts of chemical research*, 46(8), 1900-1909.
- [21] Greeley, J., Jaramillo, T. F., Bonde, J., Chorkendorff, I. B., & Nørskov, J. K. (2006). Computational high-throughput screening of electrocatalytic materials for hydrogen evolution. *Nature materials*, 5(11), 909-913.
- [22] Lamy, C., Rousseau, S., Belgsir, E. M., Coutanceau, C., & Léger, J. M. (2004). Recent progress in the direct ethanol fuel cell: development of new platinum–tin electrocatalysts. *Electrochimica Acta*, 49(22), 3901-3908.
- [23] Whipple, D. T., & Kenis, P. J. (2010). Prospects of CO<sub>2</sub> utilization via direct heterogeneous electrochemical reduction. *The Journal of Physical Chemistry Letters*, 1(24), 3451-3458.
- [24] Lee, J., Kwon, Y., Machunda, R. L., & Lee, H. J. (2009). Electrocatalytic recycling of CO<sub>2</sub> and small organic molecules. *Chemistry—An Asian Journal*, 4(10), 1516-1523.
- [25] Bevilacqua, M., Filippi, J., Miller, H. A., & Vizza, F. (2015). Recent Technological Progress in CO<sub>2</sub> Electroreduction to Fuels and Energy Carriers in Aqueous Environments. *Energy Technology*, 3(3), 197-210.
- [26] Lim, R. J., Xie, M., Sk, M. A., Lee, J. M., Fisher, A., Wang, X., & Lim, K. H. (2014). A review on the electrochemical reduction of CO<sub>2</sub> in fuel cells, metal electrodes and molecular catalysts. *Catalysis Today*, 233, 169-180.
- [27] Chen, Y., Li, C. W., & Kanan, M. W. (2012). Aqueous CO<sub>2</sub> reduction at very low overpotential on oxide-derived Au nanoparticles. *Journal of the American Chemical Society*, 134(49), 19969-19972.
- [28] Lu, Q., Rosen, J., Zhou, Y., Hutchings, G. S., Kimmel, Y. C., Chen, J. G., & Jiao, F. (2014). A selective and efficient electrocatalyst for carbon dioxide reduction. *Nature communications*, 5.
- [29] Rosen, B. A., Salehi-Khojin, A., Thorson, M. R., Zhu, W., Whipple, D. T., Kenis, P. J., & Masel, R. I. (2011). Ionic liquid–mediated selective conversion of CO<sub>2</sub> to CO at low overpotentials. *Science*, 334(6056), 643-644.
- [30] Sonoyama, N., Kirii, M., & Sakata, T. (1999). Electrochemical reduction of CO<sub>2</sub> at metal-porphyrin supported gas diffusion electrodes under high pressure CO<sub>2</sub>. *Electrochemistry communications*, 1(6), 213-216.
- [31] Peterson, A. A., Abild-Pedersen, F., Studt, F., Rossmeisl, J., & Nørskov, J. K. (2010). How copper catalyzes the electroreduction of carbon dioxide into hydrocarbon fuels. *Energy & Environmental Science*, 3(9), 1311-1315.
- [32] Nørskov, J. K., Rossmeisl, J., Logadottir, A., Lindqvist, L. R. K. J., Kitchin, J. R., Bligaard, T., & Jonsson, H. (2004). Origin of the overpotential for oxygen reduction at a fuel-cell cathode. *The Journal of Physical Chemistry B*, 108(46), 17886-17892.
- [33] Kortlever, R., Shen, J., Schouten, K. J. P., Calle-Vallejo, F., & Koper, M. T. (2015). Catalysts and reaction pathways for the electrochemical reduction of carbon dioxide. *The journal of physical chemistry letters*, 6(20), 4073-4082.
- [34] Hori, Y. (2008). Electrochemical CO<sub>2</sub> reduction on metal electrodes. In *Modern aspects of electrochemistry* (pp. 89-189). Springer New York.
- [35] Reda, T., Plugge, C. M., Abram, N. J., & Hirst, J. (2008). Reversible interconversion of carbon dioxide and formate by an electroactive enzyme. *Proceedings of the National Academy of Sciences*, 105(31), 10654-10658.
- [36] Hori, Y., Murata, A., & Takahashi, R. (1989). Formation of hydrocarbons in the electrochemical reduction of carbon dioxide at a copper electrode in aqueous solution. *Journal of the Chemical Society, Faraday Transactions 1: Physical Chemistry in Condensed Phases*, 85(8), 2309-2326.

- [37] Manthiram, K., Beberwyck, B. J., & Alivisatos, A. P. (2014). Enhanced electrochemical methanation of carbon dioxide with a dispersible nanoscale copper catalyst. *Journal of the American Chemical Society*, 136(38), 13319-13325.
- [38] Li, C. W., & Kanan, M. W. (2012). CO<sub>2</sub> reduction at low overpotential on Cu electrodes resulting from the reduction of thick Cu<sub>2</sub>O films. *Journal of the American Chemical Society*, 134(17), 7231-7234.
- [39] Sen, S., Liu, D., & Palmore, G. T. R. (2014). Electrochemical reduction of CO<sub>2</sub> at copper nanofoams. *ACS Catalysis*, 4(9), 3091-3095.
- [40] Nie, X., Esopi, M. R., Janik, M. J., & Asthagiri, A. (2013). Selectivity of CO<sub>2</sub> reduction on copper electrodes: the role of the kinetics of elementary steps. *Angewandte Chemie International Edition*, 52(9), 2459-2462.
- [41] Durand, W. J., Peterson, A. A., Studt, F., Abild-Pedersen, F., & Nørskov, J. K. (2011). Structure effects on the energetics of the electrochemical reduction of CO<sub>2</sub> by copper surfaces. *Surface Science*, 605(15), 1354-1359.
- [42] Schouten, K. J. P.; Perez Gallent, E.; Koper, M. T. M. Structure Sensitivity of the Electrochemical Reduction of Carbon Monoxide on Copper Single Crystals. *ACS Catal.* 2013, 3, 1292–1295.
- [43] Hori, Y.; Takahashi, I.; Koga, O.; Hoshi, N. Selective Formation of C<sub>2</sub> Compounds from Electrochemical Reduction of CO<sub>2</sub> at a Series of Copper Single Crystal Electrodes. *J. Phys. Chem. B* 2002, 106, 15– 17.
- [44] Peterson, A. A., & Nørskov, J. K. (2012). Activity descriptors for CO<sub>2</sub> electroreduction to methane on transition-metal catalysts. *The Journal of Physical Chemistry Letters*, 3(2), 251-258.
- [45] Lim, H. K., Shin, H., Goddard III, W. A., Hwang, Y. J., Min, B. K., & Kim, H. (2014). Embedding covalency into metal catalysts for efficient electrochemical conversion of CO<sub>2</sub>. *Journal of the American Chemical Society*, 136(32), 11355-11361.
- [46] Rosen, J., Hutchings, G. S., Lu, Q., Forest, R. V., Moore, A., & Jiao, F. (2015). Electrodeposited Zn dendrites with enhanced CO selectivity for electrocatalytic CO<sub>2</sub> reduction. *Acs Catalysis*, 5(8), 4586-4591.
- [47] Won, D. H., Choi, C. H., Chung, J., Chung, M. W., Kim, E. H., & Woo, S. I. (2015). Rational Design of a Hierarchical Tin Dendrite Electrode for Efficient Electrochemical Reduction of CO<sub>2</sub>. *ChemSusChem*, 8(18), 3092-3098.

# Chapter 3: Experimental Instrumentation and

## Methods

This chapter outlines the various instrumentation, methods, and procedures used for all experiments performed in this work. Details of electrodeposition, characterization of deposited materials, the electrochemical reduction of CO<sub>2</sub>, and effluent ERC product quantification are described in the following.

### 3.1) Electrochemical Setups, Instrumentation, and Software

A Biologic SP-150 single-channel potentiostat was used for all electrochemical measurements and experiments including: electrodeposition investigations, Cyclic Voltammetry (CVs) or Linear Sweep Voltammetry (LSVs), and chronoamperometry (electrolysis of CO<sub>2</sub>, ERC). EC-Lab software was used in conjunction with the Biologic Sp-150, to link and perform these techniques as well as collect and record data for further analysis.

Electrodepositions and Electrochemical Impedance Spectroscopy (EIS) (see **Section 3.6d**) were performed in cylindrical cell setups (**Figure 3.1**) while ERC experiments used a custom-designed electrochemical cell (see **Section 3.3**). Various reference electrodes (REs) were used depending on the experiment and the electrolyte utilized, therein. Mercurous Sulfate Electrode (MSE = +0.64 V vs. SHE, saturated K<sub>2</sub>SO<sub>4</sub>), Saturated Calomel Electrode (SCE = +0.24 V vs SHE, saturated KCl), and Silver Chloride (Ag/AgCl = +0.21 V vs SHE, 3 M NaCl) were used. Various REs were used to avoid contamination (i.e. Cl<sup>-</sup> ions in SO<sub>4</sub><sup>2-</sup> solution and

vice versa) and degradation. For simplicity, all the potential values will be referred to the MSE RE.

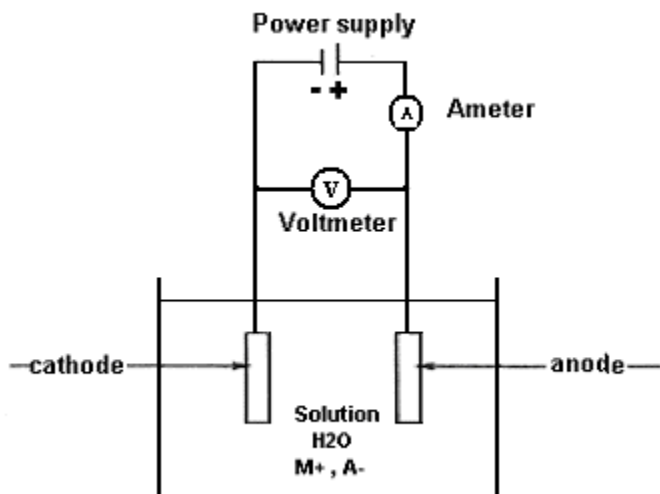


**Figure 3.1:** Simple experimental set up showing electrodeposition of metal  $M^+$  onto the cathode from an electroplating solution with metallic salt MA in  $H_2O$ . Taken from [1].

### 3.2) Synthesis of Electrocatalyst films

#### a.) Copper

Dendritic copper was electrodeposited on Cu substrates (100 nm Cu on Si wafer), using a 10 mM  $CuSO_4$  (Alfa Aesar, 99.99%) + 0.5 M  $H_2SO_4$  (Sigma Aldrich, 98%) + 0.5 M NaCl (Fischer Scientific, 99.99%) solution. Depositions were performed at -0.95 V vs MSE to a charge density of  $1\text{ C/cm}^2$  for a theoretical thickness of  $\sim 370\text{ nm}$ . The addition of chloride ions (from NaCl) to the copper sulfate solution has been shown to increase the degree of grain faceting predominantly at  $\{110\}$  planes. Furthermore, the rate determining step involving a copper (I)

chloride intermediate is believed to induce formation of dendritic copper versus smoother compact films [2].

Pure copper films (100 nm thick) sputtered on Si wafers were also explored in ERC experiments. These were rinsed with acetone and methanol in an ultrasonic bath for 20 minutes. A brief cleanse using dilute (10% v/v)  $\text{H}_2\text{SO}_4$ , followed by a rinse in Milli-Q water (18.2 M $\Omega$ ), was performed immediately prior to each electrolysis experiment.

## **b.) Indium**

Indium was electrodeposited on Au substrates (40 nm Au on Si Wafer), using a 50 mM  $\text{In}_2(\text{SO}_4)_3$  (Alfa Aesar, 99.99%)+ 0.5 M  $\text{H}_2\text{SO}_4$  (Sigma Aldrich, 98%) + 0.5 M NaCl (Fischer Scientific, 99.99%) solution. Depositions were performed at a potential of -2.05 V vs MSE. A charge density of 9 C/cm<sup>2</sup> was required in order to obtain full coverage of indium on the substrate surface, due to the fact that Indium ( $E_0 = -0.34$  V) can be deposited only in parallel with hydrogen evolution .

Pure indium foil (1 mm thick, 99.998% Alfa Aesar) was also used as a comparison. Before each ERC experiment, the foil was mechanically polished using SiC paper incrementally from 240 to 1200 grit. Once a smooth ( $R_f = 1.07$ ) indium surface was achieved, it was cleaned in an identical fashion to that of the smooth (sputtered) copper surfaces.

### c.) Bismuth

Dendritic bismuth was electrodeposited on Au substrates, using a 25 mM  $\text{Bi}(\text{NO}_3)_3$  (Alfa Aesar, 99.99%) + 1.3 M  $\text{HNO}_3$  (Fischer Scientific, 69%) solution [3]. The films were deposited potentiostatically at -0.85 V vs MSE to a charge density of  $5 \text{ C/cm}^2$ , corresponding to a calculated thickness of 3.69 micron at 100% efficiency. Smooth bismuth was also deposited on Au, however using a 100 mM  $\text{Bi}(\text{NO}_3)_3$  (Alfa Aesar, 99.99%) + 1 M  $\text{HNO}_3$  (Fischer Scientific, 69%) solution (Sigma Aldrich, 70%) [4]. The growth was performed at -0.5 V vs MSE to a charge density of  $5 \text{ C/cm}^2$ .

Increasing the  $\text{Bi}^{+3}$  concentration in the electroplating solution helped to attenuate diffusion limited conditions for the reducing metal ions that would ultimately induce a dendritic morphology. The more positive plating potential in the latter case also contributes to a slower, more compact, deposition process.

### d.) Copper-Indium

Copper-indium alloys were electrodeposited from an acidic electrolyte containing 0.5 M  $\text{H}_2\text{SO}_4$  (98%, Sigma Aldrich), 0.1 M  $\text{In}_2(\text{SO}_4)_3$  (Alfa Aesar, 99.99%), and 1 mM  $\text{CuSO}_4$  (Alfa Aesar, 99.99%) [5]. Alloy growth was carried out at constant potential onto 100 nm thick Au films sputtered on Si wafers, coated first with a 5 nm Ta adhesion layer. Alloy composition was tuned by varying the applied potential between -1.45 V and -1.75 V vs MSE, in order to determine appropriate conditions to prepare 20, 40, 60, and 80 at% indium alloys [5]. Deposition time was consistently 20 minutes, to produce dendritic constructions between 500 nm and 20 micron in thickness across all compositions (see **Figure 4.1**).

### e.) Copper-Bismuth

Dendritic copper-bismuth alloys were also produced using electrodeposition. Several copper-bismuth plating solutions, with distinct metal ion concentrations, were utilized in order to synthesize alloys across the entire binary composition range. The use of several solutions was made necessary by the close standard potentials of  $[\text{Cu}^{2+}]$  (+0.34 V) and  $[\text{Bi}^{3+}]$  (+0.31 V), which led to a limited sensitivity of alloy composition on potential. A 0.5 M  $\text{HNO}_3$  (Fischer Scientific, 69%) base solution was used before adding metal salts to a given solution. Across all solutions used, the total metal ion concentration remained constant at 20 mM adding both  $[\text{Cu}^+]$  and  $[\text{Bi}^{3+}]$  (See **Figure 5.1**).  $\text{Cu}_2\text{O}$  (Alfa Aesar, 99.99%) and  $\text{Bi}(\text{NO}_3)_3$  (Alfa Aesar, 99.99%) were used as the metallic salts.

The copper-bismuth electrocatalysts were grown at a constant potential of -1.45 V vs MSE using gold substrates (40 nm) on silicon wafers. The alloys were deposited on substrates with a nominal area of around 3  $\text{cm}^2$  and to a charge density of 4  $\text{C}/\text{cm}^2$  corresponding to an average thickness of 4.57 micron. Alloys of selected compositions (20, 40, 60, and 80 at% Bi) were fabricated at room temperature with stirring.

### 3.3) Custom Electrochemical Cell for the Electrochemical Reduction of $\text{CO}_2$

ERC experiments were performed in a custom electrochemical cell designed in house (**Figure 3.2**). This consisted of a two compartment cell with either an anion exchange membrane (Tokuyama A-006, 28 micron thick) or a proton exchange membrane (Nafion A117, 178 micron thick) separating the two compartments. The top compartment housed the electrocatalyst (WE) and RE ( $\text{Ag}/\text{AgCl}$ ) which were placed approximately 0.5 cm apart. The bottom compartment

housed the CE, consisting of a Pt net. The electrolytic solution used in the ERC experiments was 0.1 M  $\text{KHCO}_3$  (Alfa Aesar, 99.9% metals basis), which was purified using recrystallization and vacuum filtration laboratory techniques. A total of 60 mL solution was placed in the top compartment, and 120 mL in the bottom one. The volume of the outer cone headspace was 35 mL. The cell was saturated with high-purity  $\text{CO}_2$  (99.99%, Praxair) and was pumped for 30 minutes prior to every experiment.

The electrocatalyst was mounted onto a copper wire with conductive copper tape (3M, Ted Pella) and insulated with  $\text{Pb-CrO}_3$  paint so that only the electrocatalyst surface was exposed to the electrolyte. The electrocatalyst always faced down towards the membrane (and bottom compartment) to allow a uniform flow of current with minimal resistance.

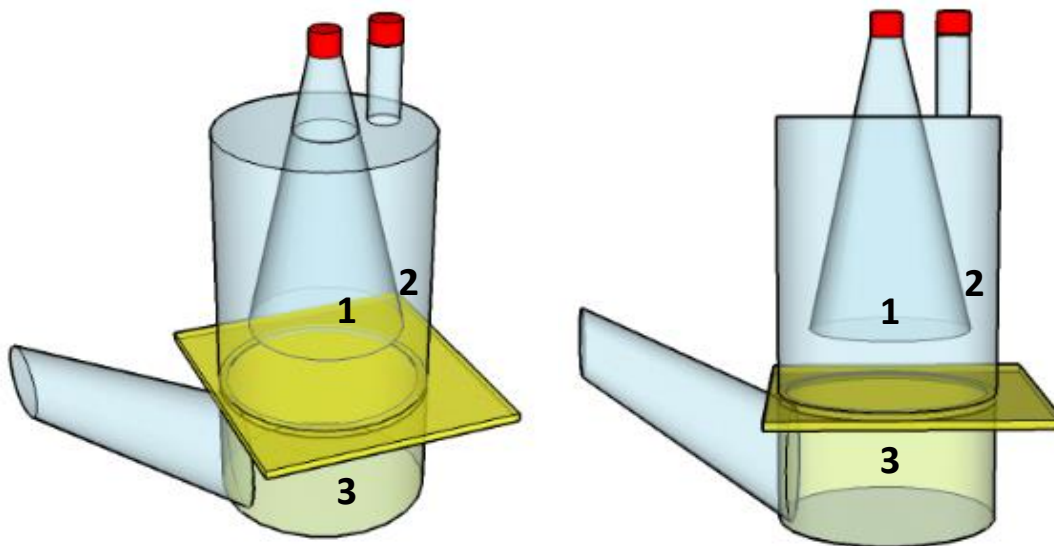


**Figure 3.2:** A schematic of the custom electrochemical cell used for ERC experiments. The yellow film represents the ion exchange membrane (Tokuyama or Nafion) separating the top and bottom compartments, while the red septa show where aliquots of gaseous products were extracted at the conclusion of an ERC experiment. (1) WE position, (2) RE position adjacent to WE (in outer cone), (3) CE position.



At the beginning of each ERC run the inner cone was filled with electrolyte, which was slowly replaced with gaseous products during a given experiment. Thus, a headspace is continuously formed for the duration of an ERC experiment. At the conclusion of an ERC experiment, the gaseous products were syringed out, volumetrically measured, and then analyzed using gas chromatography (see **Section 3.5a**). The volume of the evolved gaseous headspace varied with each set of conditions – electrocatalyst material, electrocatalyst composition, and reduction potential. A gaseous sample was also collected from the outer cone area where gas diffused from the electrolyte (**Figure 3.2**). The gaseous products in the outer cone were also measured to provide a more accurate and complete description of the result of a given ERC experiment. Liquid products were syringed out as well from the top compartment, but also from the bottom compartment if an anion exchange membrane was used for that ERC run. This becomes necessary because the anion exchange membrane slowed steady passage of ERC liquid products (i.e. formate), but did not prevent it altogether. On the other hand, the proton exchange membrane only allowed positively charged ions (i.e.,  $H^+$  and  $K^+$  ions) to pass through and therefore liquid product crossover in the latter case was not a concern.

### **3.4) Electrolysis – The Electrochemical Reduction of $CO_2$**

ERC investigations were executed by performing a method adopted from Jaramillo et al. [6]. A series of measurements were performed in a predefined order for each ERC experiment in order to minimize systematic errors. The series of measurements consisted of: (1) resistance compensation, (2) LSV, (3) resistance compensation, and (4) chronoamperometry. The first resistance compensation was performed to provide an accurate assessment of the applied potential during the electrolysis of  $CO_2$ . The same procedure was repeated after the LSV, as well,

due to changes on the electrocatalyst surface incurred during this technique (i.e. reduction of a native oxide layer, especially readily oxidized materials such as Cu). These resistance compensation steps take into account solution resistance, cell geometry, distance between RE and WE, distance between WE and CE, amongst other factors. LSVs were performed before each ERC run for two reasons: (1) to remove any oxide layer, exposing a truly metallic electrocatalyst surface to a CO<sub>2</sub> saturated electrolyte and (2) to ensure qualitative consistency of identical electrocatalyst materials by observing the position of peaks and HER onset.

### **3.5) Product Identification and Quantification**

#### **a.) Gas Chromatography and Calculation of Dissolved Gases via Henry's Law**

The gaseous CO<sub>2</sub> reduction products were identified by GC-TCD (Gas Chromatography – Thermal Conductivity Detector) with a Shimadzu GC-2014 instrument equipped with a Restek RT-Qbond 30 m × 8 mm fused silica PLOT column (**Figure 3.3**). The instrument was equipped with a 0.5 mL injection loop in which the sample passed through three columns in series (Hayesep T 80/100 mesh 0.5 m × 2.0 mm, Supelco 60/80 Mesh 5 Å molecular sieve 2.0 m × 2.1 mm, and Hayesep Q 80/100 mesh 1.5 m × 2.0 mm). GC-Solution software was used to record chromatograms of injected gaseous mixtures as well as subsequent quantification. 1 mL aliquots, of gaseous products were directly injected into the sample loop for quantification. If samples were less than 1 mL, CO<sub>2</sub> would be used as the balance. This addition was required in order to completely saturate the sample loop as well as push out any gaseous sample that remained from a previous injection. Failure to do this may result in skewed quantification of gaseous products.



**Figure 3.3:** Shimadzu GC-2014 instrument used for gas product analysis.

Injected gaseous product samples were identified and quantified based on differences in thermal conductivity in reference to the carrier gas flowing through the GC. Most gases have thermal conductivities significantly less than that of He, the typical carrier gas used with GC, and therefore elicit a detectable signal that can be quantified. However, an Ar carrier gas was necessary in quantifying  $H_2$  gas, a significant by product in the ERC, due to  $H_2$  thermal conductivity being similar to that of He [7].

The injected gas mixture shows peaks at different retention times based on the interaction of individual gases with each other as well as with the stationary phase (porous polymer resins within the three columns) of the GC. Other factors such as temperature, flow rate, column setup

and length, and relative amounts of gases can affect the retention time at which the product gases elute on the resulting chromatogram. Authentic standards (Praxair, 99.99%) of CO, CH<sub>4</sub>, C<sub>2</sub>H<sub>4</sub>, CO<sub>2</sub>, and H<sub>2</sub> were injected individually to accurately pinpoint the retention times; in addition, selected gas mixtures were tested to determine any shift due to interactions. The retention times of the relevant products and air, in both carrier gases, are highlighted in **Table 3.1**.

Gas	Retention Time (min)
CO <sub>2</sub>	1.5
C <sub>2</sub> H <sub>4</sub>	2.1
H <sub>2</sub> (Ar only)	5.2
O <sub>2</sub>	5.5
N <sub>2</sub>	5.7
CH <sub>4</sub>	6.4
CO	6.6

**Table 3.1:** Retention times of various gases regularly detected in the ERC. Air (O<sub>2</sub> + N<sub>2</sub>) is also seen, and is a benign contaminant. H<sub>2</sub> can only be detected when using an Ar carrier gas.

The resulting peaks for the products outlined in **Table 3.1** are integrated and measured. Standards, of known concentration, of these product gases have an associated peak area, and are then used to quantify a product's concentration in an injected sample from an ERC experiment,. Calculations are straightforward as concentration and peak area are linearly proportional to each other. Sample chromatograms showing various product peaks are shown in **Figure 3.4**.

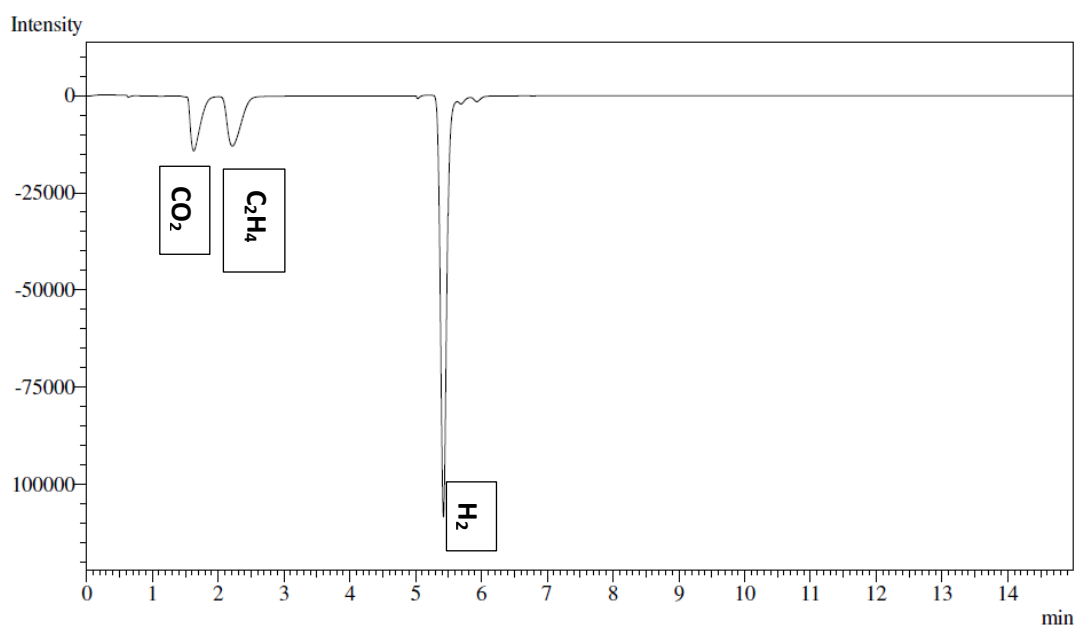
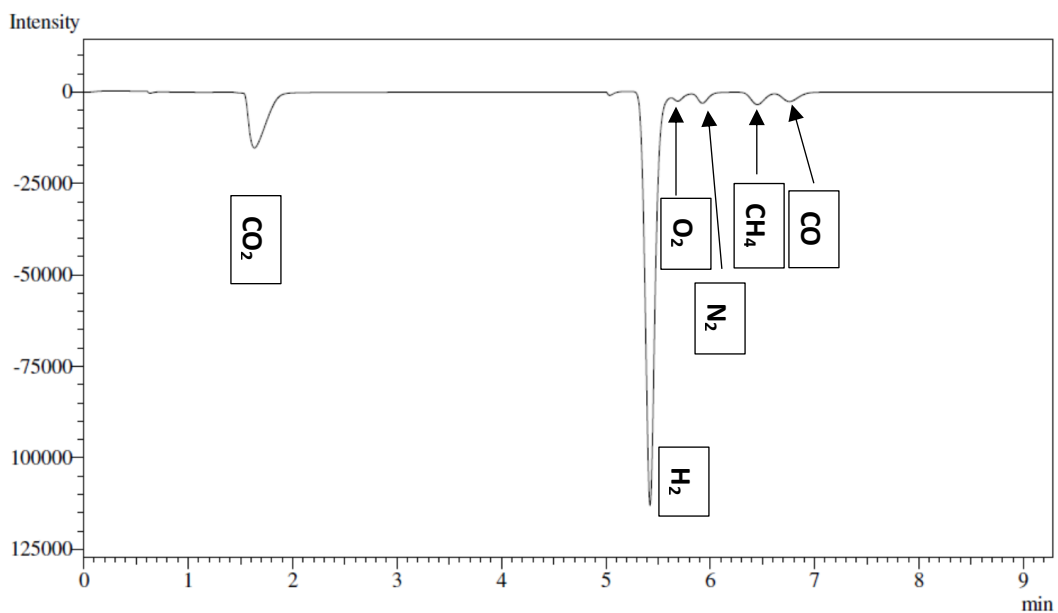


**Figure 3.4:** Sample chromatograms using an Ar carrier gas. All products and air are shown.

Henry's law states that the amount of gas dissolved is proportional to its partial pressure in the headspace. In our experiments, a non-negligible amount of gas is dissolved in the liquid phase. In order to accurately calculate the amount of dissolved gas in the electrolyte, at the

conclusion of a CO<sub>2</sub> electrolysis experiment, Henry's law analyses were performed. The proportionality factors of gas in the system (headspace and dissolved) are known as Henry's law constants. Typical Henry's law constants can be systematically converted to dimensionless Henry's law constants (**Eqn. 3.1**) [8].

$$k_H^{cc} = \frac{c_{aq}}{c_{gas}} = k_H * RT \quad (\text{Eqn. 3.1})$$

Following gas product analysis using GC, the concentration of specific gases in the headspace,  $c_{gas}$ , are easily calculated. From  $c_{gas}$  we can calculate the concentration of dissolved gaseous products,  $c_{aq}$  using tabulated Henry's law constants,  $k_H^{cc}$ , from Sander et al. outlined in **Table 3.2**. Note that the amount of gases being formed during an ERC run is sufficiently small as not to vary significantly the pressure in the reactor.

Dissolved Gaseous Products	$k_h$	$k_h^{cc}$
Hydrogen, H <sub>2</sub>	$7.8 \times 10^{-4}$	$1.9 \times 10^{-2}$
Carbon Monoxide, CO	$9.7 \times 10^{-4}$	$2.4 \times 10^{-2}$
Methane, CH <sub>4</sub>	$1.4 \times 10^{-3}$	$3.4 \times 10^{-2}$
Ethylene, C <sub>2</sub> H <sub>4</sub>	$4.8 \times 10^{-3}$	$1.17 \times 10^{-1}$

**Table 3.2:** Tabulated Henry's Law constants for relevant ERC products. These dimensionless constants,  $k_H^{cc}$ , are defined in **Eqn. 3.1** [8].

These constants therefore assume standard temperature and pressure (25 degrees C, 1 atm) which is a safe assumption of conditions in the laboratory and in the cell, despite the evolution of gases and a subsequent slight pressure increase. This type of Henry's law analysis

has been performed in similar applications – the ERC and photoelectrochemical water splitting [9, 10].

### **b.) Proton ( $^1\text{H}$ ) Nuclear Magnetic Resonance (NMR)**

Yields of aqueous products were determined by  $^1\text{H}$  NMR (10%  $\text{D}_2\text{O}$ , Varian 600 MHz, **Figure 3.5**). Solvent suppression of the  $\text{H}_2\text{O}$  signal was achieved by presaturation and double pulsed -field gradient spin echo pair after the last pulse with the  $180^\circ$  pulse replaced with a composite pulse. In other words, the enormous  $\text{H}_2\text{O}$  peak is minimized in favor of greater sensitivity, especially for products that typically elute on the shoulders of this peak.



**Figure 3.5:** A Varian 600 MHz NMR spectrometer. Dept. of Chemistry, University of Virginia.

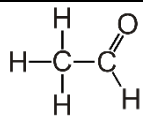
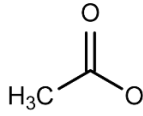
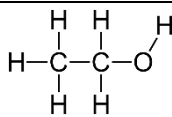
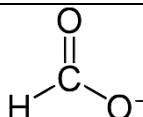
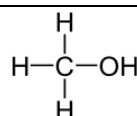
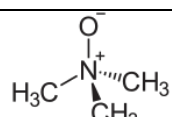
Trimethylamine N-oxide was used as the standard in micromolar quantities to provide direct quantification of any liquid product identified in a given ERC experiment. The standard was chosen due to its placement between potential product peaks on the NMR spectra, as portrayed in **Figure 3.6**. Specifically, 0.1 mL of a 1.33 mM Trimethylamine N-oxide standard was added to 0.5 mL of a liquid product sample, taken at the conclusion of an ERC experiment. Thus, the final concentration of the standard was approximately 0.222 mM and was used to directly quantify the liquid products, by integration and comparison of peaks.

NMR is used to determine various chemical properties of molecules including structure, environment, geometry, and electronic configuration. More specifically, proton NMR is used with respect to  $^1\text{H}$  nuclei present in the target organic molecule. All organic molecules contain  $^1\text{H}$  and therefore can be detected, identified, and quantified with this technique. Peak structure and position (known as chemical shift) as recorded on an NMR spectrum, is determined by the symmetry of molecule, interaction between H atoms, and electronegativity. The chemical shift ( $\delta$ , in ppm) is determined by comparing the sample resonance frequency ( $\nu$ ) to that of a reference (see **Eqn. 3.2**).

$$\delta = \frac{\nu_{\text{sample}} - \nu_{\text{reference}}}{\nu_{\text{reference}}} = \frac{1 \text{ MHz}}{10^6 \text{ MHz}} = 10^{-6} = 1 \text{ ppm} \quad (\text{Eqn. 3.2})$$

**Table 3.3** summarizes several ERC products (and our standards) in terms of these characteristics, while **Figure 3.6** visualizes them on the output spectrum of NMR data processing.



Aqueous Product	Peak Type	Chemical Shift (ppm)	Group	Molecule Visualization
Acetaldehyde	Doublet	2.25	CH <sub>3</sub>	
	Quartet	9.69	C-H	
Acetate	Singlet	2.08	CH <sub>3</sub>	
Ethanol	Quartet	3.67	CH <sub>2</sub>	
	Triplet	1.19	CH <sub>3</sub>	
Formate	Singlet	8.38	C-H	
Methanol	Singlet	3.37	CH <sub>3</sub>	
Trimethylamine N-Oxide	Singlet	3.52	(CH <sub>3</sub> ) <sub>3</sub>	

**Table 3.3:** Previously detected liquid products from the ERC [6] and associated peak locations and shapes using our in-house NMR (Varian 600 MHz, <sup>1</sup>H NMR).

Potassium formate was the only liquid identified as product of the ERC on the electrocatalysts under study, as confirmed by use of authentic standards. Formate and the standard (trimethylamine N-oxide) appear as singlets at 8.38 and 3.52 ppm, respectively. Formate has a single <sup>1</sup>H nucleus while our standard has 9 <sup>1</sup>H nuclei in a symmetrical molecule with three methyl (CH<sub>3</sub>) groups. For quantification purposes in determining the concentration of

formate in a given liquid product sample, a 9 to 1 ratio of these  $^1\text{H}$  nuclei must be accounted for. By setting the standard peak area to 9, we account for this ratio and can take the formate peak area and multiply by 0.222 mM (the concentration of the standard) to calculate the concentration of formate effluent from the ERC.

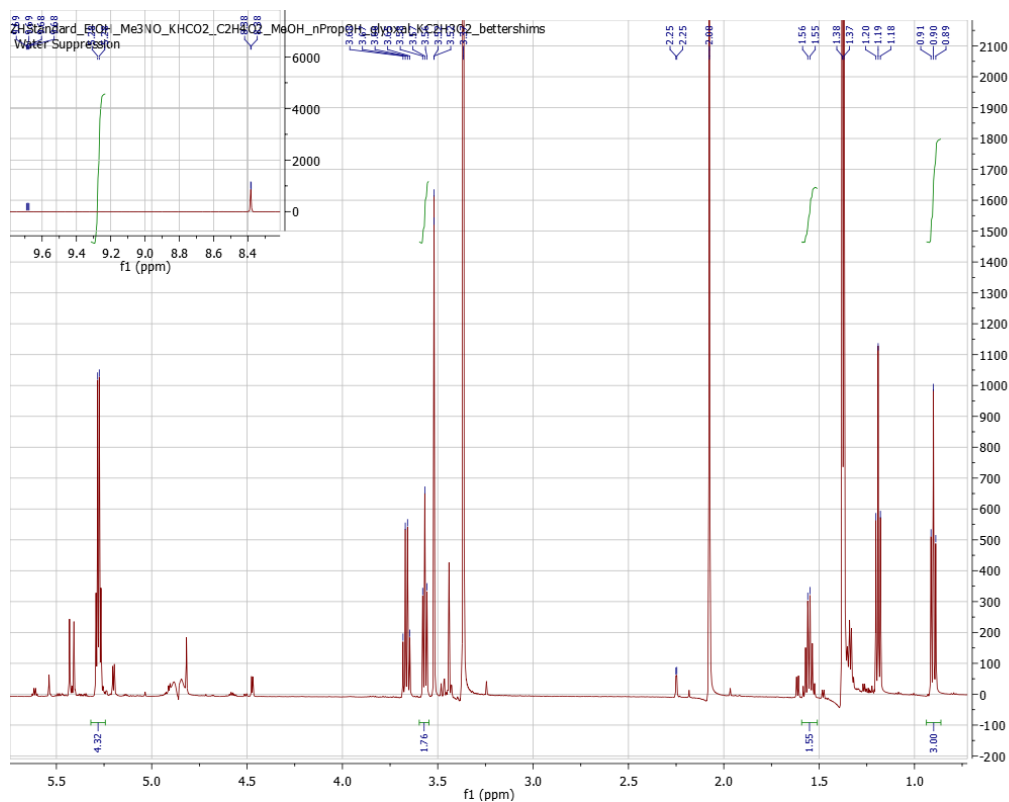


**Figure 3.6:** NMR spectrum showing various possible liquid products outlined in **Table \_\_\_\_**.

### **3.6) Characterization Instrumentation and Techniques**

#### **a.) SEM-EDS**

A FEI Quanta 650 Scanning Electron Microscope (SEM) using a SE-ETD (Secondary Electron – Everhart Thornley Detector) setup was utilized for examining and imaging the surface morphology of the various electrocatalyst materials. In conjunction with SEM, Energy Dispersive X-Ray Spectroscopy (EDS) with Aztec (Oxford Instruments) software was used to determine the composition of the electrodeposited alloys before (and after) their utilization in ERC experiments. An accelerating voltage of 15 kV and a spot size of 4.0 were used as the optimal SEM-EDS parameters to both image the materials successfully as well as quantify the compositions of these electrodeposited materials. These compositional data were confirmed by ICP-OES (Inductively Coupled Plasma – Optical Emission Spectroscopy) techniques which have a higher sensitivity. Unfortunately, ICP-OES (iCAP 7400 Analyzer) is a destructive technique and was used only on selected samples. That being said, EDS is typically accurate to approximately  $\pm 2$  at% depending on observed elements and internal standards [11]. The Aztec software utilizes “ZAF” corrections in order to ensure this level of accuracy -Z is the atomic number correction; A is the absorption correction; and F is the fluorescence correction.

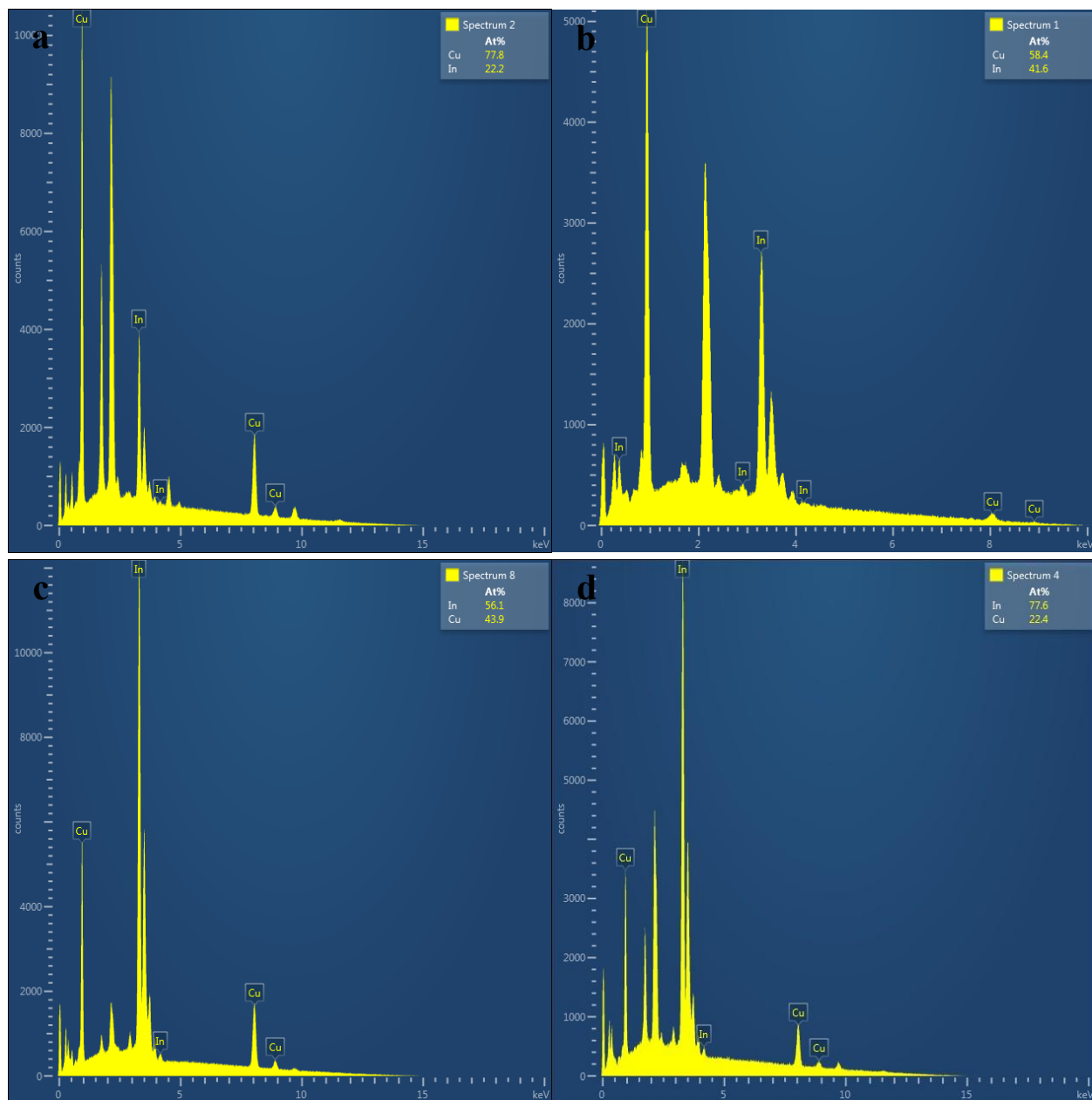


**Figure 3.7:** Sample EDS spectra of compositionally varying Cu-In alloys used for ERC experiments. 22 at% In (a); 42 at% In (b); 56 at% In (c); 78 at% In (d).

## **b.) XRD – Powder and Grazing-Incidence**

Powder x-ray diffraction (XRD) was used to identify the crystal structure of the metals and alloy catalysts under study. A Philips PANalytical X'Pert Pro MPD (Multi-Purpose Diffractometer) was used with a Cu X-ray tube source ( $\lambda$  K $\alpha$  = 0.154 nm), goniometer, and sample spinner configuration. Continuous scans were performed from 20 to 65 degrees ( $2\theta$ ). PDF-4 (ICDD, International Centre for Diffraction Data) software was used for identification of XRD pattern peaks. When the intensities of the substrate peaks were sufficiently strong to eclipse the reflections of the material being investigated GIXRD was employed instead.

Grazing Incidence X-ray diffraction (GI-XRD) measurements were conducted also using a Philips Panalytical X'Pert Pro MPD with an Eulerian Cradle stage using Cu K $\alpha$  radiation ( $\lambda$  = 0.154 nm). The  $2\theta$  scans were acquired at fixed omega angle of  $1^\circ$  using a  $0.05^\circ$  step size at a 1.4s/step rate from 20 to  $80^\circ$  ( $2\theta$ ). GI-XRD provides crystallographic information, just as typical powder XRD does, but is significantly more surface sensitive. In addition, GI-XRD does not give preferential orientation information because the direction of the k vector changes continuously with  $2\theta$ .

## **c.) TEM**

A FEI Titan HR-TEM (High Resolution – Transmission Electron Microscope) was also used for characterizing the dendrite morphology of the Cu-In and Cu-Bi electrocatalysts. The exposed dendrite surfaces have large surface areas and are highly faceted. FFT (Fast Fourier Transform) processing of atomic resolution images was performed on various spots on the dendrite tips in order to determine the crystallinity and atomic layout of the surface.

The distance between a point and the center, of an FFT image, represents the d-spacing ( $d$ ) in reciprocal space. There also exists an identical point directly opposite on the other side of the center, and thus the distance between the two points through the center is equivalent to  $2d$ . TEM software is used to analyze this length in units of  $\text{nm}^{-1}$ , which can then be converted to true d-spacings in real space.

In an identical fashion to identifying XRD peaks, d-spacings calculated from FFT images are used to identify crystallographic planes of the observed surfaces in TEM images. PDF-4 (ICDD, International Centre for Diffraction Data) was used in these endeavors. The viewing direction,  $[ijk]$ , of the plane being examined can also be pinpointed when there is more than one crystallographic plane of the same compound (i.e. **Figure 3.7**,  $\text{Cu}_{11}\text{In}_9$  (313) and (400)) shown on the FFT image. Using the Miller indices of two reflections and by means of simple vector calculus, the viewing direction can be calculated as a vector intersecting the normal of these two reflections. Once the viewing direction,  $[ijk]$ , is determined it can be plugged into the PDF-4 database to simulate an FFT image that ideally would be identical to the one collected using the TEM.

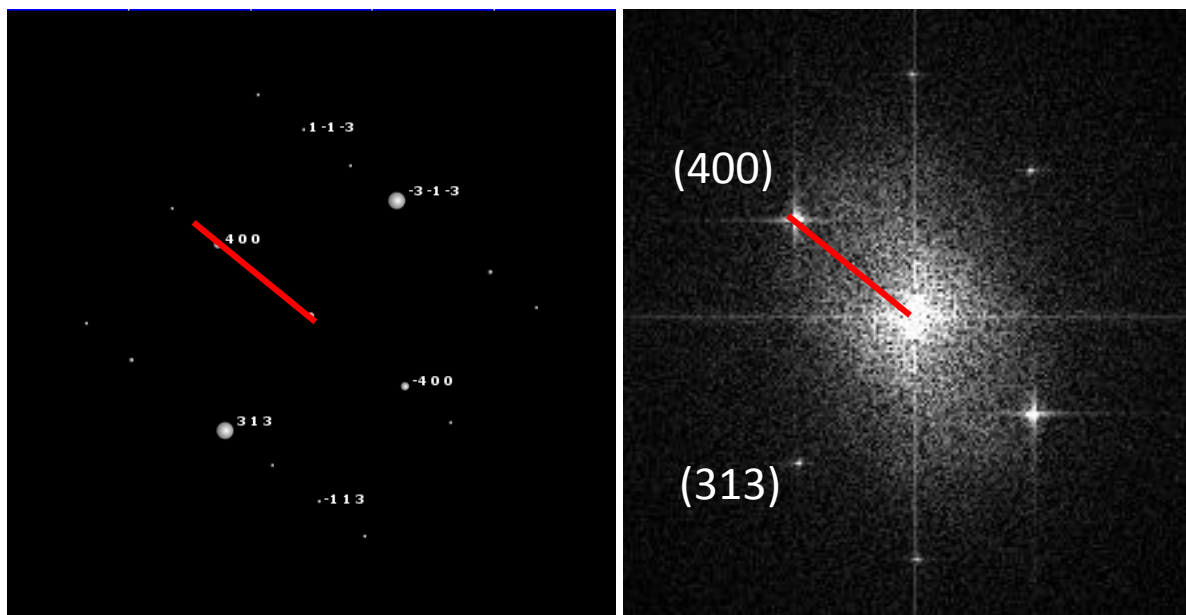


**Figure 3.8:** Matching FFT patterns (left, computer generated from PDF-4 software; right, FFT taken from HR-TEM analysis on a Cu-In dendrite) confirming the intermetallic  $\text{Cu}_{11}\text{In}_9$  (400) and (313) planes on the catalyst surface (83 at% In). The viewing direction was found to be  $[0\ 12\ -4]$ .

#### d.) EIS

A Gamry Ref 600 potentiostat was utilized for EIS (Electrochemical Impedance Spectroscopy) investigations to determine the electrochemically active surface area (EASA) of the various electrocatalyst materials being investigated. A three-electrode setup using a WE, RE, and CE was used. Gamry Framework software was used to analyze the EIS data and perform mathematical fittings in order to determine the  $C_{dl}$  (electric double layer capacitance). EIS was run potentiostatically at OCP (open circuit potential) from a frequency of 100,000 Hz to 0.01 Hz, at a rate of 10 frequencies per decade. The potential was held at OCP for three minutes prior to

each experiment. A 0.1 M HClO<sub>4</sub> electrolyte was used for determining the C<sub>dl</sub> of Cu and Cu-In materials.

The cell is modeled as a Randles circuit, shown schematically in **Figure 3.8**. The elements in the circuit include the solution resistance (R<sub>s</sub>), a double-layer capacitance (C<sub>dl</sub>) in parallel with the charge transfer resistance (R<sub>c</sub>) and a Warburg impedance (Z<sub>w</sub>). The Warburg impedance describes a diffusion circuit element, with current 45° out of phase from the voltage signal.

$$Z_W = \frac{1}{i\omega(C_{dl})} \rightarrow \frac{1}{(i\omega)^\alpha(C_{dl})} \quad (\text{Eqn. 3.3})$$

$$C_{dl} = (CPE) * (\omega_{max})^{\alpha-1} \quad (\text{Eqn. 3.4})$$

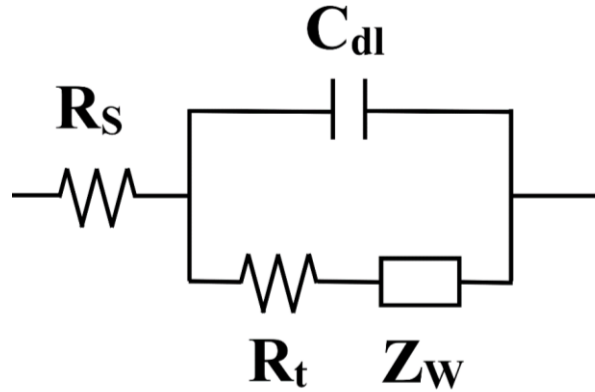


**Figure 3.8:** Ideal Randles circuit visualizing how EIS is performed on various surfaces with respect to electrical responses. The double-layer capacitance, C<sub>dl</sub>, is calculated based on the fitting of EIS data through **Eqns. 3.3 & 3.4**



The capacitive component,  $C_{dl}$ , is replaced with a constant phase element (CPE) due to the non-ideal capacitive response. As a result, the impedance of a capacitor changes to **Eqn. 3.3**, with  $\alpha$  as an empirical constant. When  $\alpha = 1$ , the impedance ideally models a capacitor; when  $\alpha = 0$ , the impedance ideally models a resistor; and when  $0 < \alpha < 1$ , the CPE is used as in this case. Each fit of EIS data, assumes the Randles circuit form with CPE replacing the  $C_{dl}$ . Then, each  $C_{dl}$  value is obtained via **Eqn. 3.4**) using the frequency at the apex on the semi-circular Nyquist plot ( $\omega_{max}$ ) as well as the CPE and  $\alpha$  values obtained from the mathematical fitting of the EIS data.

The ratio of the  $C_{dl}$  values is equivalent to the ratio of the exposed surface areas. The  $C_{dl}$  of the smooth sputtered copper film was used as a reference in order to calculate the true surface area of our high surface area catalysts (**Eqn. 3.5**)

$$\frac{C_{dl}(catalyst)}{C_{dl}(reference)} = \frac{A_{catalyst}}{A_{reference}} \quad (\text{Eqn. 3.5})$$

#### e.) AFM

A Bruker Innova atomic force microscope (AFM), used in tapping mode, was used for imaging the nanoscopic topography of various surfaces in order to determine the roughness factors. The roughness factor,  $R_f$ , is defined as the true surface area divided by the nominal (geometrical) surface area (**Eqn. 3.6**)

$$R_f = \frac{A_{real}}{A_{nominal}} \quad (\text{Eqn. 3.6})$$

The roughness factor was used to determine the true surface area of the studied, smooth sputtered electrocatalyst materials. The determined  $R_f$  values, very close to unity as expected, were used in conjunction with EIS investigations, as  $A_{reference}$ , to further improve accuracy in the calculation of

$A_{\text{catalyst}}$ . Thus, instead of just assuming a  $R_f$  of unity, we determined the actual  $R_f$  values and referenced them to determine  $A_{\text{catalyst}}$  more accurately in EIS investigations.

## References:

- [1] Souad A. M. Al-Bat'hi (2015). Electrodeposition of Nanostructure Materials, Electroplating of Nanostructures, Dr. Mahmood Aliofkhazraei (Ed.), InTech, DOI: 10.5772/61389.
- [2] Shao, W., & Zangari, G. (2009). Dendritic growth and morphology selection in copper electrodeposition from acidic sulfate solutions containing chlorides. *The Journal of Physical Chemistry C*, 113(23), 10097-10102.
- [3] Xiaolong, L., & Zhen, X. (2014). The effect of electrochemical conditions on morphology and properties of Bi<sub>2</sub>Se<sub>3</sub> thick films by electrodeposition. *Materials Letters*, 129, 1-4.
- [4] Sandnes, E., Williams, M. E., Bertocci, U., Vaudin, M. D., & Stafford, G. R. (2007). Electrodeposition of bismuth from nitric acid electrolyte. *Electrochimica acta*, 52(21), 6221-6228.
- [5] Liang, D., Unveroglu, B., & Zangari, G. (2014). Electrodeposition of Cu-In Alloys as Precursors of Chalcopyrite Absorber Layers. *Journal of The Electrochemical Society*, 161(12), D613-D619.
- [6] Kuhl, K. P., Cave, E. R., Abram, D. N., & Jaramillo, T. F. (2012). New insights into the electrochemical reduction of carbon dioxide on metallic copper surfaces. *Energy & Environmental Science*, 5(5), 7050-7059.
- [7] Snavely, K., & Subramaniam, B. (1998). Thermal conductivity detector analysis of hydrogen using helium carrier gas and Hayesep® D columns. *Journal of chromatographic science*, 36(4), 191-196.
- [8] Sander, R. (1999). Compilation of Henry's law constants for inorganic and organic species of potential importance in environmental chemistry.
- [9] Morris, A. J., McGibbon, R. T., & Bocarsly, A. B. (2011). Electrocatalytic Carbon Dioxide Activation: The Rate-Determining Step of Pyridinium-Catalyzed CO<sub>2</sub> Reduction. *ChemSusChem*, 4(2), 191-196.
- [10] Cox, C. R., Lee, J. Z., Nocera, D. G., & Buonassisi, T. (2014). Ten-percent solar-to-fuel conversion with nonprecious materials. *Proceedings of the National Academy of Sciences*, 201414290.
- [11] Goldstein, J., Newbury, D. E., Joy, D., Lyman, C., Echlin, P., Lifshin, E., ... & Michael, J. Scanning electron microscopy and x-ray microanalysis. 2003. ISBN, 306472929, 9780306472923.

## Chapter 4: Electrochemical Reduction of CO<sub>2</sub> – The Copper-Indium System

In this chapter, we demonstrate the capability of copper-indium electrocatalysts to efficiently convert CO<sub>2</sub> to syngas and formate at relatively high efficiency. The catalysts are characterized in order to determine crystallography, atomic surface structure, composition, and surface morphology. Furthermore, their catalytic performances are clarified in actual ERC experiments at various sets of conditions based on potential and composition of the catalyst. Electronic structure of these materials is also qualitatively discussed in order to investigate possible reaction mechanisms. Results shown are compared with the literature to show similar electrocatalytic behavior through experimental evidence and DFT simulations. A majority of this chapter is reproduced from published (or soon to be published) work written by the author.

### 4.1) Structure and Morphology of Catalyst Materials:

Cu-In alloys grow spontaneously with a dendritic morphology; in order to meaningfully compare the pure metals with Cu-In therefore we also targeted deposition of dendritic Cu and In. Electrodeposited Cu showed extensive formation of dendritic features upon chloride addition [1]; electroplated Indium in contrast exhibited only limited roughening, with a roughness factor of 1.1, as determined by AFM (**Figure 4.1**).

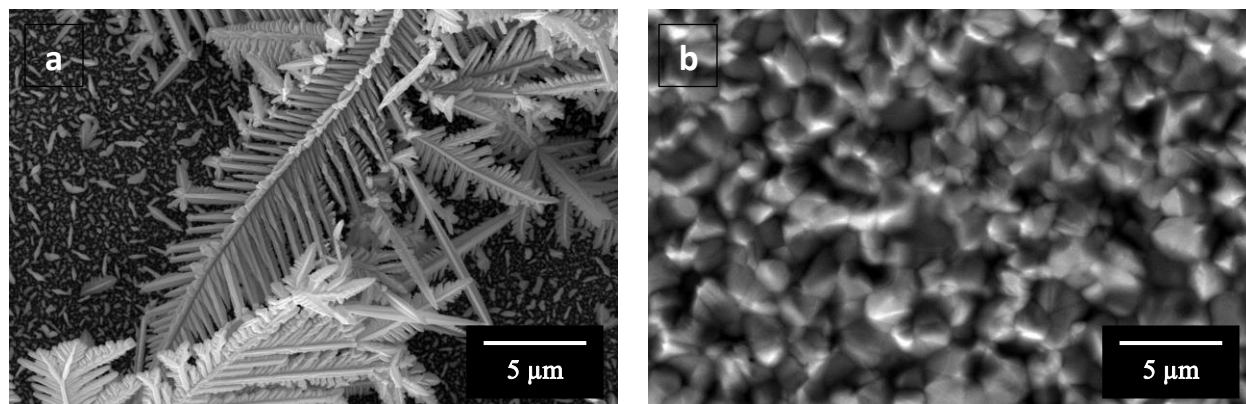


**Figure 4.1:** SEM images of (a) dendritic Cu and (b) electroplated In.

The composition of Cu-In alloys was changed by varying the applied potential between -1.45 V and -1.75 V vs MSE; the composition vs. applied potential is reported in **Figure 4.2**, showing an increase in In fraction with increasing overpotential. Oscillations in the applied potential were due to the intense hydrogen evolution; the alloy composition on the other hand varied slightly over different tests; a criterion of  $\pm 5$  at% from 20, 40, 60, or 80 at% In was required for use in ERC tests. Due to the large difference in the redox potentials of Cu and In, In is codeposited only at a potential where Cu is reduced under diffusion limitations with simultaneous HER, leading to the formation of dendritic features [2, 3]. The applied potential determines the degree of growth instability, resulting in more complex dendrites with increasing overpotential. Thus, differences in the dendritic structure are shown in **Figure 4.3**, where Cu-rich alloys show scattered dendritic islands and indium-rich alloys indeed reveal more extensive dendritic architectures.

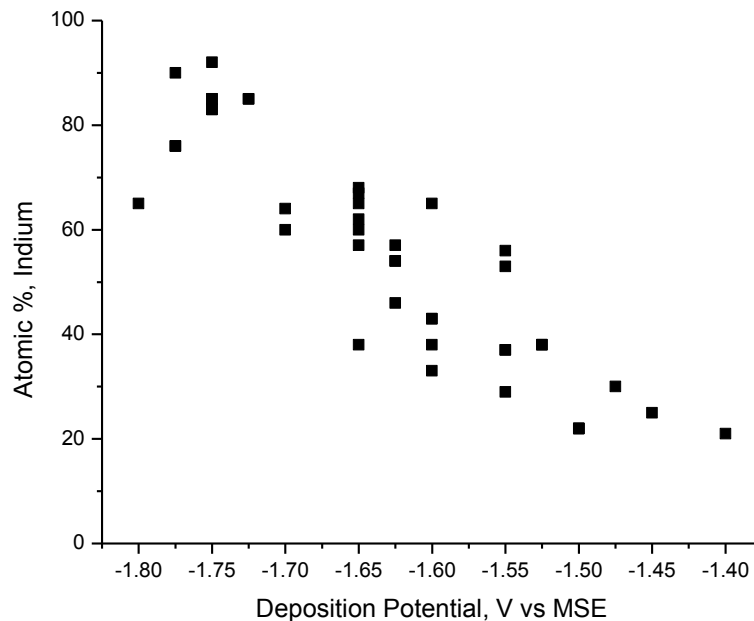


**Figure 4.2:** The compositional dependence of Cu-In alloys on deposition potential using the plating solution containing 1 mM  $\text{Cu}^{2+}$ , 0.2 M  $\text{In}^{3+}$ , 0.5 M  $\text{H}_2\text{SO}_4$ .

Using the secondary electron mode in the SEM, significant contrast is shown in the images in **Figure 4.3**. The dark contrast background represents a relatively smooth, continuous film while the bright features show the various dendritic constructions growing vertically out of the base film. Increasing the applied potential, the Cu-rich dendrites exhibited first  $\{111\}$  then  $\{100\}$  facets, with extensive twinning. Indium-rich dendrites in contrast show a more complex morphology with a variety of different facets, probably due to the formation of non-cubic intermetallic phases.

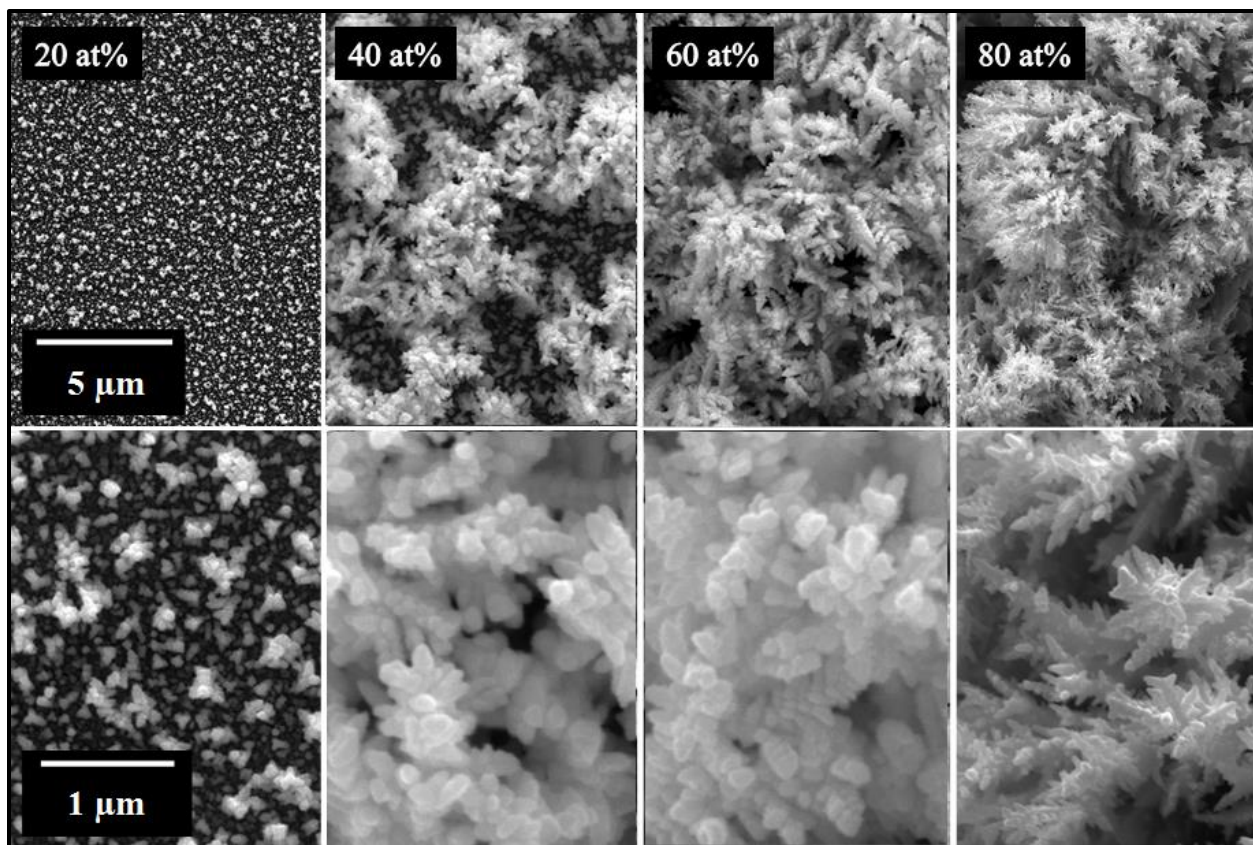


**Figure 4.3:** SEM images of dendritic copper-indium electrocatalysts used in ERC experiments. Top images show overall morphology while bottom images at higher magnification highlight surface details and exposed facets. Indium content (at%) increases from left to right.

**Figure 4.4** shows the cross sectional topography of the various Cu-In electrocatalysts; the continuous layer at the base of the dendrites varies in thickness from 0.2  $\mu\text{m}$  in the Cu-rich film to 1  $\mu\text{m}$  in the In-rich film. Similarly, the thickness of the dendritic films ranges from 0.8  $\mu\text{m}$  to >18  $\mu\text{m}$ .

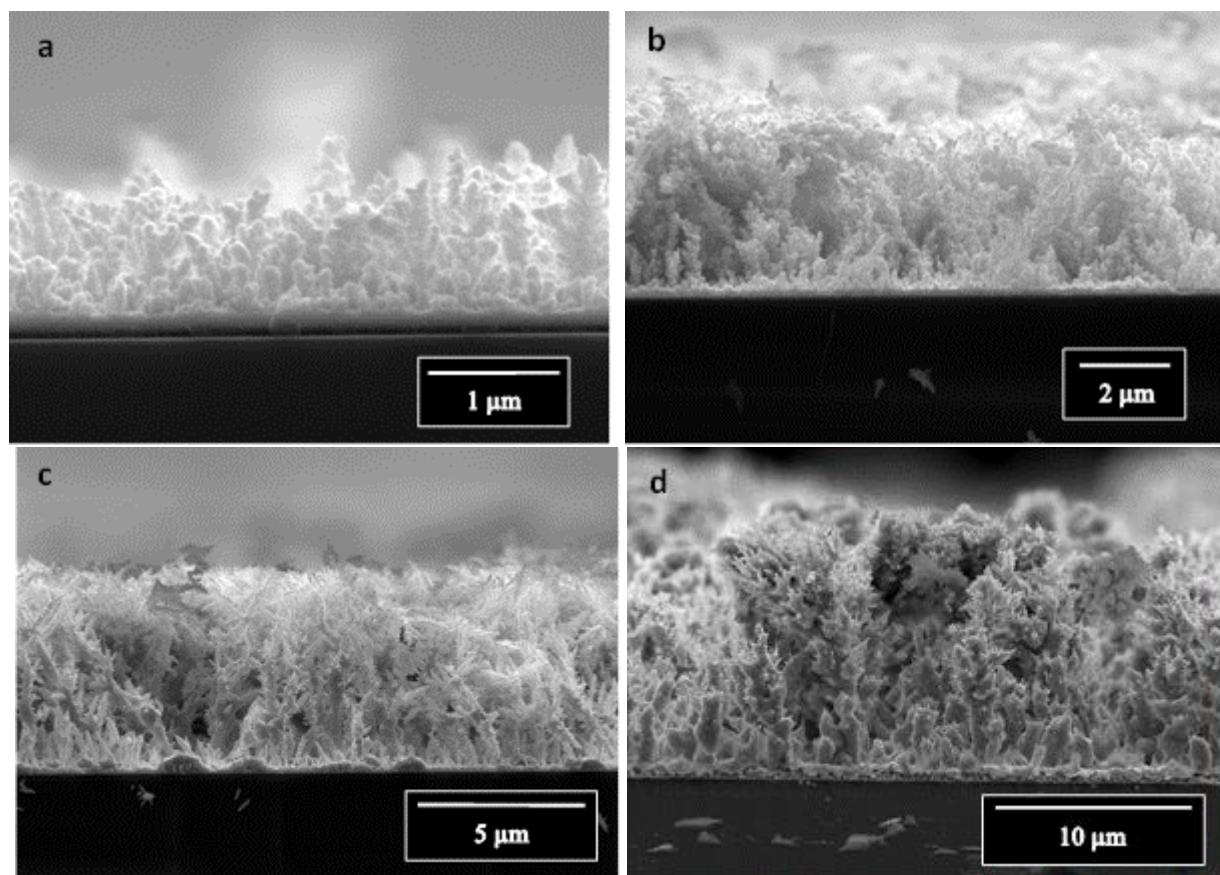


**Figure 4.4:** Cross-sectional SEM images of various electrodeposited Cu-In alloys. (a) 26 at% In; (b) 37 at% In ; (c)60 at% In; (d) 85 at% In.

In order to explore the mechanical and compositional stability of the copper-indium electrocatalysts, morphological and composition studies were performed on all the samples being investigated before and after ERC experiments to quantify any possible degradation resulting from the testing process, exposure to electrolyte, and/or handling. **Figure 4.5** shows the morphology of two representative copper-indium electrocatalysts before and after ERC experiments. No noticeable changes in surface morphology can be seen, suggesting significant mechanical resistance upon operation. Furthermore, little compositional changes are seen (**Table**

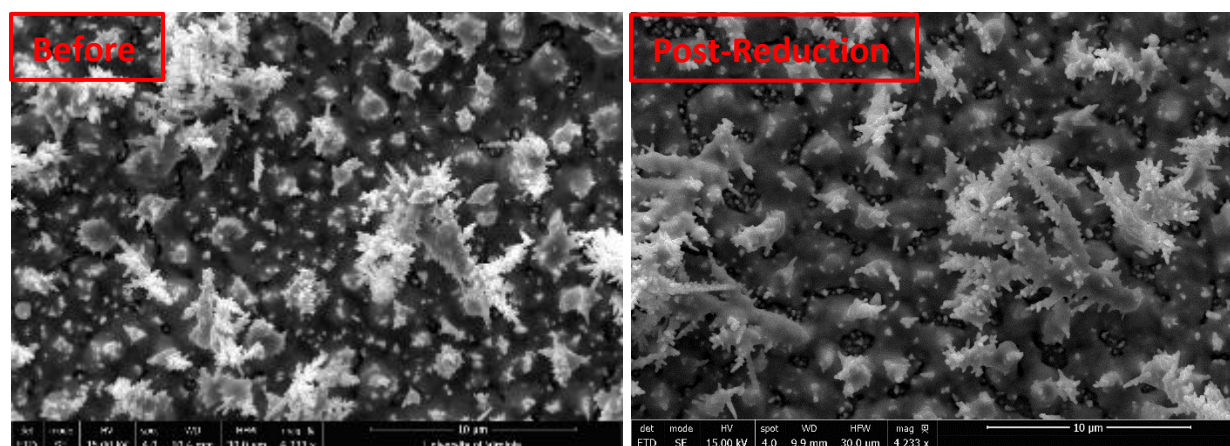


4.1). Despite the chemical and physical durability of these materials, extreme care should be taken due to the dendritic nature of these electrocatalysts.

Sample	Potential (V vs RHE)	at% In Before	at% In After
1	-0.9	80	80
2	-1	39	40

**Table 4.1:** EDS analysis on indium content before and after ERC experiments on two samples of different compositions.

**Sample 1:**



**Sample 2:**

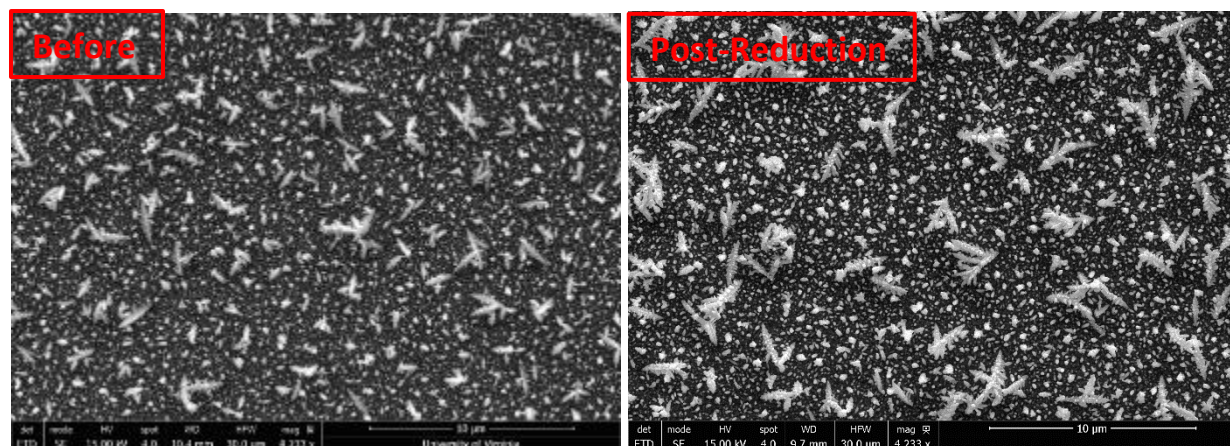


**Figure 4.5:** SEM images showing surface morphology of various Cu-In electrocatalysts before and after ERC experiments (see **Table 4.1**).



XRD patterns of Cu-In alloys are shown in (Figure 4.6). Copper rich alloys (up to 25 at% indium) show a dominant peak at  $2\theta \sim 43^\circ$ , identified as the FCC (111) reflection of the Cu solid solution. A small  $\text{Cu}_{11}\text{In}_9$  (11-2) intermetallic peak is also seen but its intensity is very low relative to the (111) reflection. 37-38 at% In alloys exhibit more intermetallic peaks, including  $\text{Cu}_9\text{In}_4$  (332) (a triclinic structure),  $\text{Cu}_{11}\text{In}_9$  (711) and (402) (with monoclinic structure), and a further shift of the FCC (111) peak.

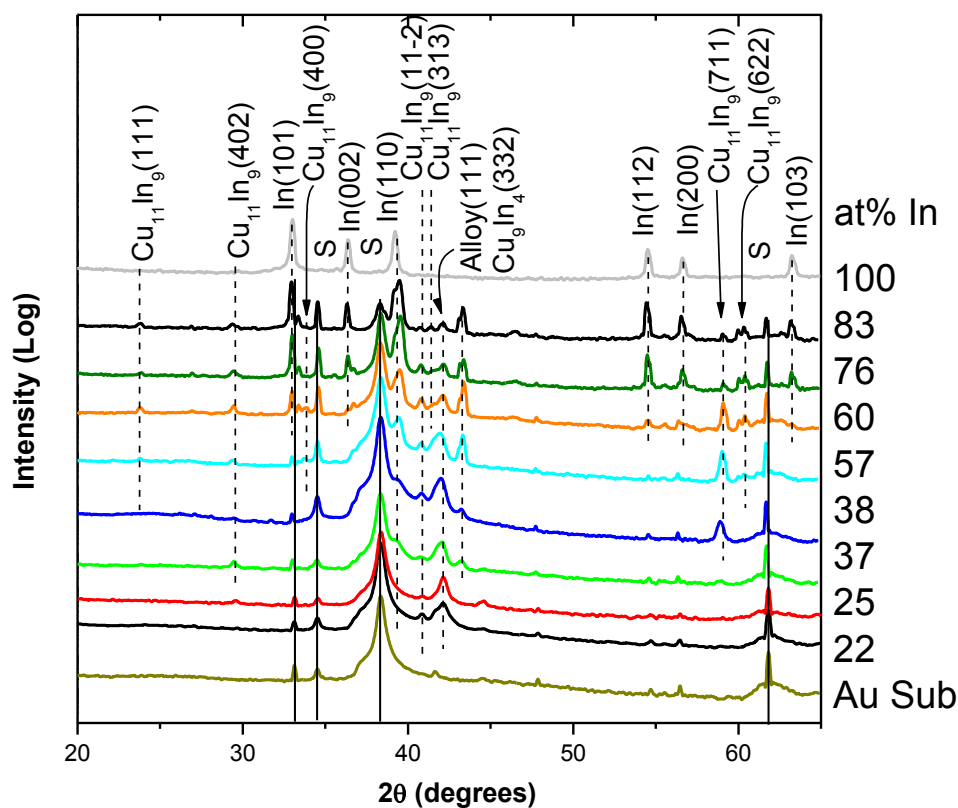


**Figure 4.6:** X-ray diffraction (XRD) patterns for electroplated Cu-In films. Solid lines show the various substrate peaks associated with Au or Si. Dashed lines show reflections from the various phases. Note the logarithmic scale.

**Figure 4.7a** shows an enlargement of the region  $2\theta = 40-44^\circ$ , highlighting the FCC (111) alloy peak. Initially this peak shifts to lower  $2\theta$  angles with increasing In content due to In incorporation above the solubility limit (thermodynamically indium is only soluble in Cu up to  $\sim 1$  at% [4]). By assuming Vegard's law, the actual fraction of In incorporated in the lattice is  $\sim 12.5$  at%, at an overall indium content of 57 at%. Supersaturation of In within the Cu (111) FCC lattice is destabilized when the internal stresses achieve a critical level, such that nucleation of an intermetallic compound ( $\text{Cu}_{11}\text{In}_9$  or  $\text{Cu}_9\text{In}_4$ ) becomes energetically favorable [5]. This is illustrated in **Figure 4.7a** as overall In content increases from 38 to 60 at%, and the (111) reflection begins to revert back towards smaller and more thermodynamically stable lattice constants (low In content) of the solid solution, along with the emergence of Cu-In intermetallic reflections. This is also displayed by the dashed line in **Figure 4.7b** where the (111) alloy phase reaches a critical lattice constant at  $3.733 \text{ \AA}$ , before a sharp decrease is seen. Above 57 at% indium, higher order Cu-In intermetallics appear and the In (110) peak becomes much more defined. As total indium content continues to increase, the intensities of the (111) alloy and Cu-In intermetallic peaks decrease substantially in the wake of elemental indium reflections. In-rich alloy (83 at% indium), exhibit only peaks of elemental indium, with the exception of the  $\text{Cu}_9\text{In}_4$  (332) reflection.

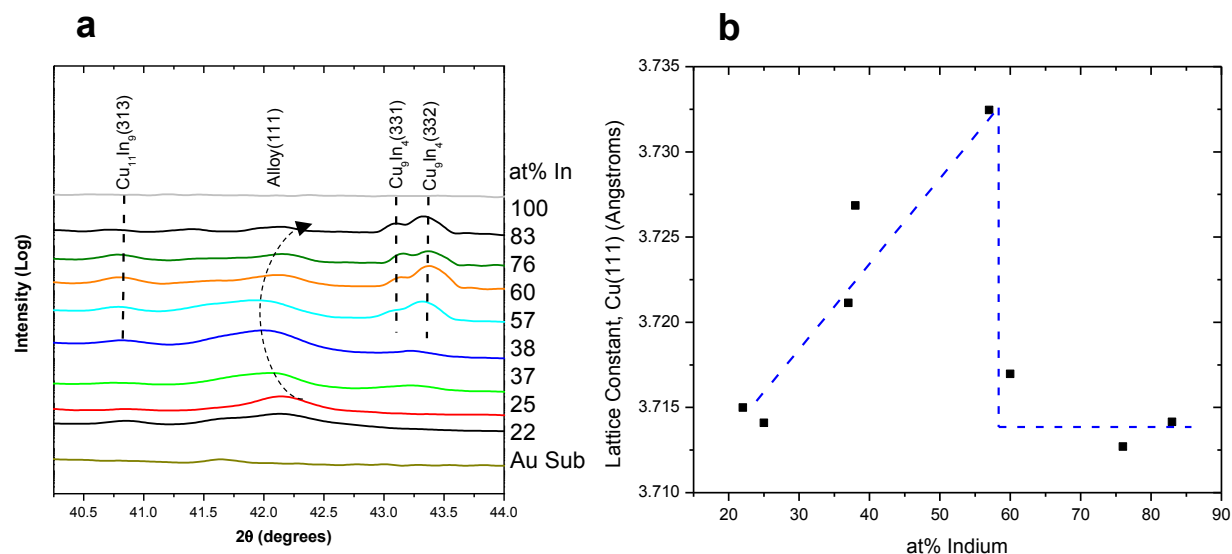


**Figure 4.7:** (a) A zoomed-in diffraction pattern of the Cu-In alloys. The overlaid black dashed line shows the shifting of the alloy (111) reflection with composition. (b) Lattice constant of the alloy (111) peak as a function of indium content in the electrodeposited Cu-In alloy. The blue dashed line shows the trend in lattice constant with average composition.

HR-TEM images of Cu-In dendrites are shown in **Figures 4.8 and 4.10**. A low magnification view of a Cu-In dendrite (80 at% In) is seen in **Figure 4.8a**; uniform dispersion of Cu and In is confirmed via EELS/EDS mapping as shown in **Figure 4.11**. The dendrite tips (**Figure 4.8a**) reveal a consistent tip width of approximately ~50 nm.

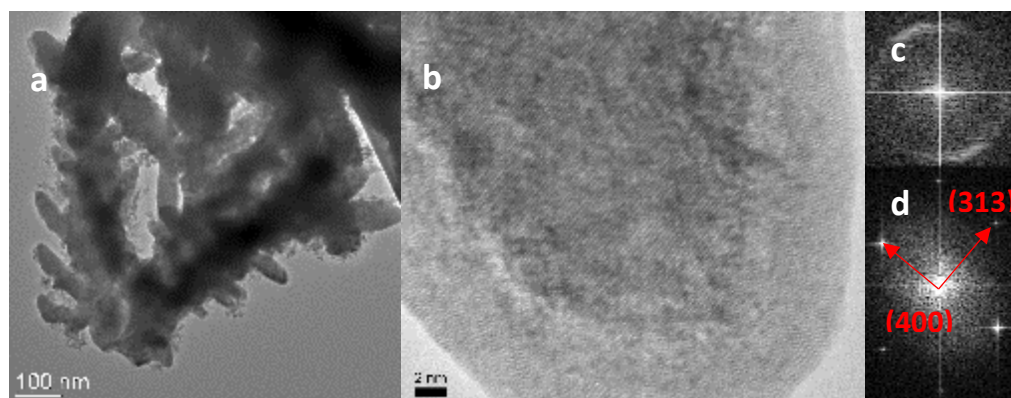
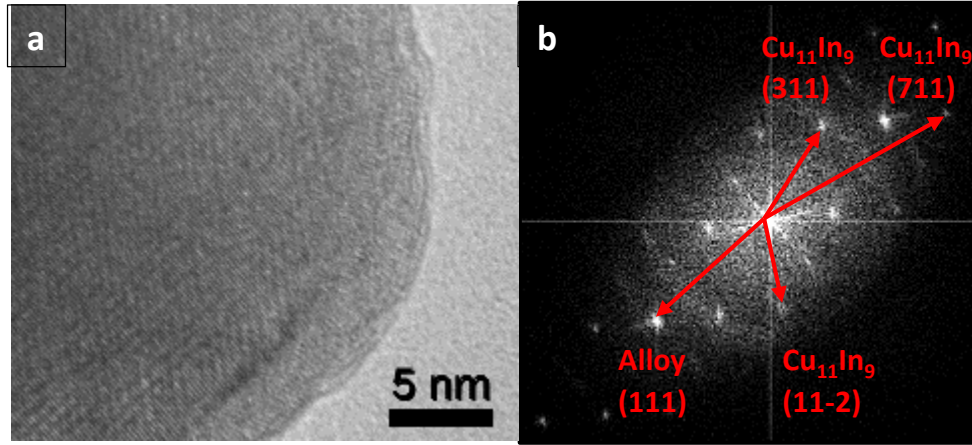


**Figure 4.8:** HR-TEM images of an 80 at% In catalyst: (a) a typical dendrite network, (b) a dendrite tip, and FFT images from both (c) the thin (~5 nm) amorphous surface, and (d) the  $\text{Cu}_{11}\text{In}_9$  intermetallic crystalline bulk.  $d_{(313)} = 2.18 \text{ \AA}$ ,  $d_{(400)} = 2.64 \text{ \AA}$ .

An atomic resolution image of a dendrite tip (**Figure 4.8b**) reveals an amorphous layer ~5 nm thick on the surface, and a well-defined crystalline structure in the interior. These features are confirmed by FFT analysis of the two regions, as shown in **Figure 4.8c** and **4.8d**, respectively. The amorphous surface layer is an oxide film supposedly formed by exposure to air. Recently, it was shown that indium and indium oxide on the surface contribute to the catalytic activity and propensity to produce formate in the ERC [6]. In our case, any oxide layer that may be present is removed during the linear sweep voltammetry (LSV) prior to the ERC experiment, exposing the crystalline region to the solution. The FFT pattern in **Figure 4.8d** reveals measured d-spacings associated with the (400) and (313) reflections of  $\text{Cu}_{11}\text{In}_9$  from XRD patterns shown above, without any evidence of the (111) alloy reflection. This should be expected due to the high In fraction. These assignments were confirmed by reconstructing the FFT images using PDF-4

crystallography software (ICDD, International Centre for Diffraction Data) as shown in **Figure 3.7**.

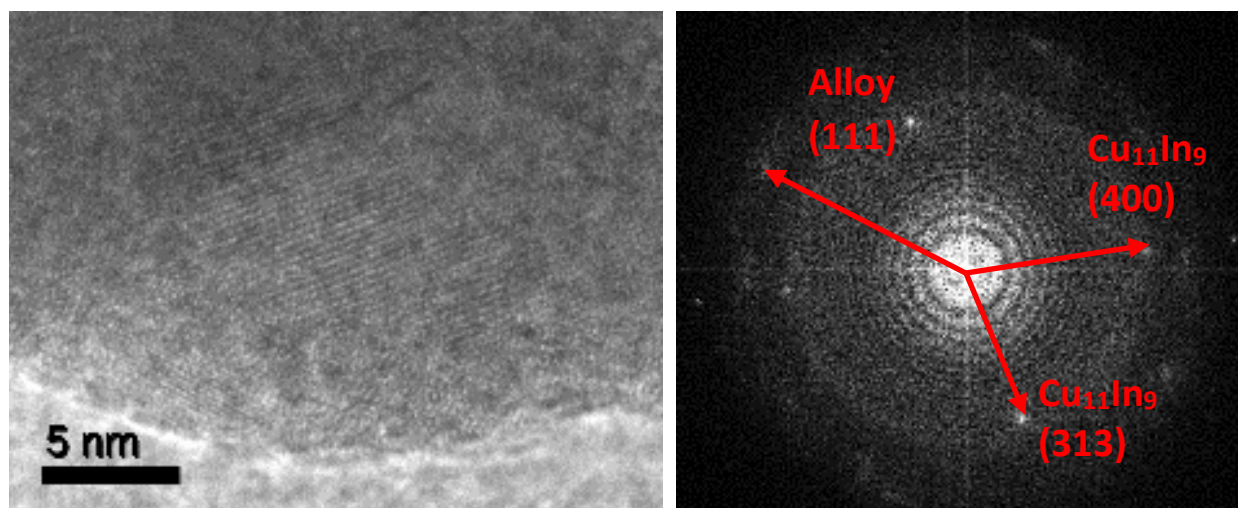


Phase	Reflection	d Spacing
Alloy	(111)	2.15 Å
Cu <sub>11</sub> In <sub>9</sub>	(11-2)	3.71 Å
Cu <sub>11</sub> In <sub>9</sub>	(311)	3.03 Å
Cu <sub>11</sub> In <sub>9</sub>	(711)	1.60 Å

**Figure 4.9:** (a) HR-TEM of a 60 at% indium dendrite tip and (b) the associated FFT image labeled with the relevant crystallographic reflections. The d spacings are assigned in the table below.

**Figure 4.9a** shows the surface region of a 60 at% indium Cu-In dendrite. Again, an amorphous surface layer is distinguishable with a thickness of  $\sim 3$  nm, less than in the previous case, as expected due to the lower In fraction. The FFT pattern (**Figure 4.9b**) reveals a superposition of the Cu<sub>11</sub>In<sub>9</sub> intermetallic and the (111) solid solution reflections. High-order crystallographic planes are seen in the diffraction pattern, including the (311), (11-2), and (711).

As before, the oxide layer is removed prior to CO<sub>2</sub> electrolysis and is therefore neglected. **Figure 4.10** shows a copper rich dendrite tip with atomic resolution and the associated crystallographic reflections obtained from FFT. The expected alloy (111) reflection is revealed but surprisingly the Cu<sub>11</sub>In<sub>9</sub> (313) and (400) reflections are also seen.



Phase	Reflection	d Spacing
Alloy	(111)	2.15 Å
Cu <sub>11</sub> In <sub>9</sub>	(313)	2.18 Å
Cu <sub>11</sub> In <sub>9</sub>	(400)	2.64 Å

**Figure 4.10:** HR-TEM of a 25 at% indium dendrite tip and the associated FFT image labeled with the relevant crystallographic reflections. The d spacings, in Angstroms, are assigned below.

Electron energy loss spectroscopy (EELS) was used in conjunction with EDS mapping to determine the distribution of copper and indium in the dendrites. This dendrite was produced via electrodeposition at -1.75 V vs MSE, and was scraped onto a carbon grid for TEM imaging. No elemental segregation is seen, barring a few copper rich areas in the top right of the dendrite network shown in **Figure 4.11**.

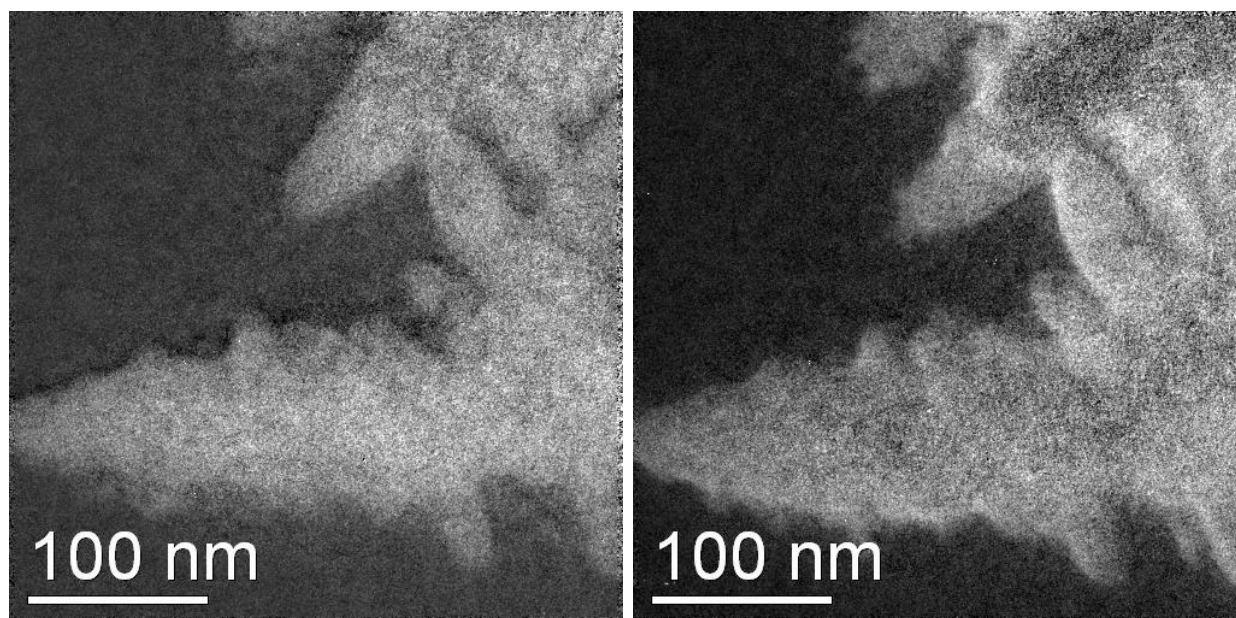


**Figure 4.11:** EELS (electron energy loss spectroscopy) mapping of a dendrite network (83 at% indium). The white color represents the detected element, copper (left) and indium (right).

The high curvature of the dendrite tips is likely to expose a wide range of crystallographic facets to the electrolyte, including those with high Miller indices. It should be noted however that XRD and TEM diffraction are unsuitable to determine the facets exposed to the electrolyte, due to the fact that diffraction methods identify the orientation of crystallographic directions in the bulk, that generally do not coincide with the surface orientation. This identification has been unfortunately often mistakenly made in the literature.

The grain size of various Cu-In reflections were estimated using the Scherrer equation, revealing grain size trends with composition (**Figure 4.12**). Higher order reflections such as  $\text{Cu}_{11}\text{In}_9$  (332) and  $\text{Cu}_{11}\text{In}_9$  (711) showed a larger grain size with increasing indium content. The alloy

(111) reflection showed relatively constant grain size around 15 nm before rising to 25 nm from 60 to 80 at% indium. However, the  $\text{Cu}_{11}\text{In}_9$  (11-2) reflection remained relatively stationary between 20 and 30 nm. Grain size determination from XRD analysis matched with direct TEM measurements of dendritic facets on various Cu-In alloys (length scale of 10s – 100s nm).

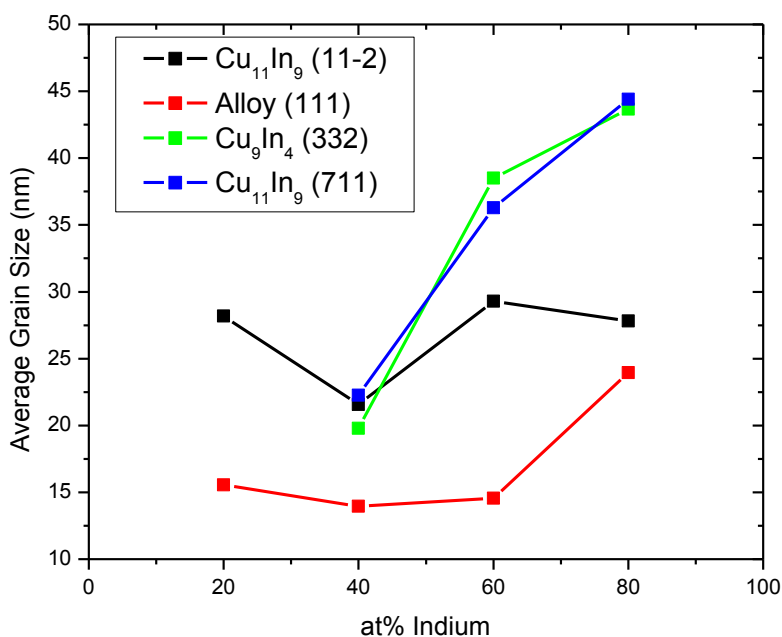


**Figure 4.12:** Grain size of various crystallographic reflections as a function of overall indium content in the film (at% Indium). Grain size was evaluated using the Scherrer equation.

#### 4.2) Electrolysis of $\text{CO}_2$ - Product Distribution and Conversion Rates

**Figure 4.13** shows product distribution as a function of In fraction for various applied potentials. Product distribution as a function of applied potential for the various compositions is displayed in **Figure 4.14**. Pure dendritic Cu produces more than 75%  $\text{H}_2$  at all potentials, while CO and formate are produced in significantly smaller amounts. Methane and ethylene are minor



products, formed at 0.1-1% efficiency (**Figure 4.14**). A tendency to produce predominantly  $H_2$  and formate is revealed also on pure indium surfaces, with CO efficiencies below 10% across all potentials. As overpotential is increased, on pure In, formate reaches its peak efficiency at -1 V, just below 40%. As with pure copper,  $H_2$  is the dominant product on indium at all explored potentials, although not as overwhelming.

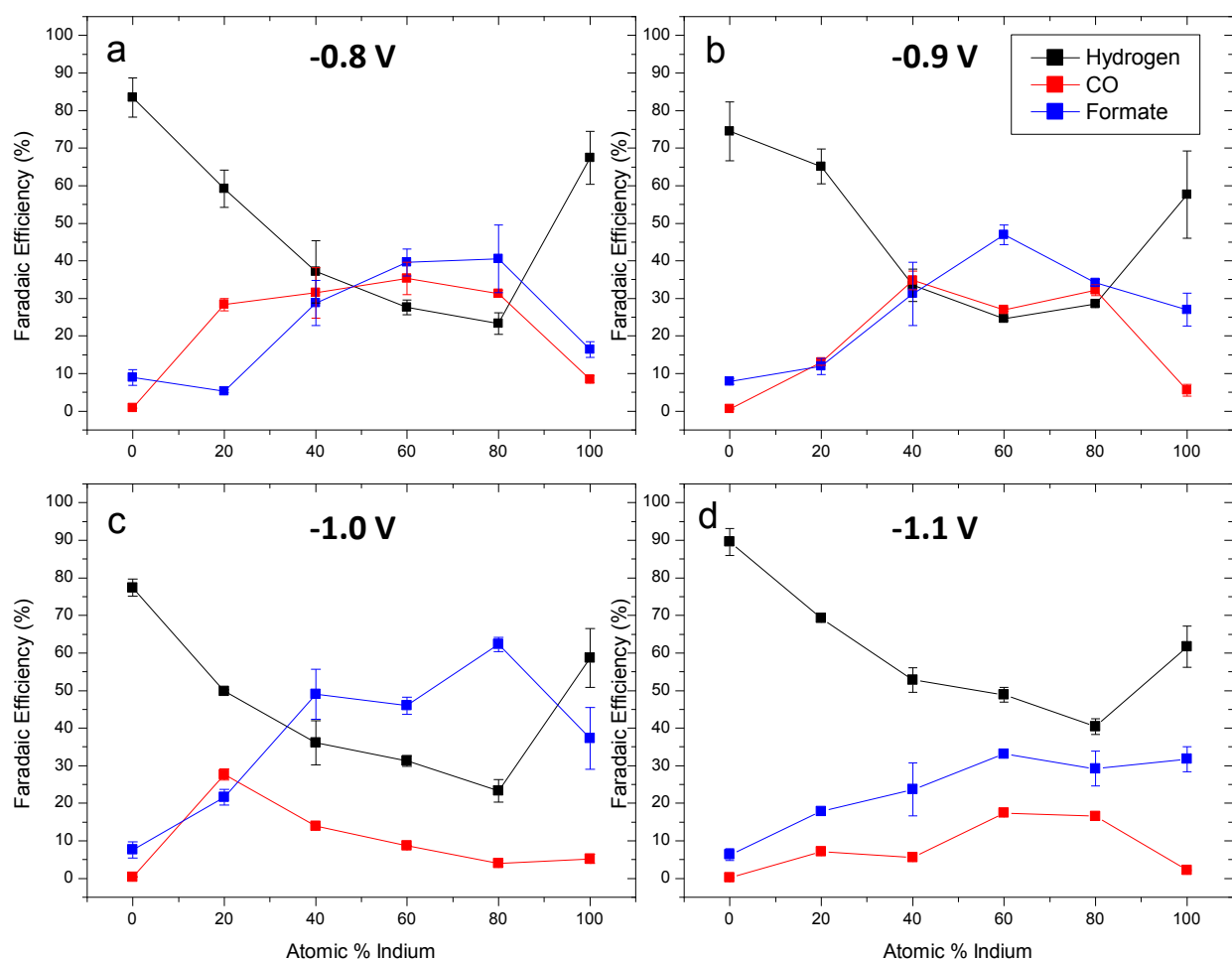


**Figure 4.13:** Product faradaic efficiency as a function of indium content at various potentials (a, -0.8 V vs RHE; b, -0.9 V vs RHE; c, -1.0 V vs RHE; d, -1.1 V vs RHE).

At the most positive potentials of -0.8 and -0.9 V (**Figure 4.13a & 4.13b**), CO is produced steadily at 30% efficiency across a wide range of alloy compositions, while HER is concurrently suppressed to below 35% efficiency. Formate is produced in substantial quantities, with peak efficiencies above 60 % being achieved at 60 or 80 at% In alloys. At -1 V (**Figure 4.13c**), using a 40 at% In alloy composition, the proper ratio of syngas is obtained as well as 50% formate. These are the optimal conditions to enable utilization of the entire product stream, though separation would still be needed. CO peaks at 28% efficiency, using a 20 at% In alloy, before dropping off as In content increases. Furthermore, the highest reported formate efficiency (62%), in this study, is achieved using an 80 at% indium catalyst at this potential. At -1.1 V (**Figure 4.13d**), hydrogen evolution dominates over all ERC products and therefore is typically undesirable given the higher energy consumption and lower ERC product yield. That being said, syngas can still be produced, at an appropriate ratio for Fischer-Tropsch applications, at -1.1 V using a 80 at% indium alloy. Formate peaks at 32% efficiency, as does CO at 17%, with a 60 at% In catalyst. Overall, a complex tradeoff between CO, formate, and H<sub>2</sub> yields is realized at all potentials and alloy compositions. A synergistic effect between copper and indium is generally observed, as we note lower H<sub>2</sub> efficiencies on the alloys, at all potentials, with respect to either elemental metal.

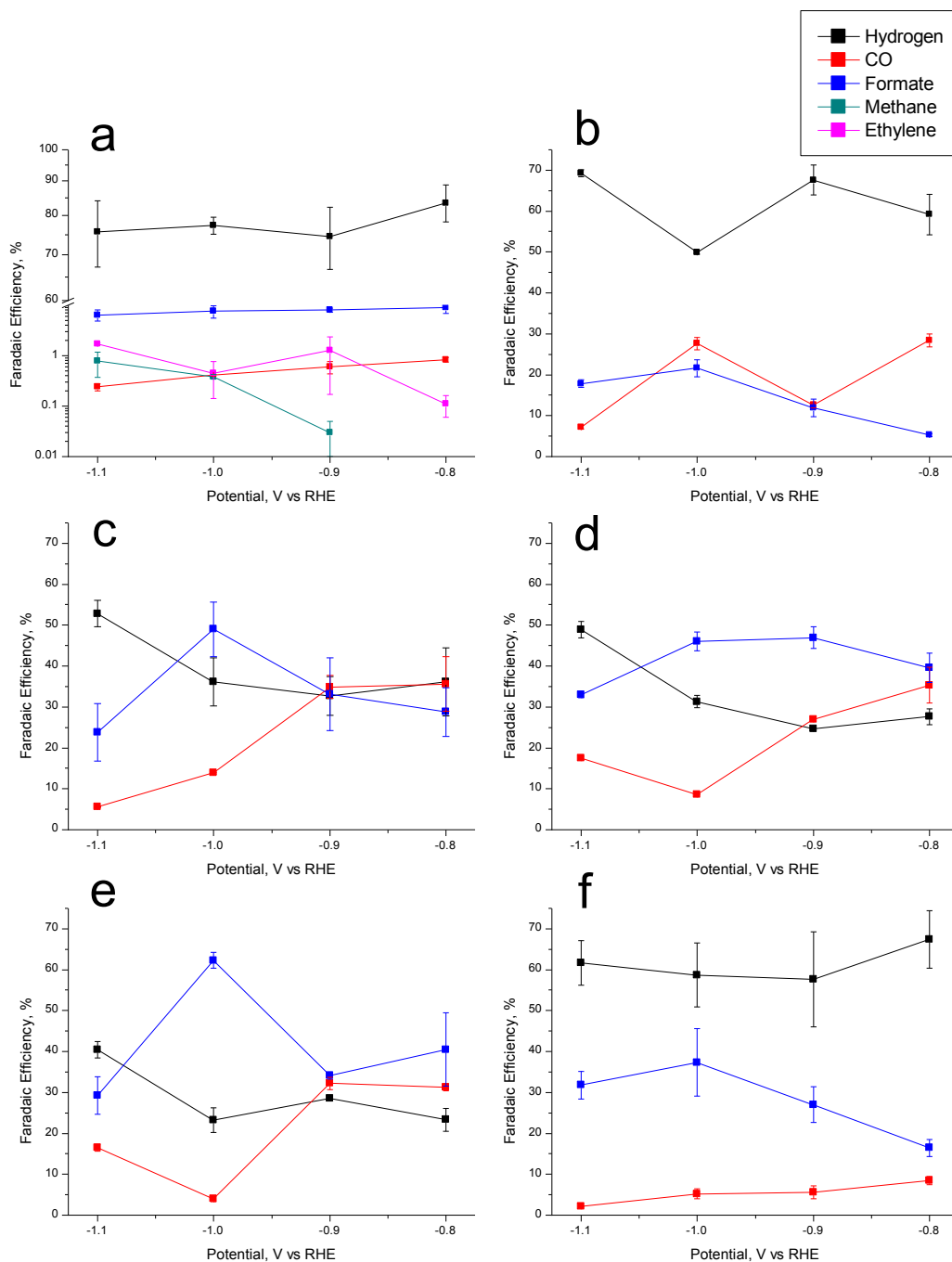


**Figure 4.14:** Product faradaic efficiency as a function of potential at various alloy compositions (a, pure copper; b, 20 at% In; c, 40 at% In; d, 60 at% In; e, 80 at% In; f, pure indium). Note that the data in (a) are presented in semilogarithmic format.

We attempted to determine the actual surface area of our electrodes at a constant cross-sectional thickness by using electrochemical impedance spectroscopy (EIS), according to the method described in ref. [7] (**Figure 3.8**). However, at open circuit potential, the approach to a vertical line expected in the Nyquist plot at low frequency for porous electrodes is never achieved, and the roughness factors determined from the capacitance at low frequency are much lower than expected based on the SEM imaging of cross sections (**Figure 4.4**). We therefore had to resign to use geometric areas and nominal current densities, with the assumption that the surface areas of dendritic Cu and Cu-In would be similar, due to similar morphology, in order to meaningfully compare the available data. Outlined in **Table 4.2** are the calculated double layer capacitances of various catalyst materials and their roughness factors, derived from EIS data and fitting.

Material	Double Layer Capacitance ( $\mu\text{F}/\text{cm}^2$ )	Surface Roughness ( $\text{cm}^2 / \text{cm}^2$ )
Smooth Cu on Si	70.89	1.01 <sup>a</sup>
Dendritic Cu	240.65	3.39
Cu-In (77-23)	1287.53	18.16
Cu-In (61-39)	1451.28	20.47
Cu-In (37-63)	3244.44	45.77
Cu-In (26-74)	3974.73	56.07
Cu-In (16-84)	5521.97	77.89

**Table 4.2:** Calculated  $C_{dl}$  values and associated roughness factors, using smooth Cu on Si as a reference material. <sup>a</sup>Determined using AFM (**Section 3.6e**) and used as a reference for determining surface area of all other films as per **Eqn. 3.5**.

Total and partial nominal current densities for the detected products (**Figure 4.15**) were determined using products yields, current data acquired during the electrolysis of CO<sub>2</sub> on the various electrocatalyst materials, and the geometrical area.

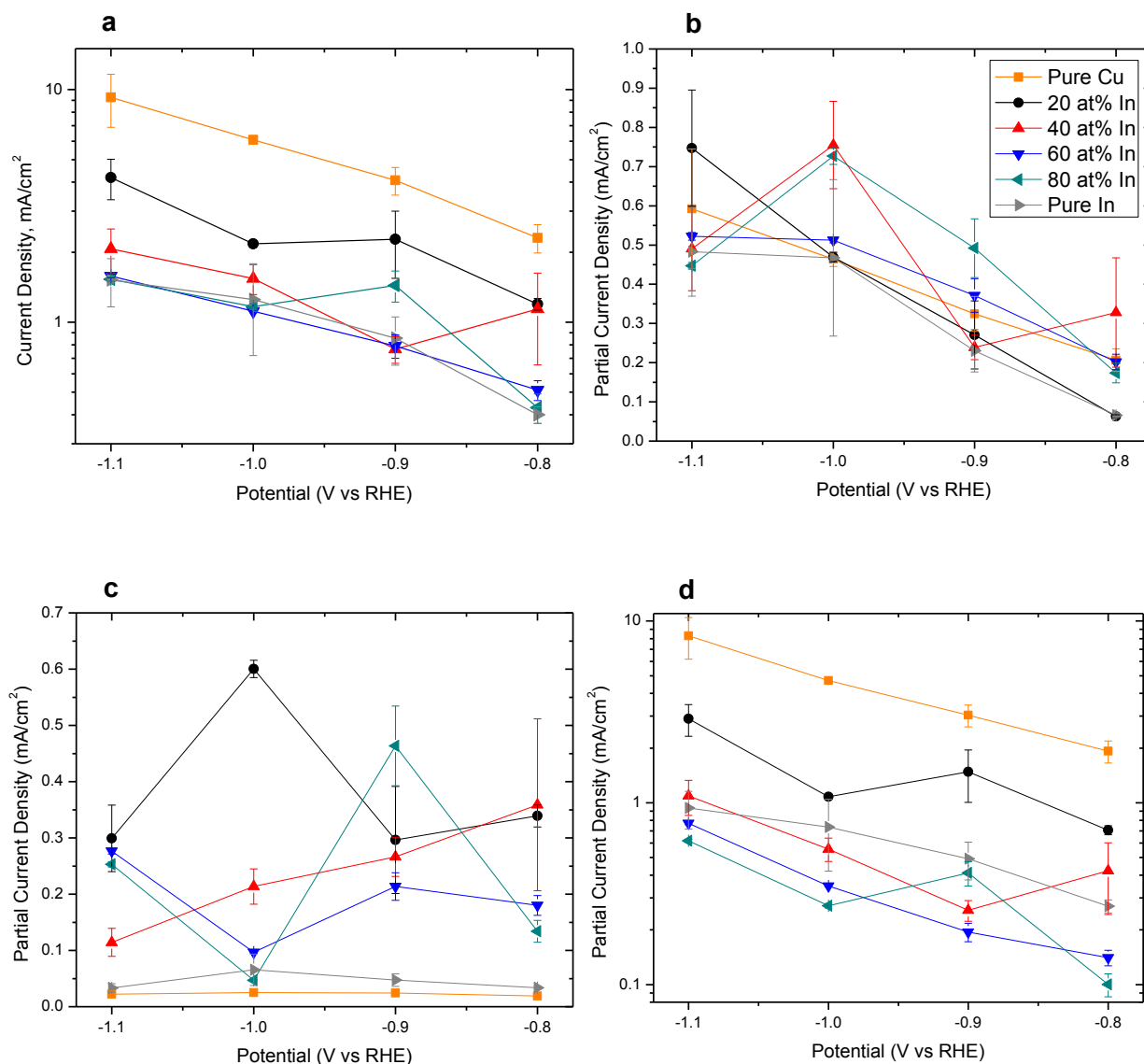


**Figure 4.15:** Total geometric current density (a) and partial currents for (b) formate, (c) CO, and (d) H<sub>2</sub> for Cu, In and the various Cu-In electrocatalysts as a function of applied potential. The current density is normalized to the geometric surface area for each specific material. A logarithmic scale is used in (a) and (d).

Pure Cu shows the largest total current density across all potentials, while for Cu-In alloys the nominal current decreases with increasing In content (**Figure 4.15a**). The trends for pure In generally mirrors that of the 60 and 80 at% In materials.

Alloying of In to Cu resulted in a slower kinetics towards CO<sub>2</sub> reduction, down by almost an order of magnitude. Formate partial current densities (**Figure 4.15b**) are shown to increase as overpotential is increased, even up to -1.1 V vs RHE for some alloys where the efficiency of formate production dropped off only due to the increased HER at this potential. A peak for formate partial current density is seen on several Cu-In alloys at -1.0 V vs RHE, corresponding to the highest Faradaic efficiencies for formate production. CO partial current densities for the various Cu-In alloys (**Figure 4.15c**) show the lowest conversion rates among the various products and some scatter as a function of potential, but they all perform better than pure Cu and In. Thus, a synergistic effect in Cu-In alloys was observed: all alloys produced CO at a higher rate than either pure metallic component. With regard to the H<sub>2</sub> partial current density  $j_{H_2}$  (**Figure 4.15d**), the trends are intuitive –  $j_{H_2}$  is increasing with larger overpotential on all electrocatalysts under study. Interestingly, pure electroplated In generally produces H<sub>2</sub> at a larger rate than the 40, 60, and 80 at% In alloys, showing inhibition of HER upon alloying.

Prior to every ERC an LSV was performed, to ensure reproduction of electrochemical responses for identical catalyst materials. The LSVs shown in **Figure 4.16** corroborate the expected HER suppressing behavior of indium, where addition of indium should result in a lower partial current density for HER and a lower H<sub>2</sub> Faradaic efficiency. As indium content increases, onset of the HER occurs at a higher overpotential.

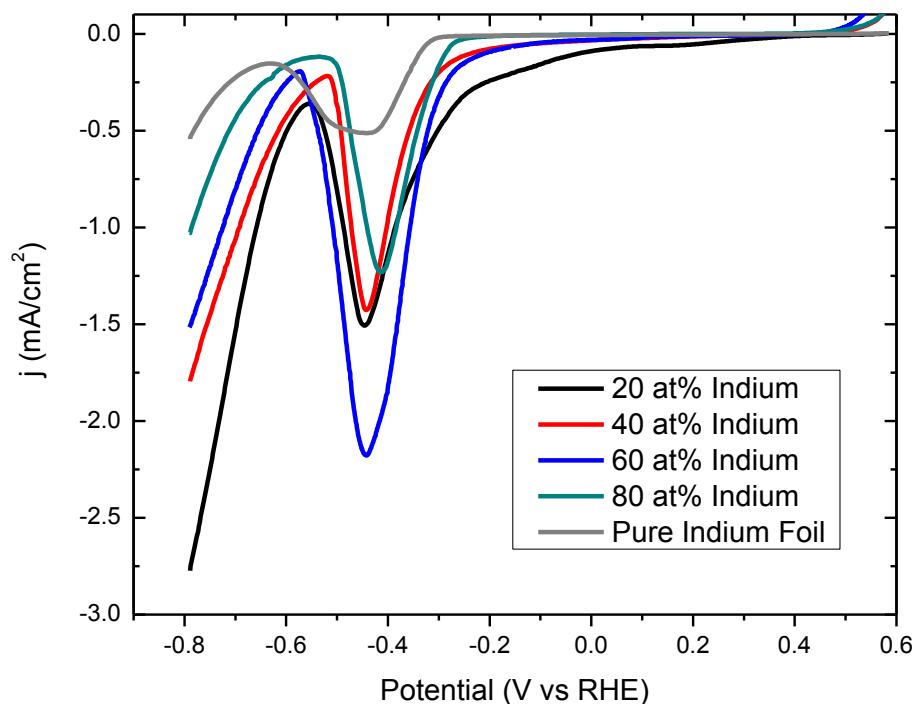


**Figure 4.16:** Linear sweep voltammetry (LSV) comparison of the various Cu-In surfaces and Pure In foil. The current density is shown with respect to the geometric surface area of the catalyst. The LSV was performed from +0.6 V to -0.8 V vs RHE, at a scan rate of 10 mV/s.

Comparisons with other works available in the literature can be made, but they must be only qualitative due to the widely different conditions that have been used. The nominal total current density observed in this work is similar to those of refs. [8-10], but higher than ref. [11], probably due to the more positive potential range used in the latter work. The product distribution is also similar to those reported in those references, with formation of mostly CO and/or formate. The work by Rasul [11] showed a higher CO efficiency (up to 85%), probably due to the slower HER at more positive potentials. High activity facets on Cu nanofoams show a propensity to form formate at higher efficiencies than on their smooth Cu counterparts, with

efficiencies as high as 35% [12]. Thus, alloying Cu with In in a similar dendritic surface morphology, allows for higher formate efficiencies (62%) as demonstrated in this work. Furthermore, nanostructured SnO<sub>2</sub> particles were prepared, by a different method than in ref [13], and a formate efficiency over 80% was achieved [14]. These comparisons lead us to hypothesize that the oxide derived materials reported in refs. [9-11, 13] afford higher efficiencies simply due to nanostructuring and resulting formation of high energy crystal facets with enhanced activity, as exemplified by this work and [8, 12, 14].

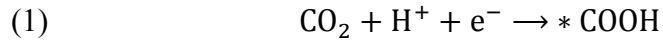
We attempted to find correlations between the structural properties and composition of the electrocatalyst vs. product distribution. We noted a rough relationship between the extent of formate production and the intensity of the high order reflections (400), (711), and (311) for the Cu<sub>9</sub>In<sub>4</sub> and Cu<sub>11</sub>In<sub>9</sub> phases. In contrast, as In content decreased the (111) Cu-In alloy reflection became stronger, correlating to a dominance of CO in the product stream, at potentials below -1.1 V. In addition, selectivity to formate was seen to increase with grain size; this may suggest that defects such as steps and grain boundaries may not be the active sites, but it should be noted that twins may not be detected by XRD but may still be active sites for the reactions of interest. No correlation was however found between the phase constitution and the product distribution, suggesting that no definite conclusion can be inferred about microstructural correlations from the available data.

On the other hand, the observed product distribution can be more directly explained on the basis of surface composition. The Cu-In alloy will tend to be enriched in Indium at the surface due to the larger affinity to -OH; this enrichment however is difficult to quantify due to the complex surface morphology. An overview of the literature shows that CO exhibits a strong adsorption strength at Cu ( $\Delta H_{\text{ads}} \sim -0.7$  eV/at), when CO adsorbs on (100) facets through the C



atom [15]. In contrast, very limited (or no) adsorption of CO<sub>2</sub> or CO occurs on In surfaces [16]. More recently, Lim et al [16] calculated by DFT the enthalpy of adsorption  $\Delta H_{\text{ads}}$  of COOH and CO on Cu and In (see Fig. 3 in [17]):  $\Delta H_{\text{ads}}$  of COOH on Cu was calculated to be -1.5 eV/at and on CO was -0.7 eV/at; in contrast  $\Delta H_{\text{ads}}$  of COOH on In was  $\sim -1.0$  eV, and on CO was  $\sim 0$ . These data show that the presence of two different elements at the surface, one a d-metal, another a sp-metal, may enable modulation of the relative variation of the strength of adsorption of –COOH and –CO, resulting in a departure from the correlation discussed by Norskov between  $\Delta H_{\text{ads}}$  (COOH) and  $\Delta H_{\text{ads}}$  (CO). This in turn may result in a variation of product distribution vs composition, as experimentally observed.

The pathway for the formation of –COOH (detected as HCOOK in our system) and CO has been described as follows [18]:



In order to form HCOOK the adsorption strength of –COOH must be small so that the product may quickly desorb; at high Cu content the probability to adsorb on a Cu atom would increase and CO tends to be formed according to eq. (2). At high In content on the contrary the CO tends to decrease, as observed. The delocalized p orbital on In has a relatively low (compared with other metallic p block dopants) radical-preparation energy cost with regards to stabilizing the 2p orbital of C in the –COOH intermediate. The cost of stabilizing the covalent  $\sigma$ -bond of the p orbital of In with the 2p of –COOH is also relatively low, which ultimately steers the reaction to COOH and in turn HCOOK, after desorption. Furthermore, CO is formed in smaller quantities because an empty p orbital on In is required, for which the unbound electrons on the C in CO

must bond [17]. A larger amount of energy is thus required to catalyze the  $\text{--COOH} \rightarrow \text{CO}$  step, as shown above. The discussed trends correspond with our product distribution, where generally formate is the preferred product, over CO, as In content increases. The product distribution vs. applied potential on the other hand is more difficult to predict due to the dependence of  $\Delta H_{\text{ads}}$  on potential. Overall, the alloying of In with Cu inhibits HER and hinders the path of  $\text{CO}_2$  reduction reaction to CO (**Figure 3. \_\_\_\_**).

## References:

- [1] Shao, W., & Zangari, G. (2009). Dendritic growth and morphology selection in copper electrodeposition from acidic sulfate solutions containing chlorides. *The Journal of Physical Chemistry C*, 113(23), 10097-10102.
- [2] Shin, H. C., & Liu, M. (2005). Three-Dimensional Porous Copper–Tin Alloy Electrodes for Rechargeable Lithium Batteries. *Advanced Functional Materials*, 15(4), 582-586.
- [3] Shin, H. C., Dong, J., & Liu, M. (2003). Nanoporous structures prepared by an electrochemical deposition process. *Advanced Materials*, 15(19), 1610-1614.
- [4] Subramanian, P. R., & Laughlin, D. E. (1989). The Cu– In (Copper-Indium) system. *Bulletin of Alloy Phase Diagrams*, 10(5), 554-568.
- [5] Liang, D., Unveroglu, B., & Zangari, G. (2014). Electrodeposition of Cu-In Alloys as Precursors of Chalcopyrite Absorber Layers. *Journal of The Electrochemical Society*, 161(12), D613-D619.
- [6] Detweiler, Z. M., White, J. L., Bernasek, S. L., & Bocarsly, A. B. (2014). Anodized indium metal electrodes for enhanced carbon dioxide reduction in aqueous electrolyte. *Langmuir*, 30(25), 7593-7600.
- [7] Rouya, E., Cattarin, S., Reed, M. L., Kelly, R. G., & Zangari, G. (2012). Electrochemical characterization of the surface area of nanoporous gold films. *Journal of the Electrochemical Society*, 159(4), K97-K102.
- [8] Kim, D., Resasco, J., Yu, Y., Asiri, A. M., & Yang, P. (2014). Synergistic geometric and electronic effects for electrochemical reduction of carbon dioxide using gold–copper bimetallic nanoparticles. *Nature communications*, 5.
- [9] Li, C. W., & Kanan, M. W. (2012).  $\text{CO}_2$  reduction at low overpotential on Cu electrodes resulting from the reduction of thick  $\text{Cu}_2\text{O}$  films. *Journal of the American Chemical Society*, 134(17), 7231-7234.
- [10] Chen, Y., Li, C. W., & Kanan, M. W. (2012). Aqueous  $\text{CO}_2$  reduction at very low overpotential on oxide-derived Au nanoparticles. *Journal of the American Chemical Society*, 134(49), 19969-19972.
- [11] Rasul, S., Anjum, D. H., Jedidi, A., Minenkov, Y., Cavallo, L., & Takanabe, K. (2015). A Highly Selective Copper–Indium Bimetallic Electrocatalyst for the Electrochemical Reduction of Aqueous  $\text{CO}_2$  to CO. *Angewandte Chemie*, 127(7), 2174-2178.

- [12] Sen, S., Liu, D., & Palmore, G. T. R. (2014). Electrochemical reduction of CO<sub>2</sub> at copper nanofoams. *ACS Catalysis*, 4(9), 3091-3095.
- [13] Chen, Y., & Kanan, M. W. (2012). Tin oxide dependence of the CO<sub>2</sub> reduction efficiency on tin electrodes and enhanced activity for tin/tin oxide thin-film catalysts. *Journal of the American Chemical Society*, 134(4), 1986-1989.
- [14] Zhang, S., Kang, P., & Meyer, T. J. (2014). Nanostructured tin catalysts for selective electrochemical reduction of carbon dioxide to formate. *Journal of the American Chemical Society*, 136(5), 1734-1737
- [15] Föhlisch, A., Nyberg, M., Bennich, P., Triguero, L., Hasselström, J., Karis, O., ... & Nilsson, A. (2000). The bonding of CO to metal surfaces. *The Journal of Chemical Physics*, 112(4), 1946-1958.
- [16] Rossnagel, S. M., Dylla, H. F., & Cohen, S. A. (1979). AES study of the adsorption of O<sub>2</sub>, CO, CO<sub>2</sub>, and H<sub>2</sub>O on indium. *Journal of Vacuum Science & Technology*, 16(2), 558-561.
- [17] Lim, H. K., Shin, H., Goddard III, W. A., Hwang, Y. J., Min, B. K., & Kim, H. (2014). Embedding covalency into metal catalysts for efficient electrochemical conversion of CO<sub>2</sub>. *Journal of the American Chemical Society*, 136(32), 11355-11361.
- [18] Peterson, A. A., Abild-Pedersen, F., Studt, F., Rossmeisl, J., & Nørskov, J. K. (2010). How copper catalyzes the electroreduction of carbon dioxide into hydrocarbon fuels. *Energy & Environmental Science*, 3(9), 1311-1315.

## Chapter 5: Electrochemical Reduction of CO<sub>2</sub> – The Copper-Bismuth System

In this chapter, we demonstrate the capability of copper-bismuth electrocatalysts to selectively and efficiently convert CO<sub>2</sub> to formate at high rates. The crystallography and morphology of these materials is explored using various characterization techniques. With respect to product distribution, the catalysts are compared with their pure metallic components. Furthermore, their catalytic performance is tested at various sets of conditions based on potential and composition of the catalyst. Possible reaction mechanisms, relating to the adsorption strengths of CO<sub>2</sub> and a key intermediate, \*COOH, are discussed with respect to these Cu-Bi catalyst materials. A majority of this chapter is reproduced from published (or soon to be published) work by the author.

### 5.1) Structure and Morphology of Catalyst Materials:

Electrodeposition of Cu-Bi films resulted in the formation of dendritic materials; in order to provide meaningful comparisons with the pure metal counterparts, dendritic Cu and Bi were synthesized by tuning electrolyte chemistry and deposition conditions. Cu films showed a regular tree-like morphology with side branches protruding at 60° angles, as expected for the cubic structure of Cu, while Bi showed a 3-D growth with occasional 2-D dendrites, due to the hexagonal structure of Bi (**Figure 5.1**) [1].

The differences between the two dendritic morphologies are linked to the inherent crystal structure and symmetry of FCC Cu versus hexagonal Bi. A mechanism, outlined by Shao et al.,

discusses the deposition of Cu dendrites by introducing anisotropy through a rate-determining CuCl intermediate [2]. The addition of chloride ions, in a Cu plating solution, introduces anisotropy during growth. However, Bi naturally exhibits anisotropy due to its hexagonal crystal structure [3]; in particular, the Bi  $\langle 012 \rangle$  direction has been shown to be the most favorable path for growth, very different from the  $\langle 110 \rangle$  growth in Cu [2, 4]. The differing growth mechanisms and resulting morphologies, of Cu and Bi, produced atomistically distinctive surfaces for the electrocatalysis of CO<sub>2</sub>.

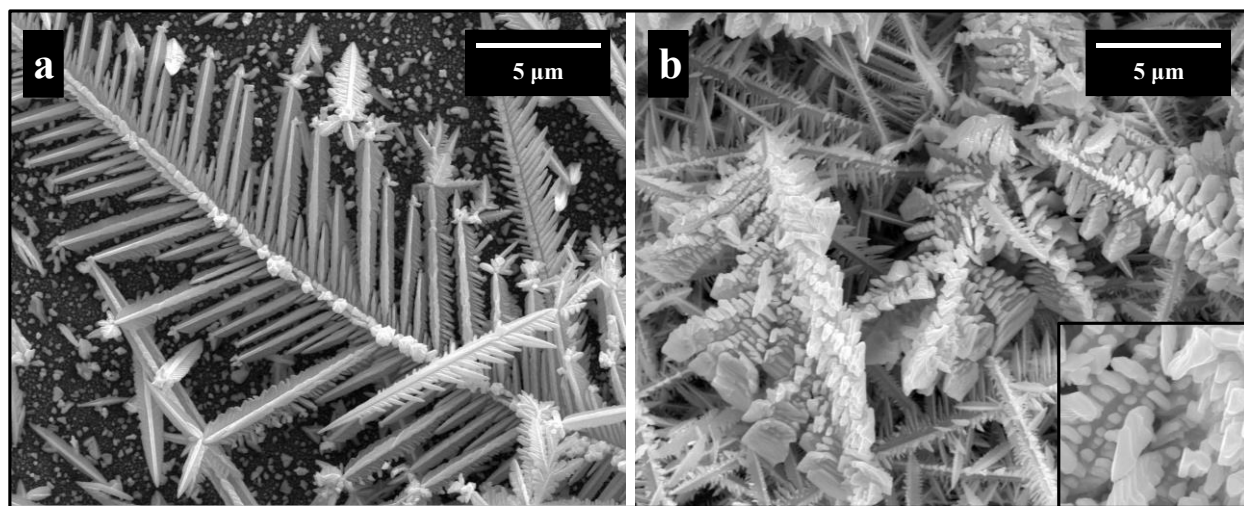


**Figure 5.1:** SEM images of (a) dendritic Cu and (b) dendritic Bi. The zoomed-in inset in (b) reveals a highly complex and faceted surface structure on dendritic Bi.

The film composition (at% Bi) vs. [Bi<sup>3+</sup>] concentration is plotted in **Figure 5.2**. Control of the alloy composition via the metal ion concentration was preferred to the applied potential since the standard potentials of Cu<sup>2+</sup> (+0.34 V) and Bi<sup>3+</sup> (+0.31 V) are very close and the Tafel

slopes are also similar, resulting in an approximately constant composition while varying the potential [5].

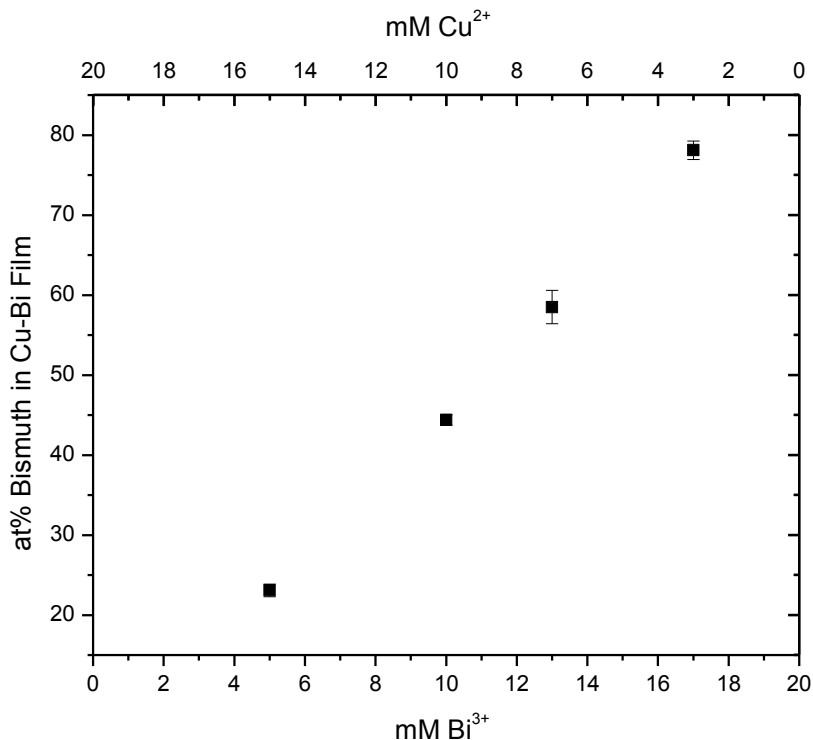


**Figure 5.2:** The composition dependence (at% Bi) of dendritic Cu-Bi films on [Bi<sup>3+</sup>] in the electroplating solution. Total metallic concentration remained constant at 20 mM. Error bars represent standard deviation of EDS confirmed compositions.

The large applied overpotential during electrodeposition caused growth instability on the surface, in turn forming the observed Cu-Bi dendritic constructions. The same deposition potential was used for all solutions (-1.45 V vs MSE), resulting in similar surface morphologies across the entire composition range of Cu-Bi films. **Figure 5.3** reveals the dendritic structure of the explored Cu-Bi films.

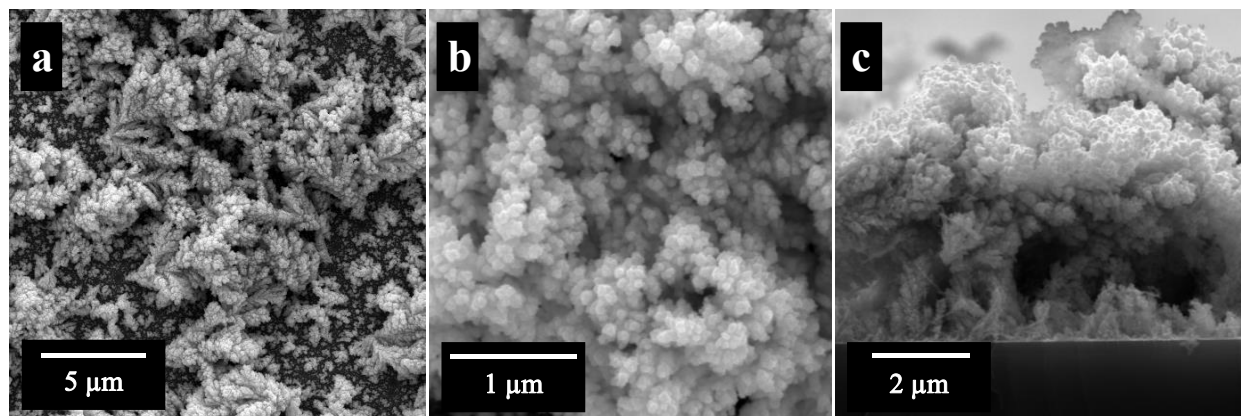


**Figure 5.3:** SEM images of dendritic copper-bismuth (23 at% Bi) films used as electrocatalysts for the ERC. A view of the macroscopic landscape (a), surface features (b), and cross section (c) are shown.

SEM images in **Figure 5.3 (a)** show dense dendritic architectures, with branches of size  $\sim 100$  nm. **Figure 5.3 (b)** shows small features and facets on the surface of these dendrites, again measuring 100 nm or less. The result of these nano-sized features is a high surface area material advantageous for catalysis applications. The cross sectional image, in **Figure 5.3 (c)**, shows a forest-like topography with dense structures. A base continuous layer with thickness of  $\sim 120$  nm was present at the substrate interface. The overall film thickness of these materials varied from 2.5 to 7  $\mu\text{m}$ , with an average thickness of 3.7  $\mu\text{m}$ .

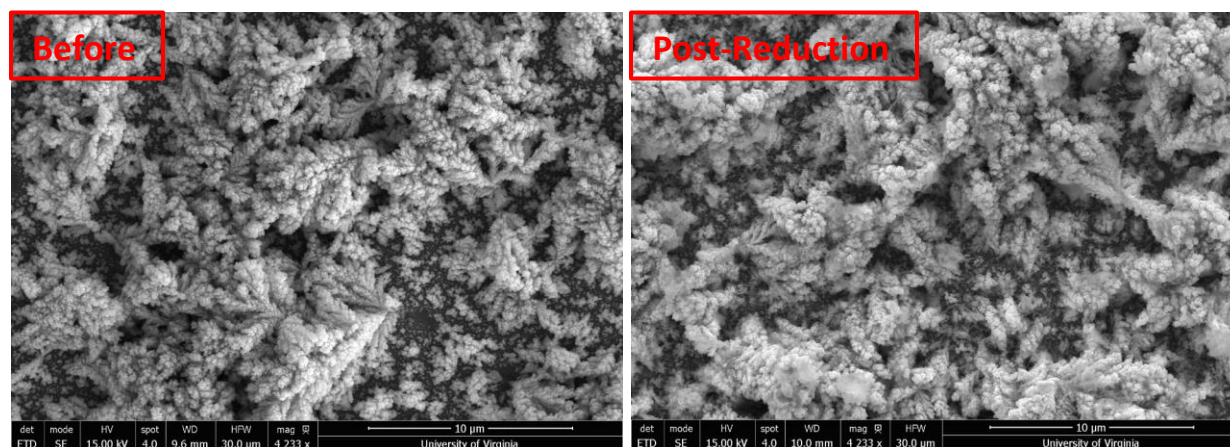
The mechanical and chemical durability of copper-bismuth electrocatalysts was explored with respect to visual surface morphology as well as composition, using SEM and EDS, respectively. Measurements and images were taken before and after ERC experiments in order to evaluate the effect of electrolysis on our various catalyst materials. **Figure 5.4** shows the surface

structure of four Cu-Bi alloys before and after ERC experiments. The copper rich films hold up very well, while the two bismuth rich films show significant changes. These changes are made evident by a significant contrast of the large dendritic constructions. Interestingly, very little compositional changes are seen in these bismuth rich films, let alone any of the films, despite these changes in morphology. Overall, the integrity of these catalysts is maintained during CO<sub>2</sub> reductions but much longer lifetime analyses will need to be performed prior to use in industrial or large scale applications.

Sample	at% Bi Before	at% Bi After
1	23	25
2	44	48
3	60	60
4	78	79

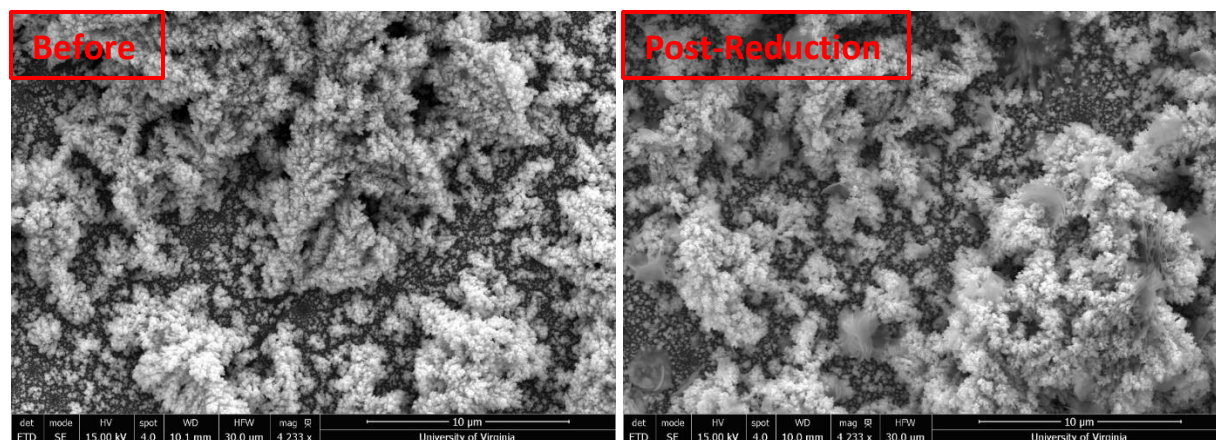
**Table 5.1:** EDS analysis on bismuth content before and after ERC experiments on \_\_ samples of different compositions.

Sample 1:

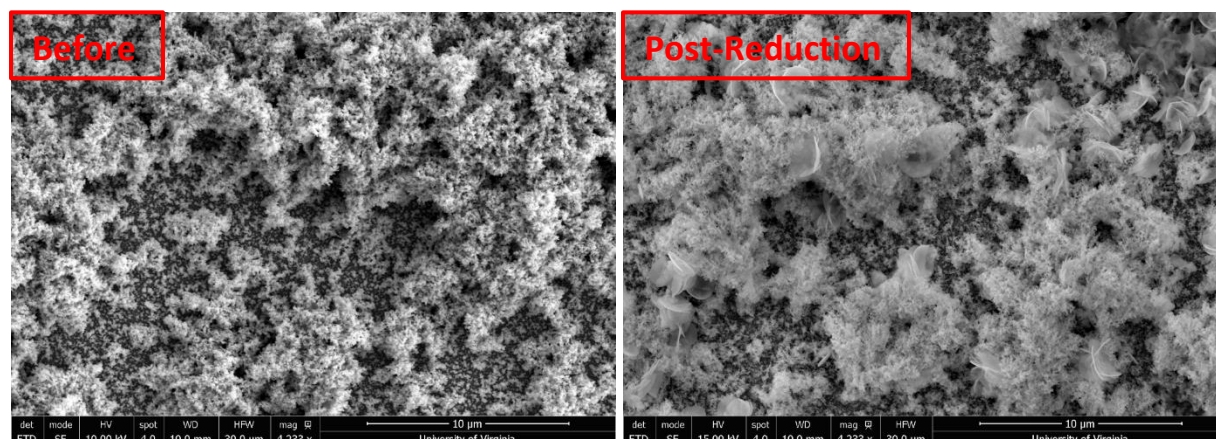




Sample 2:



Sample 3:



Sample 4:

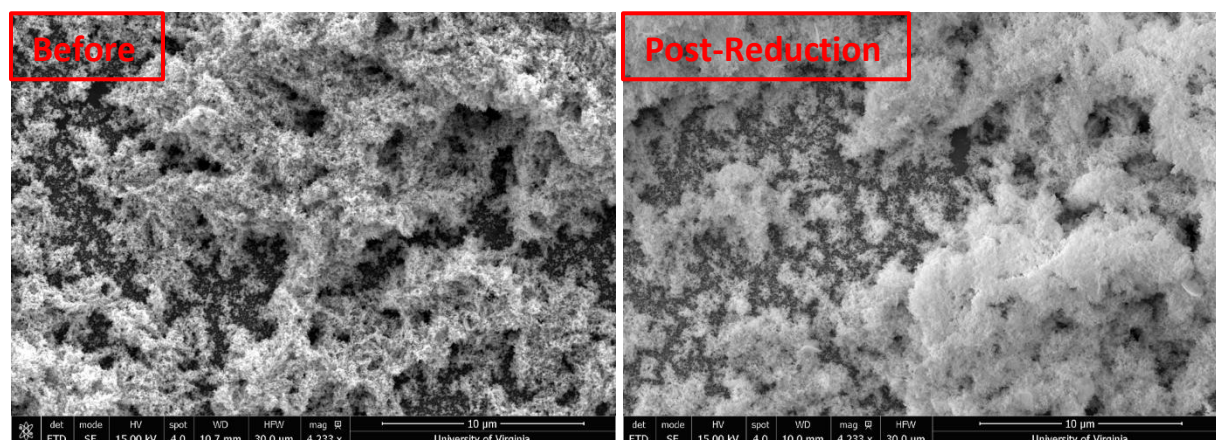


**Figure 5.4:** SEM images showing surface morphology of various Cu-Bi electrocatalysts before and after ERC experiments (see **Table 5.1**).

Grazing incidence XRD patterns of Cu, Bi and Cu-Bi alloys are shown in **Figure 5.5**. Pure Cu films show (111) and (200) reflections, while the Bi XRD pattern evidences a variety of Bi peaks, suggesting a polycrystalline microstructure. The low symmetry of bismuth's hexagonal crystal structure results in a large number of elemental Bi reflections. In the 20 at% Bi films, the only prominent Bi reflection is the (122) atomic plane.

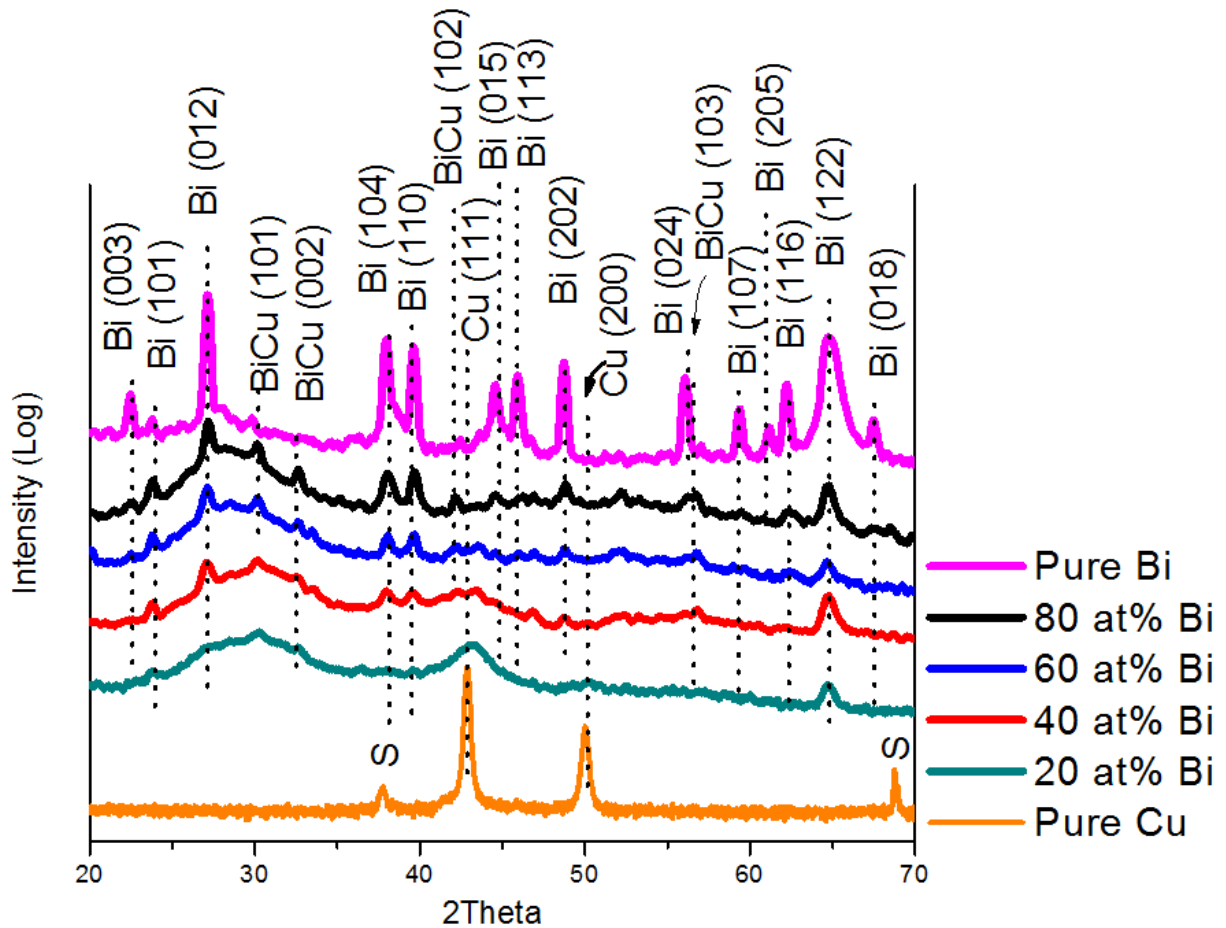


**Figure 5.5:** Grazing incidence x-ray diffraction (GI-XRD) patterns for electrodeposited Cu, Bi, and Cu-Bi films. All films shown have a comparable dendritic surface morphology. Dotted lines and arrows align with the various phases discovered in the films. Peaks labeled S, indicate reflections associated with the substrate.

In these films, the Cu (200) is barely above the baseline and immediately disappears with increasing Bi content. As the composition increases to 40 at% Bi, sharp Bi peaks emerge corresponding to the (101), (104), and (110) atomic planes. In the Bi rich films (60 and 80 at%) several more elemental Bi reflections materialize, although most of them are very small. Pure dendritic Bi shows the same elemental Bi peaks, as these Bi rich films, but are distinguishably sharper and more prominent.

Four peaks on the XRD pattern are assigned to a metastable hexagonal BiCu phase [6, 7]. Despite hexagonal BiCu typically being a metastable phase requiring heat treatment above 300 °C and pressures above 40 kbar [8], this phase was formed via electrodeposition at room temperature and pressure. The enthalpy of formation of several ordered metastable Cu-Bi compounds were found to be highly positive and thus unfavorable to form three-dimensional compounds [9].

With increasing Bi fraction the Cu-Bi alloys show initially two main wide peaks, centered around 30 and 43.5 degrees (2 theta); the first corresponds to a d spacing of about 0.3 nm, close but not identical to the d spacing of the (012) planes, or closer to the d spacing between (101) BiCu planes; the second instead corresponds to the main reflection of Cu, widened by the nanostructuring of the resulting films. At higher Bi fraction these reflections remain, but over the background the crystalline peaks of Bi and the intermetallic BiCu increase, showing an increased crystallinity. This broad peak has been experimentally seen in amorphous Bi as well as in an amorphous Bi-SiO<sub>2</sub> composite, where the center of this wide peak shifts with increasing SiO<sub>2</sub> content [10].

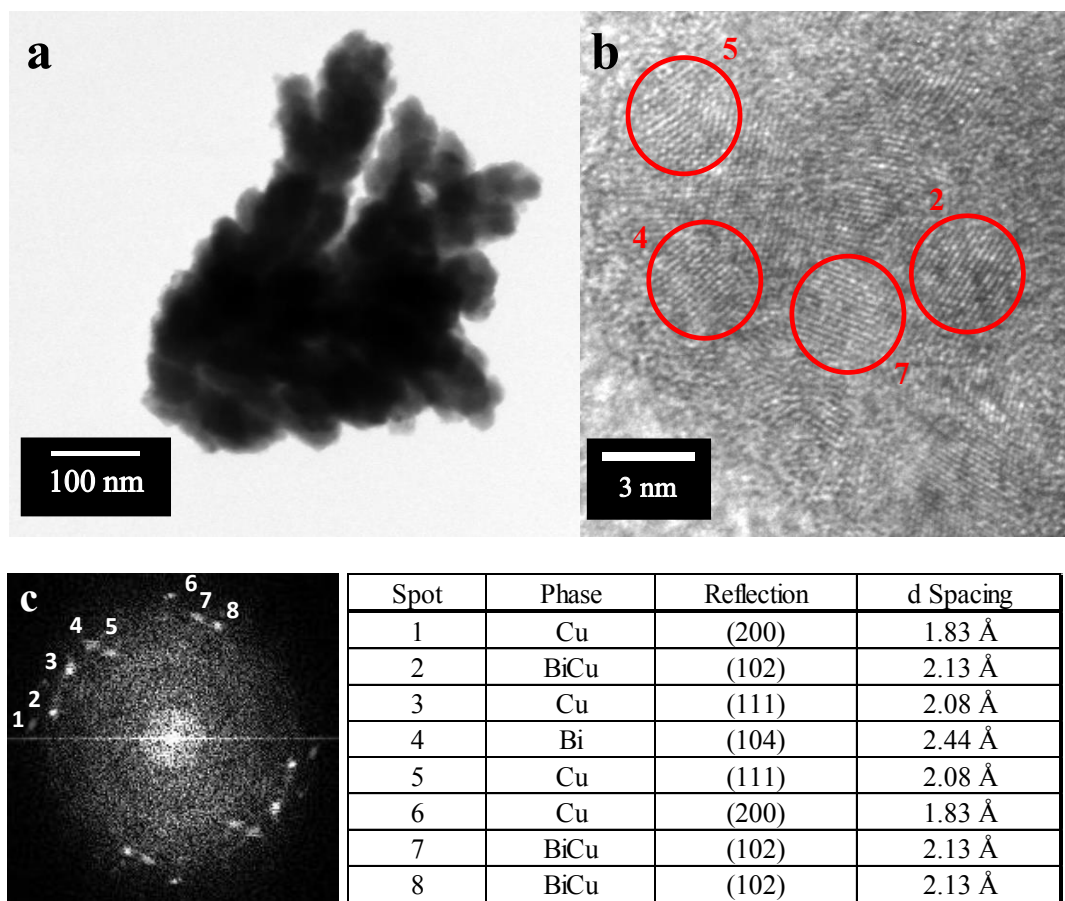


**Figure 5.6:** HR-TEM images of a 20 at% Bi alloy catalyst: (a) macroscopic view of a dendrite network, (b) zoomed-in image of a dendrite tip revealing nanocrystalline grains, (c) resolved FFT image and table of associated phases, reflections, and d spacings. Spots of particular grains listed in (c) are circled in red in (b).

HR-TEM was performed on selected Cu-Bi films in order to better determine the crystal structure, the grain size and morphology, as well as the distribution of the various phases at or near the dendritic surface. **Figure 5.6** shows both a macroscopic view of a dendrite tip as well as various grains of elemental Cu, Bi, and metastable BiCu. Small grains about 4 to 10 nm in diameter are revealed, and a very thin (~2 nm) amorphous layer can also be discerned at the

dendrite surface. The small size (few nm) of the grains, as revealed by the various phases observed, results in a high density of grain boundaries, and contributes to the overall nanocrystalline nature of these materials. Discussion of crystallinity and structure will be examined further, in coming sections.

## **5.2) Electrolysis of CO<sub>2</sub> – Product Distribution and Conversion Rates:**

**Figure 5.7** shows the product distribution observed for pure dendritic Cu and Bi surfaces with respect to applied reduction potential. Dendritic Cu yielded a large majority of H<sub>2</sub>, above 70% efficiency, at all potentials. Formate is steadily produced at ~9% efficiency while CO, methane, and ethylene remain minor products at or below an efficiency of ~2%. On the other end of the composition range, formate and H<sub>2</sub> are the main two products on dendritic Bi, with ~1% CO as the minor product. A maximum, 62% efficiency, for producing formate is achieved at -0.9 V vs RHE while other potentials maintain average efficiencies above 45%. Other than the peak formate production at -0.9 V, the overall trends remain relatively constant.



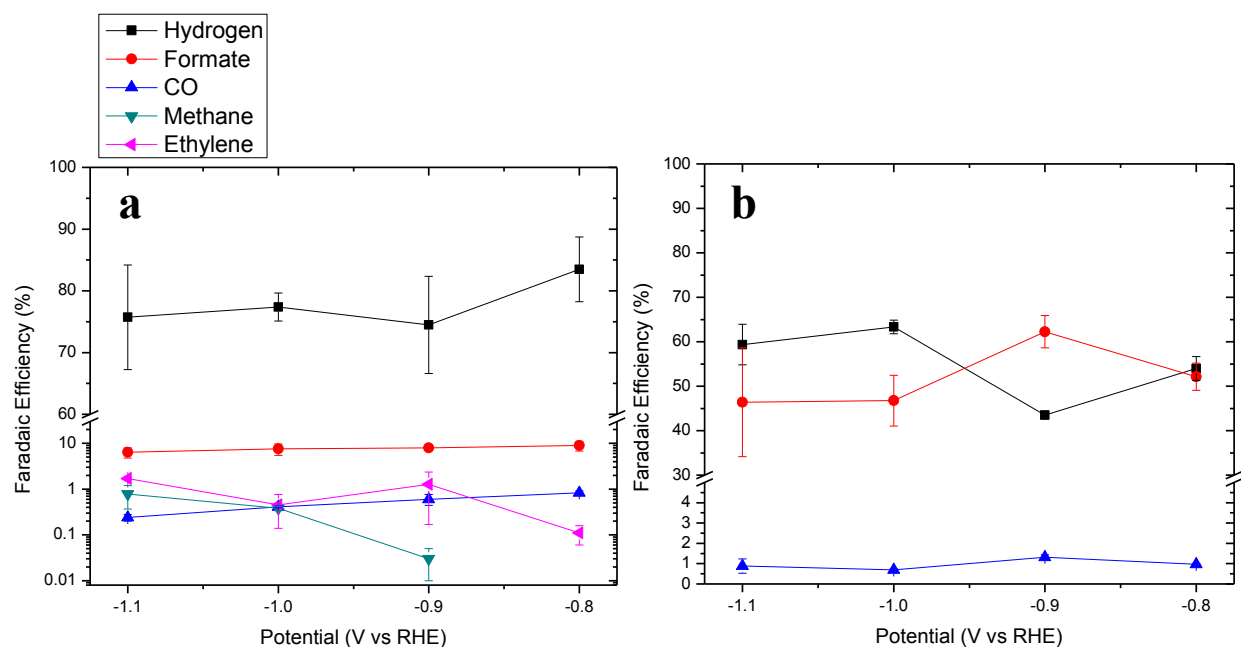


**Figure 5.7:** Product distribution (Faradaic efficiency) as a function of potential on dendritic Cu (a) and dendritic Bi (b). A logarithmic scale is used in (a) to show minor and trace products.

The product distribution as a function of potential for the various Cu-Bi electrocatalysts is shown in **Figure 5.8**. The films with the lowest Bi content (20 at%, **Figure 5.8a**) show high formate production, above 85% efficiency, at the most positive explored potential of -0.8 V vs RHE. As overpotential increases, formate efficiency decreases while HER increases (**Figure 5.8a**). At -0.9 V, using a 40 at% Bi catalyst (**Figure 5.8b**) formate reaches its peak efficiency at ~90%. Formate and H<sub>2</sub> exhibit opposite trends with this composition, where formate decreases when H<sub>2</sub> formation increases. Furthermore, we see an increase in formate efficiency from -1 to -1.1 V, followed by a sharp decrease as the potential is pushed to -1.2 V (not shown).

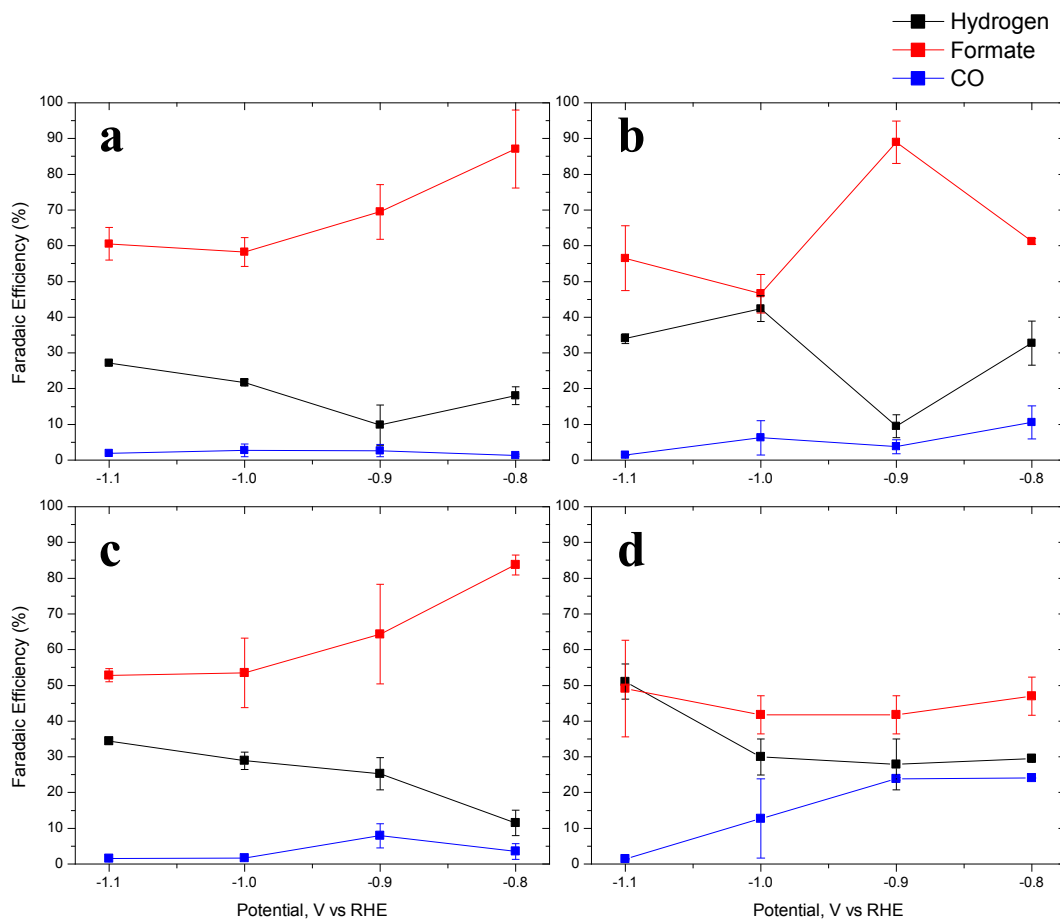


**Figure 5.8:** Product Faradaic efficiency vs. applied potential (V vs RHE) for compositionally varying Cu-Bi alloys (**a**, 20 at% Bi; **b**, 40 at% Bi; **c**, 60 at% Bi; **d**, 80 at% Bi).

Interestingly the 60 at% Bi films show almost identical behavior to that of the 20 at% Bi films, where formate production is maximized at -0.8 V, with approximately 85% efficiency.

Additionally, a small peak in CO production is witnessed at -0.9 V, where CO efficiency reaches ~8%. The 80 at% Cu-Bi films show the lowest formate efficiencies, hovering between 45 and 50% independent of reduction potential. This composition also reveals the greatest propensity to form CO at lower potentials, where ~25% efficiencies are achieved.

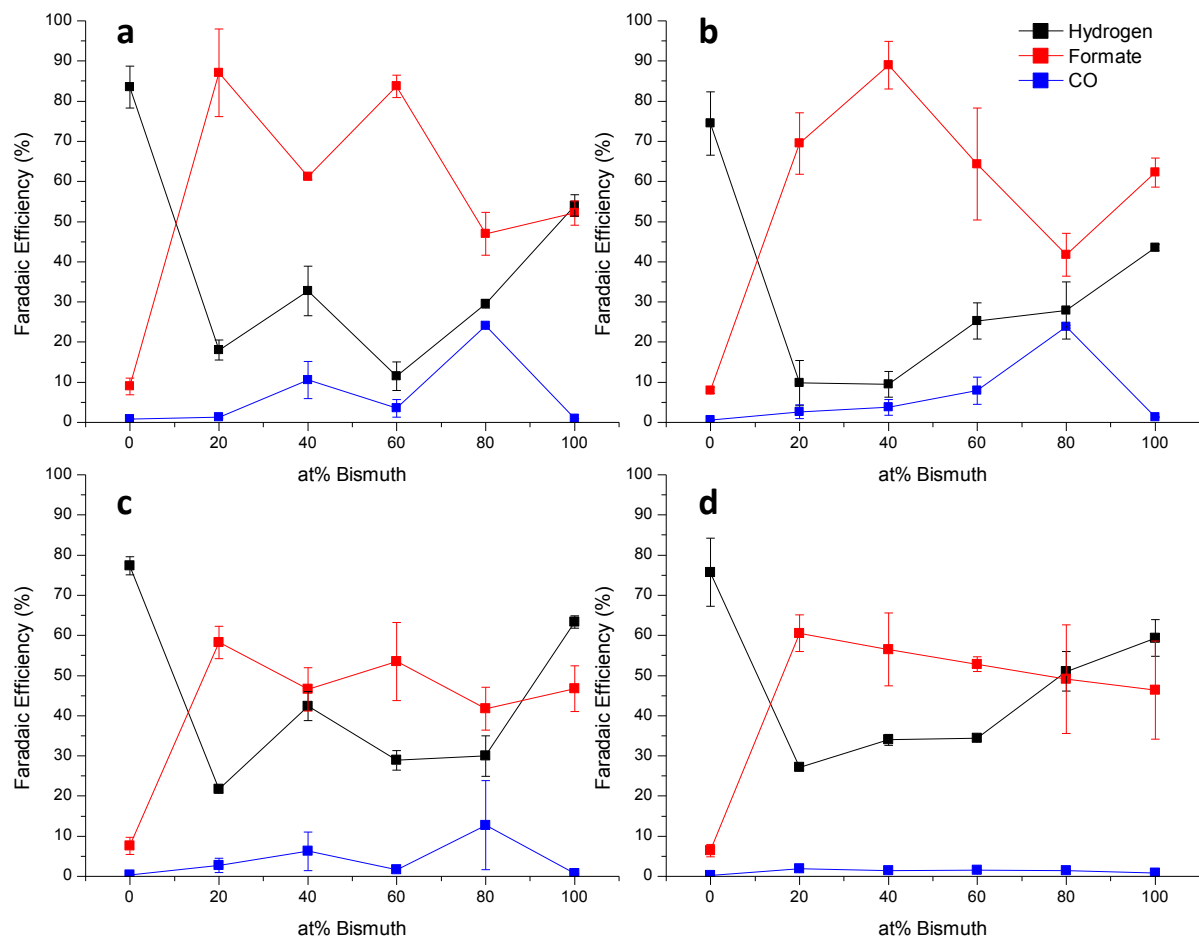


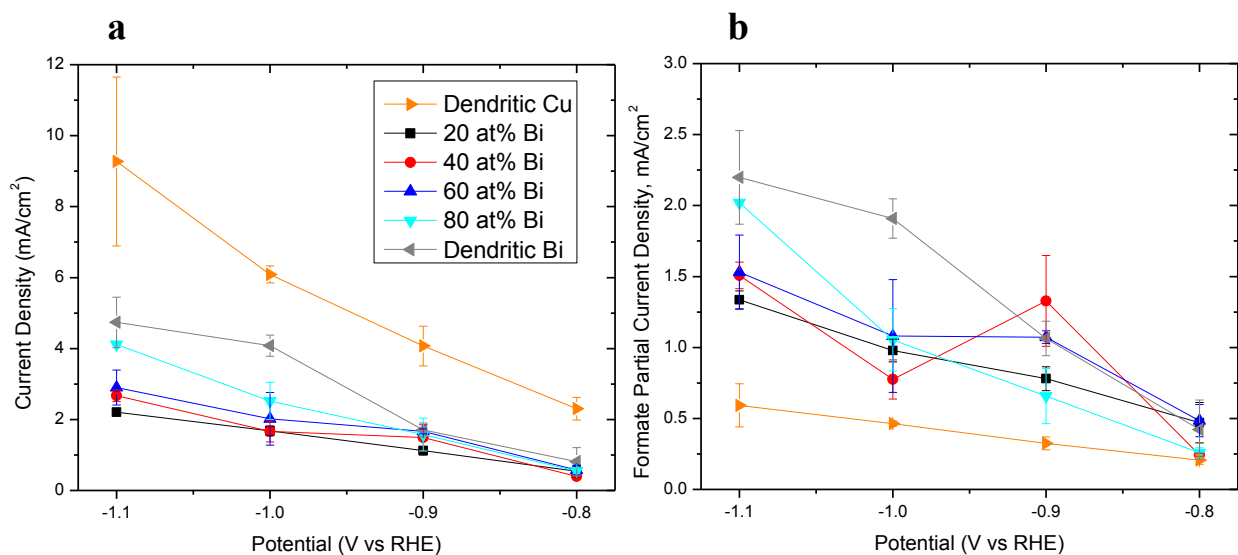
**Figure 5.9:** Product distribution (Faradaic efficiency) as a function of composition. The CO<sub>2</sub> reductions were performed at (a) -0.8 V vs RHE; (b) -0.9 V vs RHE; (c) -1.0 V vs RHE; (d) -1.1 V vs RHE.

Overall, a balance is noted between HER and formate production on Cu-Bi electrocatalysts, while CO remains the minor product (except in the case of the 80 at% Bi material). The lowest reduction potentials (-0.8 and -0.9 V vs RHE) show the greatest efficiency towards formate production. **Figure 5.9** shows the product distribution as a function of Bi content at the four reduction potentials. A synergistic effect between Cu and Bi is observed, as formate is produced at significantly larger efficiencies than on either pure metal. Correspondingly, HER formation is reduced, reaching a minimum efficiency below 12%.



The total and partial current densities were calculated from the measured product distribution, the current data recorded during every ERC experiment, and the geometric area of the electrocatalysts. The geometric area was used, due to the difficulty to measure accurately the true surface area. This choice is supported by the observation of similar thickness and morphology across the entire composition range of Cu-Bi.

The total and partial current densities of all three major products ( $H_2$ , formate,  $CO$ ) are shown in **Figure 5.10**. Dendritic Cu showed the highest overall current density followed by dendritic Bi and the Cu-Bi films, in order from highest to lowest Bi content. The addition of just 20 at% Bi to a Cu matrix, decreases the current density by a factor of 5, despite a larger surface area and more complex surface morphology. These films show great catalytic activity for forming formate as partial current densities (**Figure 5.10b**) increase steadily with increasing overpotential.



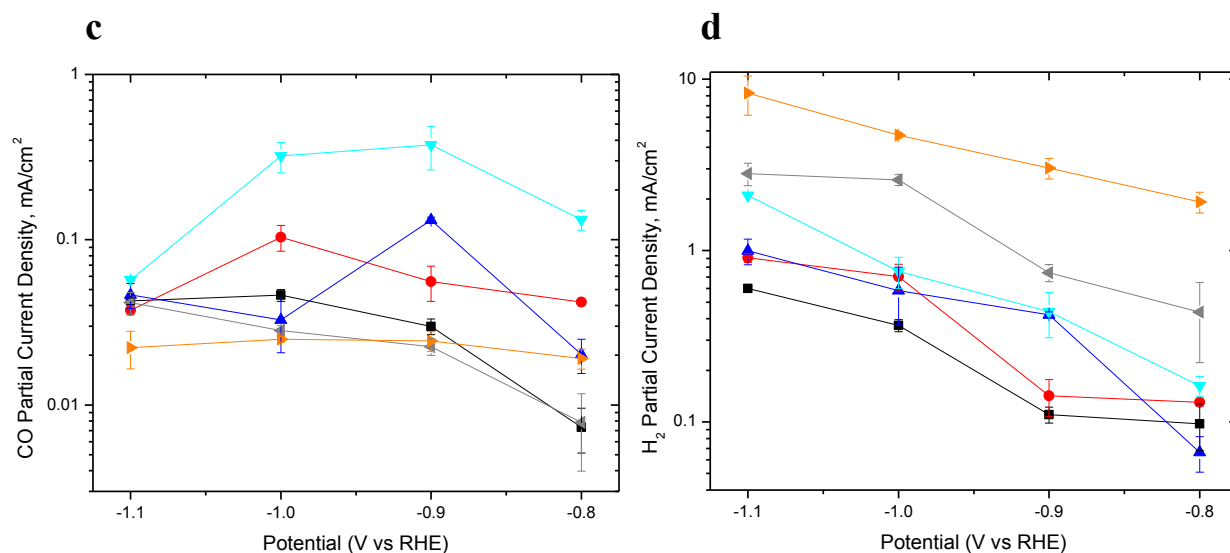


**Figure 5.10:** The geometric current density (a) and partial current densities for (b) formate, (c) CO, and (d) H<sub>2</sub> for dendritic Cu, Bi, and Cu-Bi films. Current density is plotted with respect to applied potential. A logarithmic scale is used in (c) and (d) for better visibility of trends.

Dendritic Bi shows the largest partial current densities for formate production at -1 and -1.1 V, while remaining very significant at more positive potentials. 40 at% Bi films show a peak at -0.9 V due to the extraordinarily high selectivity and efficiency for formate (~90%), at that potential (FE **Figure 5.10b**). CO partial current densities (**Figure 5.10c**) are approximately constant with respect to applied potential. Overall, the CO partial current densities are low compared to formate, except in the case of the 80 at% Bi films where CO efficiencies are the highest. Dendritic Cu and Bi show the highest catalytic activity for HER (**Figure 5.10d**), while the Cu-Bi electrocatalysts show significantly lower current densities. A synergistic effect of Cu and Bi suppresses the unwanted HER in favor of substantial formate production.

We sought out connections between composition and crystallography of the various electrocatalyst materials with respect to product distribution and reaction kinetics. Small amounts of Bi, in the studied Cu-Bi films, allow for greater formate production than on either pure metal. The nanocrystalline structure portrayed by GI-XRD and imaged with TEM, is probably related to the unusual formate efficiencies (>80%) that have been achieved, herein. The nanostructuring of Bi, by Zhang et al., shows enhancement of catalytic activity and selectivity towards formate [11]. Identical Faradaic efficiencies (~90%) for formate production were found on a nanostructured Bi sheet, with particles as small as 10 nm. XRD, however, revealed that these Bi catalysts are far from nanocrystalline, as also observed in this work, despite the similar product distribution.

Despite Bi being known as a predominantly formate-producing catalyst [12], experimental evidence suggests certain atomic planes of Bi favor the formation of CO. As Bi content increases to 80 at%, we see a noticeable increase in CO production. This increase in Bi corresponds to an increase in XRD peak intensity for the Bi (104), Bi (110), Bi (202), and Bi (116) reflections. Also, the Bi (012) peak is sharper at this composition, shedding light on what appears to be a higher degree of crystallinity. Recently, it was shown that Bi supported on a carbon substrate produced CO at high efficiencies (>80%) and current densities ( $j_{\text{CO}} = 10 \text{ mA/cm}^2$ ) but in an ionic liquid environment [13]. Similar work, from the same researchers, show similar CO efficiencies (~75%) on an amorphous Bi catalyst material. The amorphous nature of the material was confirmed by XRD, with the appearance of a broad peak around  $2\theta \sim 28^\circ$  - identical to our studied films [14].

Investigations on other sp-metals, In and Sn, show that the major product can be formate with an aqueous electrolyte and CO with a non-aqueous electrolyte [15]. Sn nanoparticles show optimized formate efficiency (>80%) when the size is adjusted to around ~5 nm – quantitatively

similar to the size of Bi (104) and Cu (111) grains (**Figure 5.6**) [16]. Thus, the product distribution on sp-metal catalysts, potentially including Bi, appears highly dependent on the catalyst fabrication process and/or the electrolyte used in CO<sub>2</sub> reduction investigations.

Studies of CO<sub>2</sub> adsorption on Bi, outside of the electrochemistry realm, reveal very weak chemisorption, or more appropriately physisorption to the surface [17, 18]. Despite this, the activity for the hydrogen evolution reaction (HER) is very low on Bi [19], which allows for the formation of small molecules to successfully compete. DFT calculations on alloys of a d-metal (Cu) with a sp-metal show the possibility to steer product distribution towards formate (or CO) due to the modification of the adsorption energies of –COOH and –CO intermediates. Bi, unfortunately isn't explored in this context, but the revealed trends (by row and column in the periodic table) indicate Bi would have the lowest energy requirement for the radical preparation and covalent bond stabilization steps [20]. The –COOH intermediate is easily formed and requires only one proton-coupled electron transfer (PCET) step. Furthermore, it has been shown that Bi adsorbs –COOH very weakly, and thus may be the driving force for the likely desorption as formate into the product stream [21, 22].

Overall, the preparation of bimetallic Cu-Bi electrocatalysts has ultimately provided increases in the efficiency and selectivity for formate production from the ERC. The amorphous nature and metastable phases on these films potentially provide greater catalytic activity towards CO<sub>2</sub> reduction, although this has been very difficult to confirm. Furthermore, a distinct bifunctional effect of Cu and Bi on the electrocatalysis of CO<sub>2</sub> can be concluded, due to a larger formate output on morphologically similar films of pure Bi and Cu.

## References:

- [1] Wranglen, G. (1960). Dendrites and growth layers in the electrocrystallization of metals. *Electrochimica Acta*, 2(1-3), 130-143.
- [2] Shao, W., & Zangari, G. (2009). Dendritic growth and morphology selection in copper electrodeposition from acidic sulfate solutions containing chlorides. *The Journal of Physical Chemistry C*, 113(23), 10097-10102.
- [3] Jiang, S., Huang, Y. H., Luo, F., Du, N., & Yan, C. H. (2003). Synthesis of bismuth with various morphologies by electrodeposition. *Inorganic Chemistry Communications*, 6(6), 781-785.
- [4] Yang, M. (2011). Fern-shaped bismuth dendrites electrodeposited at hydrogen evolution potentials. *Journal of Materials Chemistry*, 21(9), 3119-3124.
- [5] Brenner, A. (2013). *Electrodeposition of alloys: principles and practice*. Elsevier.
- [6] Predel, B. (2012). Bi-Cu (Bismuth-Copper). In *B-Ba... Cu-Zr* (pp. 101-102). Springer Berlin Heidelberg.
- [7] G. Hägg, G. Funke (1929). *Z. Phys. Chem. (B)*, B6, 272.
- [8] Matthias, B. T., Jayaraman, A., Geballe, T. H., Andres, K., & Corenzwit, E. (1966). Many More Superconducting Bismuth Phases. *Physical Review Letters*, 17(12), 640.
- [9] Siegl, R., Yan, M., & Vitek, V. (1997). Atomic structures of grain boundaries in copper-bismuth alloys: ab initio and empirical modelling. *Modelling and Simulation in Materials Science and Engineering*, 5(2), 105.
- [10] Ponta, O., Mocuta, H., Vasilescu, M., & Simon, S. (2011). Structural characterization of amorphous and nanostructured bismuth silicate xerogels. *Journal of sol-gel science and technology*, 58(2), 530-534.
- [11] Zhang, H., Ma, Y., Quan, F., Huang, J., Jia, F., & Zhang, L. (2014). Selective electro-reduction of CO<sub>2</sub> to formate on nanostructured Bi from reduction of BiOCl nanosheets. *Electrochemistry Communications*, 46, 63-66.
- [12] S. Komatsu, T. Yanagihara, Y. Hiraga, M. Tanaka, and A. Kunugi, *Denki Kagaku* 63(1995) 217.
- [13] Medina-Ramos, J., Pupillo, R. C., Keane, T. P., DiMeglio, J. L., & Rosenthal, J. (2015). Efficient Conversion of CO<sub>2</sub> to CO Using Tin and Other Inexpensive and Easily Prepared Post-Transition Metal Catalysts. *Journal of the American Chemical Society*, 137(15), 5021-5027.
- [14] Medina-Ramos, Jonnathan, John L. DiMeglio, and Joel Rosenthal. "Efficient reduction of CO<sub>2</sub> to CO with high current density using in situ or ex situ prepared Bi-based materials." *Journal of the American Chemical Society* 136.23 (2014): 8361-8367.
- [15] Chaplin, R. P. S., & Wragg, A. A. (2003). Effects of process conditions and electrode material on reaction pathways for carbon dioxide electroreduction with particular reference to formate formation. *Journal of Applied Electrochemistry*, 33(12), 1107-1123.
- [16] Zhang, S., Kang, P., & Meyer, T. J. (2014). Nanostructured tin catalysts for selective electrochemical reduction of carbon dioxide to formate. *Journal of the American Chemical Society*, 136(5), 1734-1737.
- [17] Browne, V. M., Carley, A. F., Copperthwaite, R. G., Davies, P. R., Moser, E. M., & Roberts, M. W. (1991). Activation of carbon dioxide at bismuth, gold and copper surfaces. *Applied surface science*, 47(4), 375-379.
- [18] Freund, H. J., & Roberts, M. W. (1996). Surface chemistry of carbon dioxide. *Surface Science Reports*, 25(8), 225-273.

- [19] Greeley, J., Jaramillo, T. F., Bonde, J., Chorkendorff, I. B., & Nørskov, J. K. (2006). Computational high-throughput screening of electrocatalytic materials for hydrogen evolution. *Nature materials*, 5(11), 909-913.
- [20] Lim, H. K., Shin, H., Goddard III, W. A., Hwang, Y. J., Min, B. K., & Kim, H. (2014). Embedding covalency into metal catalysts for efficient electrochemical conversion of CO<sub>2</sub>. *Journal of the American Chemical Society*, 136(32), 11355-11361.
- [21] Lust, E., Jänes, A., Lust, K., & Ehrlich, J. (1999). Orientation of organic compounds at single-crystal bismuth electrodes. *Electrochimica acta*, 44(26), 4707-4720.
- [22] Lust, E., Janes, A., Lust, K., & Pullerits, R. (1997). Adsorption of organic compounds and hydrophilicity of bismuth, cadmium and antimony electrodes. *Journal of Electroanalytical Chemistry*, 431(2), 183-201.

## Chapter 6: Conclusions and Future Research Prospects:

Parts of the conclusions were reproduced from work published (or soon to be published) by the author.

### Conclusions:

The electrochemical reduction of CO<sub>2</sub> (ERC) was performed on both Cu-In and Cu-Bi electrocatalysts of varying composition within a potential range of -0.8 to -1.1 V vs RHE. These two bimetallic systems were investigated, with respect to composition, in increments of 20 at% of the sp-metal alloying material (In or Bi).

Dendritic Cu-In alloys were obtained by electrodeposition; Cu-rich electrodes mainly consisted of a solid solution, while various intermetallics were formed at higher In content. TEM imaging evidenced the formation of dendrite tips of ~ 50 nm width, exhibiting a variety of surface facets including those with high surface activity. The ERC at Cu-In has been shown to produce formate at high efficiency while simultaneously enabling adjustment of the ratio of syngas components. Specifically, at 40 at% Indium and -1.0 V vs RHE, we achieve high formate production (49% Faradaic Efficiency, FE) as well as an optimal ratio, of 2.6:1 H<sub>2</sub> to CO, in the effluent syngas produced. Furthermore, a maximum of 62% FE for formate is obtained at this potential with an 80 at% indium electrode. The selectivity towards formate synthesis is linked to the indium fraction at the electrode surface. On the other hand, the greatest CO efficiencies are achieved at lower reduction potentials and decrease with higher indium content. The fraction of In (sp metal) and Cu (d metal) at the surface varies the relative adsorption strength of -COOH

and  $-\text{CO}$  intermediates. A weak adsorption of  $-\text{COOH}$  leads to selectivity towards formate production, while a stronger  $-\text{COOH}$  adsorption proceeds to  $\text{CO}$  production. The combined effects from varied potential and catalyst composition change the adsorption trends; ultimately leading to the observed product distribution.

Cu-Bi catalysts were grown via electrodeposition, from several acidic nitrate based solutions. SEM imaging revealed dendritic constructions, with features on the order of 50-100 nm in size. GI-XRD investigations revealed nanocrystallinity across all compositions. TEM imaging supported this observation and revealed segregated grains of Bi and Cu, as well as a metastable BiCu intermetallic, near the catalyst surface. Cu-Bi materials selectively produced formate at efficiencies above 80% at several sets of conditions, specifically at less negative potentials, reaching a maximum of  $\sim 90\%$  at  $-0.9\text{ V}$  vs RHE on a 40 at% Bi, Cu-Bi catalyst. Furthermore,  $\text{CO}$  was produced in significant quantities on 80 at% Bi, reaching efficiencies of  $\sim 25\%$  at partial current densities, larger than any other catalysts in this study. The high selectivity to formate, and not further hydrogenated products, is explained by the weak adsorption properties of  $-\text{COOH}$  and the slow HER on Bi surfaces.

Overall, the alloying of Cu with In or Bi, provides a bifunctional electrocatalytic effect resulting in the significant production of formate and syngas, at greater efficiencies and rates than either pure metallic counterpart. Furthermore, the existence of intermetallic surfaces, both stable and/or metastable, successfully fine-tuned the adsorption properties of  $\text{CO}_2$ ,  $-\text{COOH}$ , and  $-\text{CO}$  leading to increases in efficiency and selectivity of said products.



## **Research Prospects and Realization in Industry:**

The electrochemical reduction of CO<sub>2</sub> is far from being completely understood in the electrochemistry research realm. Reaction pathways and mechanisms, mass transport effects, electrocatalyst material selection and tuning, as well as incorporation into industrial applications are just some of the major areas that require further research and attention.

The use of GDEs in ERC research is very limited, but date back to the late 1980s when the ERC was first being explored as a viable CO<sub>2</sub> conversion method. GDEs provide a three-phase system with the solid catalyst, liquid electrolyte, and gaseous carbon dioxide reactant all working together to produce value-added chemicals and fuels. By increasing the area of this three-phase interface, it is possible to produce larger current densities towards the ERC, while reducing mass transport limitations [1]. Higher pressures of injected CO<sub>2</sub> may result in higher Faradaic efficiencies for methane amongst other ERC products, while simultaneously reducing the HER. GDEs, especially those at higher pressures, can provide the ability to produce value-added products, even with electrocatalyst materials (Ru and Pt) that preferentially reduce water over than CO<sub>2</sub> under standard conditions [2-3]. That being said, higher pressures, up to 50 atm, provide further complications for electrochemical cell design and operation. The research performed herein was done using a batch type setup, while many research groups employ a continuous flow setup. Little has been done to compare these two significantly different setups, although mass transport effects surely have a larger effect on the former.

The work performed here only discusses the product distribution at the conclusion of a run and not over the duration of a given ERC experiment. In order to understand the lifetime of the studied catalysts future work must incorporate a study of product distribution over time.

Catalytic performance and sustainability are of paramount importance to the process's economics as well as its potential scale-up in industry.

While a large majority of the commercially available metals have been explored individually, this work and some recent research has been done on bimetallic alloys for the ERC [4]. Research has been performed on various copper-alloys, Au-Pd, Ru-Pd, amongst other systems, however there are still many promising bimetallic systems yet to be explored [4-8]. Along with the vast number of bimetallic alloys to be investigated, it is also possible to change the exposed crystallographic surfaces and exploring those effects in conjunction with the catalyst material choice. The research presented herein provided a step in that direction – an attempt to correlate crystallography to adsorption strength of intermediates and overall product distribution.

Finally, the work performed on the ERC has been almost purely on the R & D side, with very little done in its realization on the industrial level. Start-up companies such as Dioxide Materials (Champaign, Illinois) and Mantra Venture Group (Vancouver, British Columbia) have already begun work to industrialize this process and use extraneous CO<sub>2</sub> [9-10]. Rather than inject CO<sub>2</sub> underground or in water, current temporary CCS solutions, CO<sub>2</sub> could be utilized in an industrial ERC process – exactly what these innovative pioneers plan to do. Personally, I visualize a process that is directly connected to the CO<sub>2</sub> exhaust of industrial plants, which immediately performs the ERC, with the effluent products being contained and sold or being recycled back into the plant for use, especially in Fischer-Tropsch processes, where the effluent from the ERC is syngas at the appropriate ratio of H<sub>2</sub>: CO. This is the ideal scenario for incorporating the ERC into industry, but we still have a lot of work to do in both R & D and the United States socio-political arena.

## References:

- [1] Mahmood, M. N., Masheder, D., & Harty, C. J. (1987). Use of gas-diffusion electrodes for high-rate electrochemical reduction of carbon dioxide. I. Reduction at lead, indium-and tin-impregnated electrodes. *Journal of applied electrochemistry*, 17(6), 1159-1170.
- [2] Hara, K., Kudo, A., Sakata, T., & Watanabe, M. (1995). High efficiency electrochemical reduction of carbon dioxide under high pressure on a gas diffusion electrode containing Pt catalysts. *Journal of the Electrochemical Society*, 142(4), L57-L59.
- [3] Furuya, N., Yamazaki, T., & Shibata, M. (1997). High performance Ru-Pd catalysts for CO<sub>2</sub> reduction at gas-diffusion electrodes. *Journal of Electroanalytical Chemistry*, 431(1), 39-41.
- [4] Lee, J., Kwon, Y., Machunda, R. L., & Lee, H. J. (2009). Electrocatalytic recycling of CO<sub>2</sub> and small organic molecules. *Chemistry—An Asian Journal*, 4(10), 1516-1523.
- [5] Watanabe, M., Shibata, M., Kato, A., Azuma, M., & Sakata, T. (1991). Design of Alloy Electrocatalysts for CO<sub>2</sub> Reduction III. The Selective and Reversible Reduction of on Cu Alloy Electrodes. *Journal of the Electrochemical Society*, 138(11), 3382-3389.
- [6] Kim, D., Resasco, J., Yu, Y., Asiri, A. M., & Yang, P. (2014). Synergistic geometric and electronic effects for electrochemical reduction of carbon dioxide using gold–copper bimetallic nanoparticles. *Nature communications*, 5.
- [7] Ishimaru, S., Shiratsuchi, R., & Nogami, G. (2000). Pulsed Electroreduction of CO<sub>2</sub> on Cu-Ag Alloy Electrodes. *Journal of The Electrochemical Society*, 147(5), 1864-1867.
- [8] Hahn, C., Abram, D. N., Hansen, H. A., Hatsukade, T., Jackson, A., Johnson, N. C., ... & Jaramillo, T. F. (2015). Synthesis of thin film AuPd alloys and their investigation for electrocatalytic CO<sub>2</sub> reduction. *Journal of Materials Chemistry A*, 3(40), 20185-20194.
- [9] Electrochemical Reduction of Carbon Dioxide Gets Boost. (n.d.). Retrieved June 13, 2016, from <http://www.chemicalprocessing.com/articles/2011/electrochemical-reduction-of-CO2-gets-boost/>
- [10] Electro-reduction of carbon: A new approach to CO<sub>2</sub>. (n.d.). Retrieved June 13, 2016, from [http://arizonaenergy.org/News\\_08/News\\_Nov08/Electro-reduction of carbon; a new approach to CO2.htm](http://arizonaenergy.org/News_08/News_Nov08/Electro-reduction of carbon; a new approach to CO2.htm)